CFRP Delamination Density Propagation Analysis by Magnetostriction Theory

---

A Dissertation
Presented to
the Graduate School of
Clemson University

In Partial Fulfillment
of the Requirements for the Degree
Doctor of Philosophy
Mechanical Engineering

---

by
Brandon Eugene Williams
December 2023

Accepted by:
Oliver Myers, Ph.D., Committee Chair
Garrett Pataky, Ph.D.
Gang Li, Ph.D.
Zhaoxu Meng, Ph.D.
Asha Hall, Ph.D.

Abstract

While Carbon Fiber Reinforced Polymers (CFRPs) have exceptional mechanical properties concerning their overall weight, their failure profile in demanding high-stress environments raises reliability concerns in structural applications. Two crucial limiting factors in CFRP reliability are low-strain material degradation and low fracture toughness. Due to CFRP's low strain degradation characteristics, a wide variety of interlaminar damage can be sustained without any appreciable change to the physical structure itself. This damage suffered by the energy transfer from high-stress levels appears in the form of microporosity, crazes, microcracks, and delamination in the matrix material before any severe laminate damage is observed. This research presents a novel Non-Destructive Evaluation (NDE) technique for assessing subsurface interlaminar interphacial health. A new self-sensing smart composite material is born by embedding microscopic magnetically activated sensors between CFRP ply. Magnetostrictive Carbon Fiber Reinforced Polymer (MagCFRP) is a self-sensing structural health composite material that is magnetically activated by an external magnetic field. This research merges the governing magnetoelasticity and general magnetization mechanics with analytical, experimental, and numerical results. For mode I and mode II fiber-matrix debonding, cracking, and shear delamination, there was an observed localized magnetic flux density gradient of more than 3 mT (2%) with a reversible flux of only 25% for low driving magnetic flux density (≈ 0.2 T) using the indirect magnetization stimulation method.

Dedication

I dedicate this dissertation to the loving memory of two remarkable women who have had an immeasurable impact on my life: my late grandmother, Mary Joyce Perrin, and my late mother, Katrina Neal.

To my dear grandmother, Mary Joyce Perrin, whose unwavering belief in the power of education and her constant encouragement have been a guiding light throughout my academic journey. From the earliest days of my childhood, she instilled in me a passion for learning and always saw the potential within me. She would often tell me with a gleam in her eye that I would be a doctor one day. Her words of wisdom, love, and unwavering support have been a source of inspiration that I carry with me each day. Though she is no longer with us, her spirit lives on, and I dedicate this work to honor her memory and the profound impact she has had on my pursuit of knowledge.

To my beloved mother, Katrina Neal, whose brilliance and dedication to scholarship were evident even in the face of personal challenges. Despite her own unfulfilled dreams of completing her degree in medicine due to her mental disorder, she instilled in me a deep appreciation for the pursuit of knowledge and a relentless pursuit of excellence. Her unwavering support, sacrifices, and love have been the bedrock of my educational journey. I am forever grateful for her enduring belief in my abilities and for the indomitable spirit she instilled within me. I dedicate this work to honor her memory and to carry forward her legacy of intellectual curiosity and resilience.

I am eternally grateful to both my grandmother, Mary Joyce Perrin, and my mother, Katrina Neal, for their unwavering love, belief, and encouragement. Their profound influence continues to shape the person I am today. This work is a testament to their enduring presence in my life and a tribute to their unyielding faith in my potential. To my loving wife, Kourtney Williams, thank you for your support.

Acknowledgments

I want to express my deepest gratitude and appreciation to the Mechanical Engineering Department at Clemson University, especially Dr. Atul Kelkar, the department chair, for his unwavering support throughout the most challenging time in my academic journey. I am particularly grateful to Dr. Atul Kelkar for his genuine care and kind words during a difficult time in my life. When my mother passed away amidst the challenges of COVID protocols, Dr. Kelkar extended his compassion and support, providing solace and encouragement that helped me navigate through those trying times. I also sincerely thank Dr. Asha Hall for her invaluable guidance and the sublime research experience she facilitated at the Army Research Laboratory (ARL). The opportunity to work with Dr. Hall and her team, along with the support and exceptional facilities provided by ARL, significantly contributed to the successful completion of my research. Furthermore, I am deeply indebted to my research advisor and committee chair, Dr. Oliver Myers, for his unwavering belief in my abilities and for providing me with invaluable guidance and mentorship throughout the research process. Dr. Myers' expertise and dedication to my academic growth have been instrumental in shaping the direction of my research and helping me overcome various life challenges along the way. I would also like to express my gratitude to the other committee members, Dr. Garrett Pataky, Dr. Gang Li, and Dr. Zhaoxu Meng. Their engagement in my work, valuable insights, and provision of resources and feedback have been invaluable in enriching the quality of my research. I extend my appreciation to ORAU (Oak Ridge Associated Universities) for their support and provision of resources that have significantly contributed to the completion of my research. Last but definitely not least, I would like to thank Dr. Dereje Seifu of Morgan State University (a Historically Black College) for his mentorship, guidance, and availability during my tenure of applied research in magnetostriction. Dr. Dereje Seifu and his lab at Morgan State University were truly instrumental in completing my work. I am profoundly grateful to all those who have contributed to my academic and personal

growth during my time at Clemson University. Their support, guidance, and encouragement have been instrumental in shaping the researcher and person I am today.

Table of Contents

List of Tables

List of Figures

Chapter 1

Introduction

Carbon Fiber Reinforced Polymers (CFRP) is a class of composite materials that have emerged as a revolutionary engineering material that combines carbon fibers' exceptional strength and stiffness with the versatility and formability of polymers. These composites have found widespread applications across various industries due to their unique properties and outstanding performance characteristics. CFRPs have gained significant traction in the automotive, aerospace, and engineering sectors, offering exceptional lightweight and high-strength solutions for structural applications.

1.1 Modern CFRP Use-Cases

1.1.1 Automotive Industry

In the automotive industry, CFRPs have revolutionized vehicle design and manufacturing. Automakers can significantly reduce weight by incorporating CFRP components while maintaining structural integrity and safety standards. CFRP components, such as body panels, chassis structures, and interior parts, enhance fuel efficiency, improve handling, and increase overall performance. Additionally, CFRPs play a pivotal role in electric vehicles, where minimizing weight is crucial for extending battery range. The automotive carbon fiber market is valued at USD 22.08 billion in 2023, and it is expected to grow up to USD 40.85 billion in 2027 with a CAGR of 10.80% during the forecast period [23].

The demand for strong and lightweight Electric Vehicles (EVs) is rising, driven by the

need for more efficient and sustainable transportation solutions. As the EV industry continues to innovate and evolve, the demand for Carbon Fiber Reinforced Polymers (CFRPs) is expected to increase significantly. CFRPs offer a unique combination of strength and lightweight properties, making them valuable materials for enhancing the performance and efficiency of EVs.

One notable application of CFRPs in the automotive industry can be observed in Formula 1 cars. These high-performance racing vehicles extensively use CFRP composites in their construction to achieve optimal performance, so much so that approximately 85% of a Formula 1 car is made of CFRP [29]. The lightweight nature of CFRPs allows for improved acceleration, maneuverability, and overall speed. The exceptional strength of CFRPs ensures the necessary structural integrity and safety of the vehicle, even under extreme racing conditions. The adoption of CFRPs in Formula 1 showcases their potential to enhance the performance and safety of passenger cars.

Similar applications of CFRPs can make their way into passenger cars, contributing to the weight reduction and overall efficiency of EVs. By incorporating CFRP components in the body structure, chassis, and other key areas, passenger cars can benefit from weight savings without compromising safety or performance. One real-time example of CFRPs being integrated into passenger EVs is Chinese automobile manufacturer NIO, which has developed prototypes for battery enclosures made of CFRP for its NIO high-performance EVs (Figure (1.1)). Plastics Today reports that commercial battery enclosures for electric vehicles are mainly made of aluminum and steel. In comparison, the CFRP battery enclosure is around 40% lighter [22].

The reduced weight of the vehicle translates to enhanced energy efficiency, increased driving range, and improved battery life in EVs. Furthermore, CFRPs' high strength allows for optimized structural designs that can withstand impacts and improve passenger safety. The weight-saving benefits of using CFRPs in EVs can have a drastic impact on their efficacy. By reducing the vehicle's weight, CFRPs help overcome one of the major challenges in electric vehicle technology–maximizing the driving range. Lighter EVs require less energy to propel, leading to increased efficiency and extended range on a single charge. This weight reduction also enables EV manufacturers to allocate more space for batteries, further enhancing the vehicle's driving range and overall performance.

The growing demand for strong and lightweight EVs, coupled with the increasing availability and advancements in CFRP technology, will likely lead to a rise in the usage of CFRPs in the automotive industry. As the EV market expands and consumer expectations evolve, automakers will seek ways to improve the efficiency, performance, and safety of their vehicles. CFRPs offer a viable

Figure 1.1: NIO's CFRP battery enclosure [22].

solution to achieve these goals, making them an attractive choice for lightweight and optimizing EV designs.

1.1.2 Aerospace Industry

The aerospace industry has been an early adopter of CFRPs, utilizing their exceptional properties to enhance aircraft performance and efficiency. CFRP composites are extensively used to manufacture wings, fuselages, empennages, and interior components [14, 39]. By replacing traditional aluminum structures with CFRP, aircraft manufacturers can achieve substantial weight reductions, resulting in increased fuel efficiency, extended range, and improved payload capacity. Moreover, CFRPs offer excellent resistance to fatigue and corrosion, making them ideal for aerospace applications. As the demand for super and hypersonic aerospace vehicles continues to increase, so does the need for advanced materials to meet the unique challenges of these extreme operating conditions. Carbon Fiber Reinforced Polymers (CFRPs) have emerged as a vital solution, offering a combination of exceptional strength, lightweight properties, and high-temperature resilience. The demand for reliable, tunable, and smart CFRPs is expected to rise in parallel with the growth of the super and hypersonic aerospace industries.

CFRPs are extensively utilized in the super and hypersonic aerospace sectors due to their exceptional properties. One notable application is in developing Thermal Protection Systems (TPS), which safeguard vehicles during atmospheric re-entry or high-speed flight. CFRPs are reliable and lightweight materials for TPS components, providing effective insulation and withstanding the extreme heat generated during these operations.

Moreover, CFRPs find widespread use in the manufacturing of structural components in

super and hypersonic aircraft. Wings, fuselages, tail sections, and control surfaces are constructed using CFRP composites, leveraging their high strength-to-weight ratio. The lightweight nature of CFRPs enables higher speeds, increased fuel efficiency, and improved aerodynamic performance. These structural components are vital in reducing overall weight and enhancing maneuverability, stability, and control during high-speed flight [14, 39, 26].

CFRPs also play a significant role in constructing propulsion systems for super and hypersonic aerospace vehicles. Engine components such as turbine blades, combustion chambers, and nozzle structures benefit from the high-temperature resistance and mechanical properties of CFRP materials. By utilizing CFRPs, engine efficiency, performance, and overall vehicle capabilities can be optimized.

In addition to their structural and thermal properties, CFRPs offer the potential for smart and tunable features. With advancements in composite manufacturing techniques, CFRPs can incorporate embedded sensors and actuators, enabling real-time monitoring of structural health and performance. This capability is particularly valuable in super and hypersonic aerospace vehicles, where operational conditions are demanding and the ability to detect and respond to potential issues is critical for safety and performance.

The ongoing innovation in CFRP technology, coupled with their proven performance in aerospace applications, positions them as a key enabler for advancing super and hypersonic aerospace industries. CFRPs are integral to developing reliable and high-performance super and hypersonic aerospace vehicles. Their usage in Thermal Protection Systems, structural components, propulsion systems, and potential smart features highlights their versatility and importance in this rapidly advancing field. As the demand for faster and more efficient aerospace vehicles grows, CFRPs will continue to play a crucial role in enabling these technological advancements.

1.1.3 General Structural Material

CFRPs have emerged as a favored structural material in engineering disciplines. They are being increasingly employed in civil infrastructure projects, including bridges, buildings, and pipelines, due to their high strength-to-weight ratio and durability. Seen in Figure (1.2) is an example of how Sika uses CFRP plates for flexural strengthening of dynamically and statically loaded buildings and other structures. CFRPs enable the construction of lightweight yet robust structures that can withstand high loads and harsh environmental conditions. Using CFRP composites in

Figure 1.2: Installation of Sika's CFRP plates for building support [33]

engineering offers advantages such as improved seismic resistance, reduced maintenance costs, and enhanced design flexibility [33].

1.1.4 Additive Manufacturing

The use of carbon fiber material does not stop at lamina-based ply material, as techniques in additive manufacturing (AM) continue to advance. What was predominantly used as a prototyping tool is now an integral part of engineering materials. An advanced AM material of particular interest in this research is Markforged Onyx material. Onyx is a composite material composed of nylon reinforced by continuous and/or chopped carbon fiber. This combination of materials used in an AM platform gives Onyx favorable engineering characteristics compared to traditional AM materials such as PLA or ABS. One of the main advantages of Onyx is that Markforged's composite 3D printing platform allows users to control and customize the fiber content throughout the geometry of the part (Figure (1.3)). While there is limitless potential for additively manufactured parts to be used in serious engineering applications, it is paramount that designers and engineering have reliable methods for measuring features that are associated with material characterization in a non-destructive manner. This research explores the possibility of tracking deformation and magnetization sensitivity using magnetostriction theory.

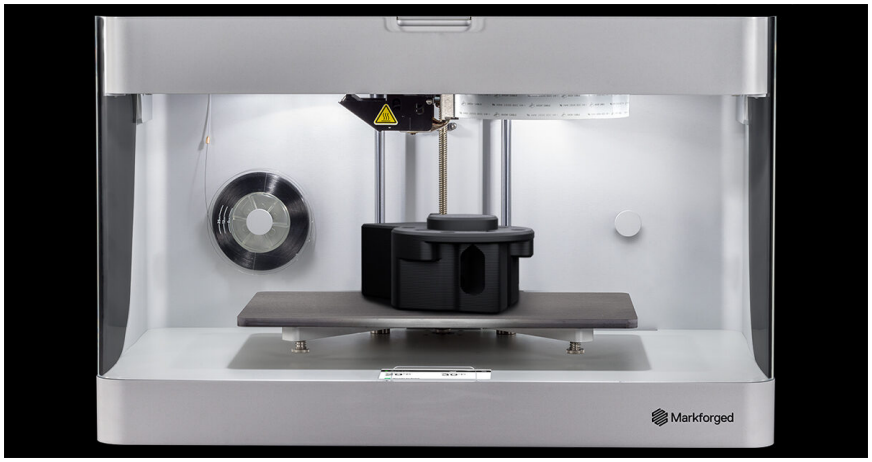

Figure 1.3: Markforged carbon fiber 3D printer. [19]

1.1.5 Expected Demand and Growth

Looking ahead, the demand for CFRPs in structural applications is expected to experience significant growth in the next decade. As industries continue to prioritize lightweight, energy efficiency, and sustainability, CFRPs are poised to play a pivotal role. The automotive sector, driven by the shift towards electric vehicles and stringent emission regulations, is projected to witness a substantial increase in the adoption of CFRPs. Similarly, the aerospace industry will continue to rely on CFRPs to optimize performance, reduce fuel consumption, and improve sustainability. Additionally, the growing utilization of CFRPs in engineering and civil infrastructure projects is anticipated to increase the material's rising demand. Market articles by marketsandmarkets.com report that the pre-preg carbon fiber reinforced polymer global market is expected to grow from 9.7 billion in 2022 to 18.9 billion in 2027 at a compound annual growth rate (CAGR) of 14.2% during the forecast period [18]

1.2 CFRP Reliability and Sustainability

When considering the use of CFRPs in engineering applications, it is crucial to prioritize reliability and sustainability. CFRPs offer exceptional mechanical properties, such as high strength-to-weight ratio and stiffness, making them attractive for aerospace applications. However, ensuring the reliability of CFRP components and structures requires careful attention to several factors, such

as environment-based mechanical performance, structural health, and interphacial health. If the engineering world is to use CFRP to its fullest potential, the life-cycle analysis of these materials must be studied with continuity and rigor. Due to the brittle nature of high-strength CFRPs, catastrophic failure can be imminent if micro and macro defects are left undetected.

1.2.1 CFRP Degradation Characteristics

While CFRPs have exceptional mechanical properties concerning their overall weight, their failure profile in demanding high-stress environments raises reliability concerns. Two crucial limiting factors in CFRP reliability are low-strain material degradation and low fracture toughness, as seen in Figure (1.4). Compared to other widely used ductile engineering materials, such as aluminum, steel, and titanium, CFRP has a much lower strain-to-failure proportionality. With a strain-to-failure of only 2% for on-axis dominate laminates, failure can be imminent and catastrophic, as seen in Figure (1.5) [38]. Due to the low strain degradation characteristics of CFRP, a wide variety of damage can be sustained to the CFRP without any appreciable change to the physical structure itself. This damage suffered by the energy transfer from high-stress levels appears in the form of microporosity, crazes, and delaminations in the matrix material before any severe laminate damage is observed. The CFRP component's capacity and overall life cycle highly depend on the composite's delamination density progression.

The dynamic delamination density propagation in CFRPs is not as simple as in classical fracture mechanics of isotropic materials in that infinite stress crack tips are parameterized by an impending stress field which is then characterized by a stress intensity factor or energy release rate [14]. In CFRPs, cracks can form and grow in different constituents in multiple modes, such as fiber breaks, matrix cracks, ply debonding, particulate, and interphacial cracks. Because there are multiple constituents and modes through which cracks can form, no single critical stress intensity factor and energy release rate can be continuously deployed. However, CFRP's main delamination density content will first exist in the matrix material. While edge delaminations are common where high interlaminar stresses are developed due to the mismatch in Poisson ratio, delamination and fiber breakage are still considered severe in the landscape of CFRP damage progression in structural applications.

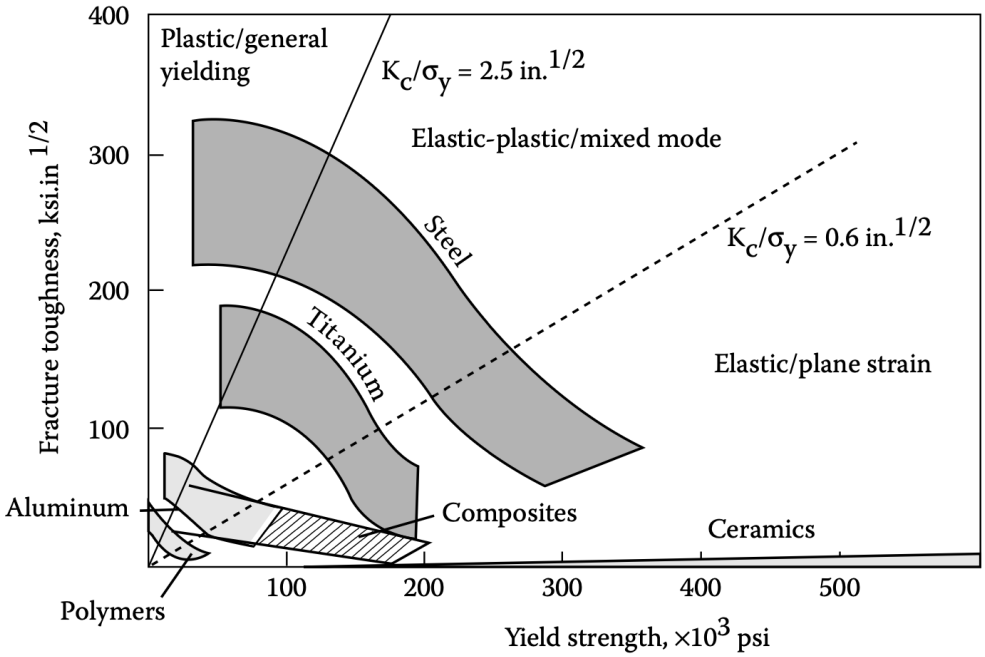

Figure 1.4: Fracture toughness as a function of yield strength for different engineering materials [14].

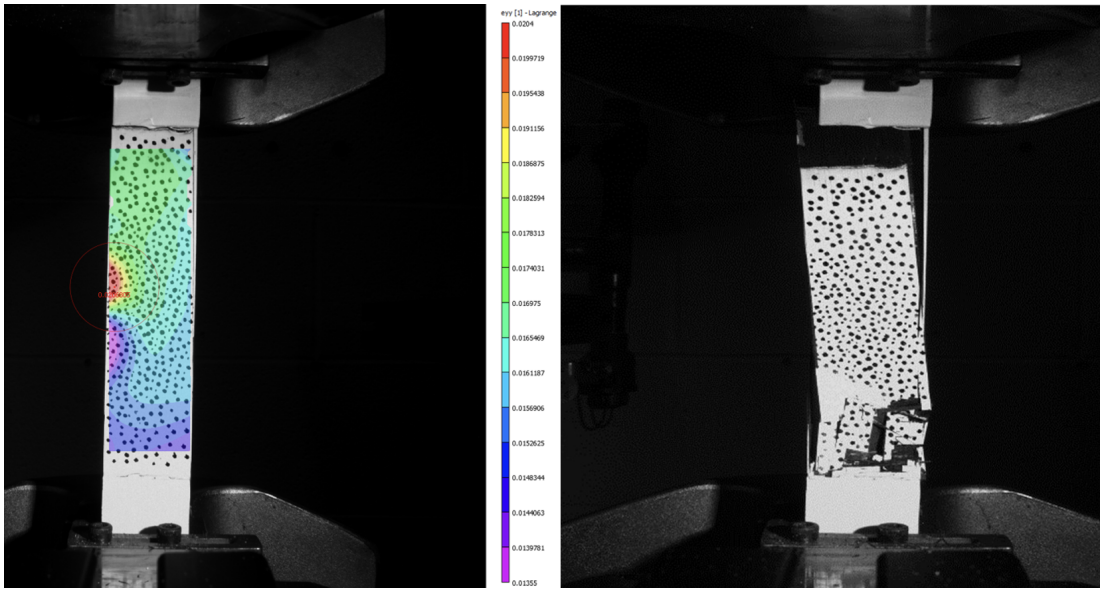

Figure 1.5: a.(left) Strain field (max strain of only 2%) of CFRP sample one DIC time step before failure. b.(right) Captured CFRP catastrophic failure the every next DIC time step during mechanical testing.

1.2.2 CFRP Sustainability Outlook

When using CFRPs in engineering applications, sustainable practices must align with environmental responsibility, resource conservation, and circular economy principles. CFRP production processes can contribute to carbon emissions, energy consumption, and environmental pollution. Minimizing the environmental impact involves adopting cleaner production methods, reducing waste during manufacturing, and optimizing energy usage. Pursuing recycling initiatives and exploring eco-friendly alternatives for raw materials can help mitigate the environmental footprint of CFRPs.

There are two main processes used to recycle CFRP. To recycle CFRP, the material must go through chemical and mechanical processes. During these processes, the material will be collected, sized, reduced, thermally treated, stripped of resin, chemically washed, and repurposed. Recycling CFRP is complex because of the variety of material combinations that can be achieved. While customizable configurations are desirable in composite design, it is the source of complexity when recycling the material at the end of its life cycle. Promoting a circular economy approach for CFRPs involves designing products for extended lifespan, enabling efficient recycling, and reusing materials at the end of their service life. Developing effective recycling methods and establishing recycling infrastructure for CFRPs will reduce waste and maximize the utilization of valuable resources [14].

1.3 NDE Methods for CFRP

Non-Destructive Evaluation (NDE) is a method for testing and evaluating parts, structures, and components' integrity in a non-destructive manner to preserve potential usability. While many different NDE techniques can be deployed on metallic engineering systems, only a subset of these methods are excepted for NDE in CFRPs. Some commonly used methods for NDE for CFRPs include ultrasonic scanning, thermography, x-ray computer tomography (CT), and acoustic emission (AE). While these methods are accepted in the composite community for detecting flaws in CFRP directly and indirectly, these traditional NDE methods are unsuitable for real-time applications. The following section will review new and emerging practices in preparation for the MagCFRP NDE method.

1.3.1 Emerging CFRP NDE Method

While these aforementioned techniques are useful in many applications, their scalability and practicality in robust applications can be limited to environmental and physical constraints. Using a non-contact NDE method such as Terfenol-D embedded CFRP (MagCFRP) has the potential to be used in a wide variety of applications while still possessing scalability and sustainability characteristics.

One widely used non-contact NDE technique is 3D Scanning Laser Vibrometry. 3D Scanning Laser Vibrometry uses a scientific instrument (Laser Doppler Vibrometer, LDV) to make non-contact vibration measurements of a surface. This technique is used for measuring stress wave propagation on the surface of a material rather than the extent and mode of internal damage [28]. The laser beam from the LDV scans the surface of interest for amplitude and frequency from the Doppler shift of the reflected laser beam frequency due to surface motion. LDV outputs are generally a continuous analog voltage. In LDV, the analog voltage is directly proportional to the target velocity component along the direction of the laser beam [28].

Ong and Chiu, 2014 their research and laser Vibrometry assumed the condition of non-surface penetrating defects. Ong and Chiu explore the possibility of relating velocity field wave modes to structural defects. Their research uses metallic test structures, which do not possess the same strain/stress, failure, and defect characteristics as CFRP composites. Using this method in composite would be highly difficult due to the inter lamina configuration and interphase properties. In this work, they refer to idealized specimens concerning geometry rather than the type of material. Ong and Chiu showed that real-world geometry significantly alters the behavior of Lamp wave-based damage detection and, due to CFRP's brittle and abrupt fracture mechanism, LDV may not even be a viable solution for surface defect monitoring of CFRP components. CFRP attenuates high-frequency stress waves, allowing them only to be carried to a distance no longer than a few centimeters from the source location [1].

The test specimens used in Ong and Chiu were made from 6 mm thick aluminum. A partial depth hole is machined on one side of the test plate. A 20 mm diameter partial depth hole simulated a non-surface penetrating defect. Two 10 mm piezoceramic (PZT) actuators initiated the stress waves. Before introducing the non-surface penetrating defect, the undamaged specimen was scanned to obtain a baseline. The damage progressively increased following each scan. The scattering of the

velocity was calculated by the velocity differential concerning time (i.e., $V_{\text{scan}} = |V_{\text{base}} - V_{\text{damage}}|$) [28].

Defects on the scale of millimeters are far too large for early-stage CFRP delamination density propagation use cases. One must also have a three-axis laser vibrometer experimental and production set-up to accurately sense Lamp wave responses in a specimen with three-dimensional geometry. This highly integrated testing procedure raises sustainability concerns due to the high calibration required to use this system confidently.

In Ong and Chiu, a substantial amount of postprocessing must be performed before the raw data can be interpreted. Examples include MATLAB algorithm scripts to generate a time-varying visualization representation of the stress field and 2D FFT processing to understand the dispersion characteristics of the present stress waves. Interestingly, the scattered wavefield is more prominent outside of the partial depth damage and appears to be guided by the circumference of the partial depth defect, even though these measurements were taken on the flat side of the test specimen. This phenomenon can be a source of uncertainty in concentrated localized damage detection.

Another NDE technique is the piezoelectric wafer active sensor (PWAS). This technique is used to detect structural damage through wave propagation techniques. One of the main differences between the state-of-the-art PWAS approach and other conventional NDE techniques is that PWAS NDE uses permanently attached unobtrusive, minimally intrusive transducers. In contrast, the traditional NDE approach uses relatively large and expensive conventional ultrasonic transducers [8]. Giurgiutiu believes their approach will lead to emerging new technology: embedded ultrasonic NDE. The authors propose this new method of embedded ultrasonic NDE to facilitate on-demand interaction of the structure to determine its current state of health and predict its remaining life.

The premise of the PWAS NDE method is that the transducers can be used both as a receiver and a transmitter (pitch and catch). The pitch-and-catch technique is a test with transmitter and receiver transducers, where the path of the ultrasonic beam is not a straight line but follows a complex path [8]. The embedded pitch-catch method was discussed to detect through-thickness fatigue cracks in metallic structures and delamination in composite and bonded structures.

The specimens under consideration in the reported studies ranged from simple geometries to full-scale aircraft-like panels [8]. The presence of irregularities in the time-reversal reconstruction would indicate structural damage. It is stated that many NDE and Non-Destructive Testing (NDT) techniques exist for identifying local damage and detecting an incipient failure in critical structures.

However, these techniques are mainly limited to the continuum level and shed little insight into the micro, nano, and atomistic levels.

Ultrasonic inspection is well-established and has been used in the engineering community for several decades [16]. Ultrasonic NDE methods rely on elastic wave propagation and reflection within the material. This may not be practical for every environment. Due to CFRP's anisotropy, non-homogeneity, and attenuating properties, using ultrasonic NDE may pose a significant challenge in extracting useful information in early damage detection.

Giurgiutiu tries to identify the wavefield disturbances due to local damage and flaws. Ultrasonic testing involves one or more of the following measurements: time of flight (TOF) (wave transit or delay), oath length, frequency, and phase angle [8]. Good contact between the transducer and the structures is obtained using special coupling gels, which adds another layer of complexity to the system. Depending on the transducer type and its bond to the structural surface, the waves created in the structures may be P- waves, S-waves, or a combination of the two [8]. Combining P-waves and S-waves can make defining defects or damages challenging. Ultrasonic inspection of thin-walled structures (e.g., aircraft shells, storage tanks, large pipes, etc.) is time-consuming and requires meticulous through-thickness C-scans over large areas.

Another novel and relatively new approach to NDE of composite components is Electrical Impedance Tomography (EIT). The premise of this research method is to integrate electrically conductive scanning into nanocomposites for self-sensing and health monitoring. EIT NDE correlates local changes in conductivity to damage. This method uses conductivity changes and imaging conductivity evolution in a carbon nanofiber-filled epoxy matrix composite, theoretically allowing the entire matrix to become self-sensing [36].

With this method, a significant thermal effect must be considered. Tallman states that their tests indicate thermal expansion is responsible for conductivity evolution in a carbon nanofillers (CNF)/epoxy composite. As advanced and evolutionary as EIT is, researchers are still taking a proof-of-concept approach in recent work [36]. Embedding carbon nanofiber into the matrix material of the composite can have a significant positive impact on the interlaminar and overall strength of the composite. It is reported by Zhu, Bakis, and Adair, in 2012 that embedding CNFs into matrix composites can yield up to a 57% increase in mode I and mode II fracture toughness [40].

Along with the boost in mechanical properties, embedding these CNFs is the sole mechanism

that allows for damage detection in composite by monitoring the changes in impedance. Theoretically, this method is sublime. However, achieving this balance between mechanical and electrical properties in practice can be challenging. Tallman writes that the electrical conductivity of polymers filled with conductive nanofillers depends on forming well-connected networks of the filler material. Once these well-connected nanofillers are severed by damage, there will be a change in the material conductivity [36]. This would pose a substantial challenge in full-scale aeronautical component manufacturing due to the high sensitivity to nano-manufacturing.

The EIT method also has limitations in that the composite fibers must be conducting, and the matrix is insulating. EIT uses the conductivity distribution from a specified domain boundary to visually represent field impedance [12, 36]. Tallman states that EIT has tremendous potential for SHM because it requires minimally invasive measurements and can be employed in nearly real-time and for a low cost [36]. No further comments were made about what exactly is "nearly real-time" or the magnitude of EIT's "low cost" compared to other traditional SHM methods. Although Tallman states that this method is "minimally intrusive" and has a "low implementation cost," it is worth noting that to scan a 54 mm X 52 mm X 5 mm specimen, one needs 16 electrode pairs to receive a current injection for tomography [36]. Presented later is a CFRP-embedded sensing technique that requires no physical contact to observe magnetic flux response as it pertains to interlaminar damage.

One of the main modes of failure that EIT is interested in is delamination. The approach is to provide full-field matrix material sensing to detect the progression of delamination in small composite panels. Studying current flux through a CFRP system is an intricate process that requires a high level of knowledge in tensor calculus, electrical engineering, and composite mechanics. Some issues arise with reconstructions for damaged and undamaged specimens due to electrode placement mismatches [36].

The tested CNF specimen in Tallman was not integrated into a functional composite laminate. It was an epoxide/acetone/Triton X-100 mixture cured in a silicone mold [36]. The testing procedure simulated the damage by drilling a 6.5 mm diameter hole through the material [36]. With damage precursors in mind, this mode of damage to a structural composite component is severe on the continuum level and could lead to catastrophic failure in a structural part. This damage mode would also be evident with a more straightforward and traditional visual inspection.

Due to the EIT reconstruction errors, even the undamaged baseline results can be mislead-

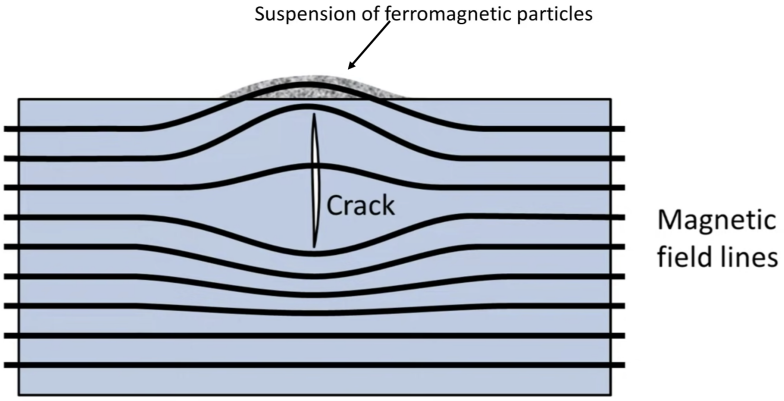

Figure 1.6: Schematic of MPI of ferromagnetic material with a crack orthogonal to the applied magnetic field [20].

ing. Multiple low conductive regions produce similar responses and the damaged specimen. With that in mind, the approach of Tallman is to study the gradient between the tomography scans rather than the raw data. Although this method is unique and novel, its high complexity, unknown scalability to full-scale composite laminate, and damage sensitivity hurt it in being considered a realistic solution for full-scale SHM in aeronautical vehicles.

1.3.2 MPI NDE for MagCFRP

Magnetic Particle Inspection (MPI) is an NDE method for detecting surface and shallow subsurface discontinuities in ferromagnetic materials such as iron, nickel, cobalt, and other alloys. The presence of a surface or subsurface discontinuity in the material allows the magnetic flux to leak because the void content cannot support as much magnetic field per unit volume as metals. In MPI, test pieces can be magnetized by direct or indirect magnetization. Direct magnetization occurs when an electric current is passed through the test object, and a magnetic field is formed in the material. Indirect magnetization occurs when no electric current is passed through the test piece, but a magnetic field is applied from an outside source. To identify a leak, ferrous particles, either dry or in a wet suspension, are applied to a part as seen in Figure (1.6). These are attracted to an area of flux leakage and for what is known as an indication, which is evaluated to determine its nature and cause [20].

Magnetostrictive Carbon Fiber Reinforced Polymer (MagCFRP) is a self-sensing structural

health composite material that is magnetically activated by an external magnetic field. MagCFRP composite constituents are carbon fiber, resin matrix, and Terfenol-D sensors. The magnetically activated Terfenol-D sensors are embedded between the lamina of the composite. These magnetostrictive embedded sensors respond to their surrounding stress field, allowing them to be used as damage sensors, as depicted in Figure (1.7).

Magnetizing MagCFRP to inspect for damage can be considered a subset of indirect MPI where an outside source applies the magnetization. Analogous to the ferrous fluid in MPI is the hall generator in the MagCFRP method. A more rigorous discussion on this MagCFRP NDE method will follow later. This discussion's intended takeaway is to bring light to a well-established NDE method for ferroic materials that share basic principal similarities to magnetostriction scanning for MagCFRP. With future developments, MPI can be developed into another class of methods explicitly designed for CFRPs with ferroic matrix fillers.

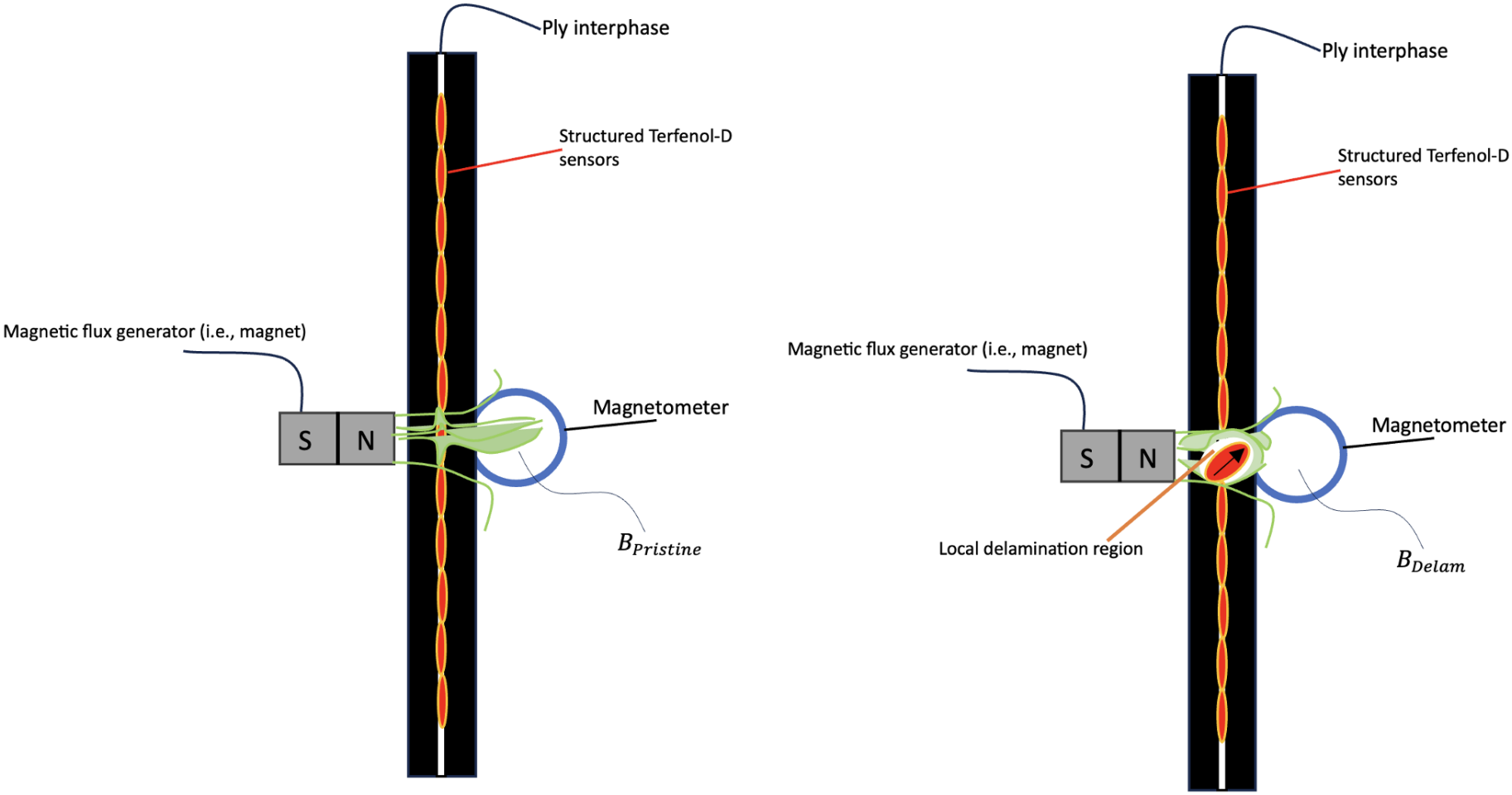

Figure 1.7: Schematic of MagCFRP system with indirect magnetization being applied. a. (left) A pristine MagCFRP system with embedded structured sensors emitting a pristine magnetic response (i.e., $B_{pristine}$). b. (right) A locally delaminated MagCFRP system with an embedded sensor emitting a delamination magnetic response (i.e., B_{Delam}).

1.4 Magnetostriction Theory

Magnetostriction is a property of ferromagnetic and paramagnetic materials that causes them to change in shape under the influence of an external magnetic field. The underlining mechanics that cause a change in length in magnetostrictive materials result from the rotation of tiny magnetic domains within the material. This rotation and reorientation cause internal strains in the material structure. The structure strains lead to the material's stretching in the direction of the magnetic field.

1.4.1 General Principles of Magnetostriction

Internally, ferromagnetic and paramagnetic materials are partitioned into magnetic domains, each of which is a region of uniform magnetic polarization. When a magnetic field is applied, the boundaries between the domains shift, and the domains rotate; both of these effects cause a change in the material dimensions. This phenomenon is governed by magnetocrystalline anisotropy, which states that in magnetocrystalline materials, it takes more energy to magnetize the material in one direction than another. This principle is of particular importance to the MagCFRP system, as it is the foundation that establishes the formation of defects, or the lack thereof, and delaminations in the composite system. If a magnetic field is applied to the material at an angle to an easy axis of magnetization, the material will tend to rearrange its structure so that an easy axis is aligned with the field to minimize the free energy of the system. Since different crystal directions are associated with different lengths, this effect induces a strain in the material [13].

The sensitivity of magnetostriction in a ferromagnetic or paramagnetic material is proportional to the induced magnetic field. The stronger the applied magnetic field is, the more the material will reorient and strain in the direction of the field. This relationship will continue until all the magnetic domains align and the material's magnetization saturation is met (Figure (1.8)).

The relationship between magnetization (M) and the applied magnetic field (H) is approximately linear in the low to moderate field strength range. This means that the magnetization increases proportionally with the applied field. This linear relationship is mathematically expressed as $M = \chi \cdot H$, where χ is the magnetic susceptibility, a material-specific constant (depicted in Figure (1.9)) [24]. More on this topic of susceptibility and magnetization will be discussed in 2.1.2.

Magnetostriction is generally a reversible energy exchange between the mechanical and

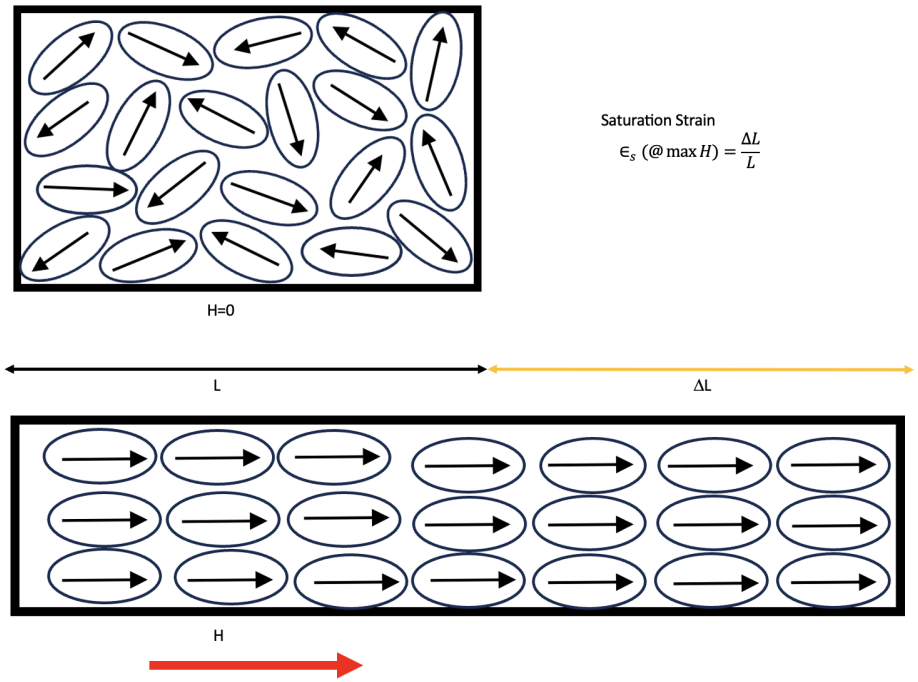

Figure 1.8: Schematic of the magnetostriction phenomenon as it pertains to magnetocrystalline anisotropy and magnetic dipole moments.

magnetic forms. The Joule Effect consists of the material's expansion, positive magnetostriction, contraction, or negative magnetostriction. Without the magnetic field, the sample shape returns to its original dimensions. Another important principle in the MagCFRP system is the Villari Effect. When subjected to mechanical stress, The Villari Effect changes a material's magnetic susceptibility (response to an applied field). For example, suppose the stress field surrounding embedded magnetostrictive material in CFRP would change. In that case, the Villari Effect states that there would also be a proportional change in the material's magnetic susceptibility (i.e., its magnetic flux density).

A pickup coil can detect the change in magnetic flux density and is proportional to the applied stress level. In this current iteration of MagCFRP, the pickup coil is exchanged for a hall generator that shares the same general principles. A Hall generator is a device that utilizes the Hall effect to measure changes in magnetic flux density or magnetic field strength. When subjected to a magnetic field perpendicular to the current flow, the Hall effect creates a voltage difference across a conductor or semiconductor. By measuring the Hall voltage, it is possible to determine the

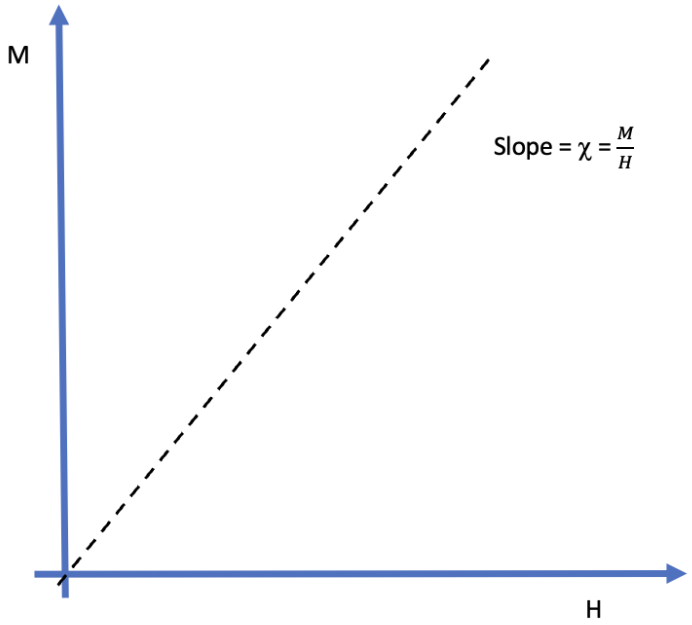

Figure 1.9: General magnetic susceptibility curve of ferromagnetic and paramagnetic materials.

magnitude and polarity of the magnetic field (Figure 1.10).

1.4.2 Magnetostrictive Material for MagCFRP

Terfenol-D is a magnetically activated smart material composed of Terbium (Tb), Dysprosium (Dy), and Iron (Fe). Typical ferromagnetic magnetostrictive materials have a saturation magnetostriction strain of only $\lambda_s \approx 10^{-6}$. However, at room temperature, Terfenol-D has the highest observed Joule magnetostriction with saturation magnetostriction strain of $\lambda_s \approx 10^{-3}$ [18]. Along with Terfenol-D's high magnetostrictive properties, it also has magneto-mechanical coupling properties, meaning as the material is exposed to a magnetic field, it becomes stiffer [6, 15, 17, 27, 25]. Terfenol-D particles have a C15 cubic laves crystal structure in a demagnetized state. However, Terfenol-D is a polymorphic structure that can change into different crystalline structures and still possess the same chemical composition [17, 25]. This characteristic allows Terfenol-D to strain three orders of magnitude greater than any other ferromagnetic or paramagnetic material.

Terfenol-D's high magnetostrictive properties give it the unique ability to be used as an embedded sensor. By embedding Terfenol-D particles into CFRP's matrix, creating a magnetoelas-

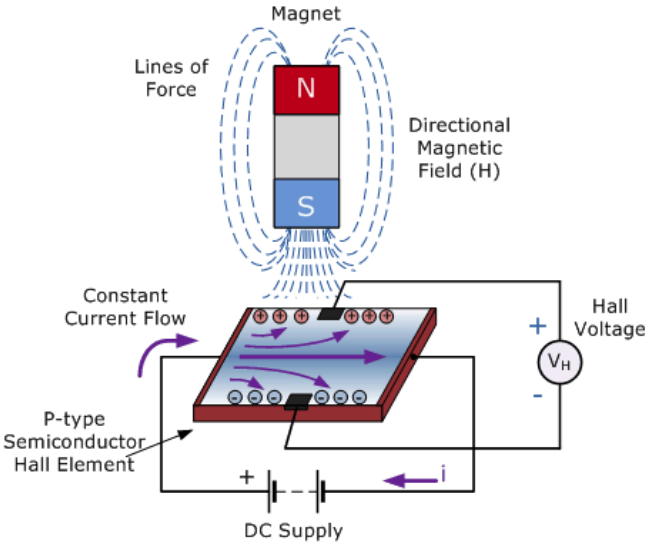

Figure 1.10: Schematic of Hall generator [37].

tomer, real-time magnetostriction data can be tracked and analyzed. Implementing the Villari effect to the magnetostriction responses of a MagCFRP composite will allow critical mechanical features to be monitored and processed for damaged detection systems [6, 15, 17, 27, 25].

Chapter 2

Mechanical Methods and Approach to MagCFRP

2.1 Magnetoelasticity Governing Concepts

In classical mechanics, the relationship between stress and strain is well-established, where strain is exhibited in a material when stress is applied to a body. However, in the realm of magnetostrictive materials, such as Terfenol-D, a fascinating phenomenon occurs. These materials demonstrate the ability to experience strain when subjected to a magnetic field in addition to the conventional mechanical stress. In general, the scheme of magnetostriction follows the framework of small-strain linear elasticity theory. The primary caveat in using magnetostrictive materials in a composite laminate is integrating a multiphysics constituent makes modeling the physical behavior extremely challenging. The interpretation and analysis of this MagCFRP system are driven by damaged precursors derived from the matrix-fiber interphase failure. Due to the inelastic characteristics of the carbon fiber and the matrix material's extremely elastic characteristics, the Terfenol-D is embedded in the matrix material. Two primary governing equations that define the magnetostrictive phenomena are given below in equations (2.1) and (2.2):

$$\delta B_i = d_{ij}\delta\sigma_j + \mu_{ij}^{\sigma}\delta H_j \tag{2.1}$$

where B is the magnetic flux density, d is the magnetostrictive coefficient ($\frac{nm}{A}$), μ is the permeability at constant stress ($\frac{H}{m}$), σ is the material stress, H is the magnetic field strength ($\frac{A}{m}$), and δ is the small perturbation symbol [17]. Defining the strain yields equation (2):

$$\delta\epsilon_i = S_{ij}^H \delta\sigma_j + d_{ij}^T \delta H_j \tag{2.2}$$

where ϵ is material strain, S is the material compliance at constant magnetic field, σ is the material stress, d is the magnetostrictive coefficient, H is the magnetic field strength, and δ is the small perturbation symbol.

As seen in equations (2.1) and (2.2) above, there is a magnetostrictive coupling between the magnetic flux density equation and the strain equation due to the magnetostrictive coupling coefficient tensor d_{ij} and the stress vector σ_{j}. The symbol δ means that, in ferromagnets, the above equations are valid only for small perturbations of the variables around their equilibrium static values [17]. This magnetostrictive coupling mechanism is the gateway that will allow the monitoring of critical information about the localized fiber-matrix interphase health. With linear elasticity in mind, equations (2.1) and (2.2) can be rewritten using a first-order strain and force tensor and a 9×9 second-order elastomagnetic tensor as seen in equation (2.3):

$$\begin{bmatrix} \delta\epsilon_{\mathrm{xx}} \\ \delta\epsilon_{\mathrm{yy}} \\ \delta\epsilon_{\mathrm{zz}} \\ \delta\epsilon_{\mathrm{yz}} \\ \delta\epsilon_{\mathrm{zx}} \\ \delta\epsilon_{\mathrm{xy}} \\ \delta B_{\mathrm{x}} \\ \delta B_{\mathrm{y}} \\ \delta B_{\mathrm{z}} \end{bmatrix} = \begin{bmatrix} S_{11}^H & S_{12}^H & S_{13}^H & \frac{1}{2}S_{14}^H & \frac{1}{2}S_{15}^H & \frac{1}{2}S_{16}^H & d_{11} & d_{21} & d_{31} \\ S_{12}^H & S_{22}^H & S_{23}^H & \frac{1}{2}S_{24}^H & \frac{1}{2}S_{25}^H & \frac{1}{2}S_{26}^H & d_{12} & d_{22} & d_{32} \\ S_{13}^H & S_{23}^H & S_{33}^H & \frac{1}{2}S_{34}^H & \frac{1}{2}S_{35}^H & \frac{1}{2}S_{36}^H & d_{13} & d_{23} & d_{33} \\ \frac{1}{2}S_{14}^H & \frac{1}{2}S_{24}^H & \frac{1}{2}S_{34}^H & \frac{1}{4}S_{44}^H & \frac{1}{4}S_{45}^H & \frac{1}{4}S_{46}^H & \frac{1}{2}d_{14} & \frac{1}{2}d_{24} & \frac{1}{2}d_{34} \\ \frac{1}{2}S_{15}^H & \frac{1}{2}S_{25}^H & \frac{1}{2}S_{35}^H & \frac{1}{4}S_{45}^H & \frac{1}{4}S_{55}^H & \frac{1}{4}S_{56}^H & \frac{1}{2}d_{15} & \frac{1}{2}d_{25} & \frac{1}{2}d_{35} \\ \frac{1}{2}S_{16}^H & \frac{1}{2}S_{26}^H & \frac{1}{2}S_{36}^H & \frac{1}{4}S_{46}^H & \frac{1}{4}S_{56}^H & \frac{1}{4}S_{66}^H & \frac{1}{2}d_{16} & \frac{1}{2}d_{26} & \frac{1}{2}d_{36} \\ d_{11} & d_{21} & d_{31} & \frac{1}{2}d_{14} & \frac{1}{2}d_{15} & \frac{1}{2}d_{16} & \mu_{11}^\sigma & \mu_{12}^\sigma & \mu_{13}^\sigma \\ d_{21} & d_{22} & d_{23} & \frac{1}{2}d_{24} & \frac{1}{2}d_{25} & \frac{1}{2}d_{26} & \mu_{12}^\sigma & \mu_{22}^\sigma & \mu_{23}^\sigma \\ d_{31} & d_{32} & d_{33} & \frac{1}{2}d_{34} & \frac{1}{2}d_{35} & \frac{1}{2}d_{36} & \mu_{13}^\sigma & \mu_{23}^\sigma & \mu_{33}^\sigma \end{bmatrix} \begin{bmatrix} \delta\sigma_{\mathrm{xx}} \\ \delta\sigma_{\mathrm{yy}} \\ \delta\sigma_{\mathrm{zz}} \\ \delta(\sigma_{\mathrm{yz}} + \sigma_{\mathrm{zy}}) \\ \delta(\sigma_{\mathrm{zx}} + \sigma_{\mathrm{xz}}) \\ \delta(\sigma_{\mathrm{xy}} + \sigma_{\mathrm{yx}}) \\ \delta H_{\mathrm{x}} \\ \delta H_{\mathrm{y}} \\ \delta H_{\mathrm{z}} \end{bmatrix} \tag{2.3}$$

where the $\frac{1}{2}$ and $\frac{1}{4}$ are calculated coefficients are unique to the elastomagnetic tensor [17]. As aforementioned earlier in this section, the magneto-mechanical couple coefficient, $\mathrm{k_{nn}}$, is a unitless parameter used to determine the magnetostrictive coefficient but is predominantly used in the ΔE-

Effect. The ΔE-Effect is the change in the magnetostrictive material's Young's Modulus due to the induced magnetic field change. The ΔE-Effect is governed by equation (2.4) [6, 15, 17, 27, 25]:

$$E^B = \frac{E^H}{1 - k_{33}} \tag{2.4}$$

where E^B is the magnetostrictive material's Young's Modulus at a constant magnetic flux density, E^H is the magnetostrictive material's Young's modulus at a constant magnetic field, and k_{33} is the magneto-mechanical coupling coefficient in the outward normal direction. There are numerous methodologies to equate the magneto-mechanical coefficient. For consistency, equation (2.5) can is used to determine the magneto-mechanical coupling coefficient [17, 9, 25, 6, 15]:

$$k_{33}^2 = \frac{d_{33}^2}{\mu_{33}^\sigma} \tag{2.5}$$

where μ_{33}^σ is the outwardly normal permeability at constant stress, and d_{33}^2 is the outwardly normal magnetostrictive coefficient.In this equation, the magnetostrictive coefficient equal to the change in strain due to a change in an induced magnetic field, as seen in equation (2.6) [6, 15, 17, 27, 25]:

$$d_{33} = \frac{d\lambda}{dH} \tag{2.6}$$

Neither the magneto-mechanical coupling factor k_{33} nor the magnetostrictive coefficient d_{33} will remain constant throughout the operating conditions in real magnetostrictive applications [6, 15, 17, 27, 25]. For Terfenol-D, the magnetostrictive coefficient is in the range of 5-70 nm/A [17].

2.1.1 Magnetic Flux Density

The beauty of MagCFRP for delamination density propagation lies in its ability to detect changes in mechanical states by monitoring one feature, that is, magnetic flux density. Magnetic flux density, B, measured in units of tesla (T), is a physical quantity used to measure the intensity of a magnetic field acting on a medium. The magnetic flux density is related to the magnetic field strength H ($\frac{A}{m}$) by a proportionality term μ ($\frac{Henry(H)}{m}$), which is an indicator of magnetic susceptibility in materials. The measure of B encompasses all magnetization response of the medium, including polarisation J (which is the value quantifying response of matter to an applied magnetic field due to alignment of internal magnetic dipole moments (T), and any non-magnetic contributions arising from

the applied field strength H due to external electric currents or internal eddy currents [24, 27, 41]. The governing relationship that maps these physical quantities to one another, in general, is given by the expression:

$$B_i = J_i + \mu_{ij} H_j \tag{2.7}$$

where B is the magnetic flux density, J is the polarisation of the material of interest, μ is the absolute permeability of the material ($\mu_r \cdot \mu_0$, relative permeability (unitless) and absolute permeability respectively), H is magnetic field strength.

While the definition of magnetic flux density in equation (2.7) differs from the previous magnetoelasticity definition given in equation (2.1), it is worth introducing equation (2.7) as a fundamental basis of magnetization of a magnetizable material from the perspective of internal dipole moment orientation, as this is a critical principle in the MagCFRP system for delamination density propagation. Since MagCFRP is a hybrid system, magnetostriction and magnetization of the embedded Terfenol-D content will be affected by the physical constraints that the surrounding constituents (i.e., matrix and carbon fiber) exert on the Terfenol-D. These initial constraints are exerted as fabrication residual stresses from equation (2.1) and boundary-dipole moment volume constraints from equation (2.7).

When a magnetostrictive material, such as Terfenol-D, is constrained from moving, its magnetization behavior is affected. When a magnetostrictive material can move freely, applying a magnetic field causes it to change shape or dimensions, resulting in a strain. This strain affects the material's magnetic domains and alignment, leading to changes in its magnetization.

However, when the magnetostrictive material is constrained from moving, its ability to change shape or dimensions is restricted. As a result, the magnetostrictive effect is suppressed or significantly reduced [24, 27, 41]. In a pristine MagCFRP system (i.e., without damage from applied loading), the embedded Terfenol-D will be constrained due to a residual normal compressive stress from fabrication. Pristine MagCFRP systems will have an associated pristine magnetic response that captures the system's physical state as it refers to localized particle orientation and magnetization (as depicted in Figure (1.7)).

In practical terms, constraining a magnetostrictive material from moving prevents it from exhibiting its full magnetostrictive capabilities. The material's response to the applied magnetic field becomes limited, and its magnetization may not reach the same levels as if it were free to deform.

This constraint can result in reduced sensitivity to magnetic fields and diminished magnetostrictive performance [17]

2.1.2 Magnetic Material Susceptibility

Susceptibility of magnetic materials, denoted by χ (unitless), can be thought of as the sensitivity between an induced magnetic field H and material magnetization M ($\frac{A}{m}$). In most applications, this relationship is linear and can be expressed using:

$$M_i = \chi H_i \tag{2.8}$$

In paramagnetic materials, such as Terfenol-D, the magnetization is linearly related to the induced magnetic field until the material reaches its saturation point. Initially, when a paramagnetic material is exposed to a weak magnetic field, the alignment of the magnetic moments is random, and the magnetization is relatively low. However, as the strength of the applied magnetic field increases, the magnetic moments gradually align with the field, increasing magnetization.

As the applied magnetic field increases, the magnetic moments align completely with the field direction. At a certain point, known as the saturation point, the material's magnetization reaches its maximum value, and further increases in the applied field have no significant effect on the magnetization. At saturation, the relationship between magnetization and the applied field becomes nonlinear. This nonlinearity results from aligning all available magnetic moments within the material. The material cannot exhibit any further increase in magnetization since all possible alignments have been achieved. Once the material reaches saturation, the magnetization plateaus, remaining constant even if the applied magnetic field continues to increase. The saturation magnetization represents the maximum magnetization achieved in the given material.

It is worth noting that the magnetic susceptibility of a paramagnetic material, such as Terfenol-D, is also influenced by temperature. According to Curie's law, the magnetic susceptibility χ of a paramagnetic material is directly proportional to the reciprocal of the absolute temperature (T). Mathematically, it can be expressed as:

$$\chi = \frac{C}{T} \tag{2.9}$$

where C is the material-specific Curie constant. As temperature increases, the thermal energy also increases. This thermal energy disrupts the alignment of the magnetic moments within the material, making it more difficult for the material to be magnetized and reducing its susceptibility. Therefore, the magnetic susceptibility decreases as temperature increases. Conversely, as the temperature decreases, the thermal energy decreases, allowing for better alignment of the magnetic moments and an increase in the material's magnetic susceptibility [24, 27, 41].

It is important to note that as the temperature approaches absolute zero (0 Kelvin), the thermal energy becomes extremely low, and the magnetic moments of the material tend to align more easily. However, as the temperature approaches infinity, the thermal energy overwhelms any magnetic alignment, causing the material's magnetic susceptibility to approach zero. For MagCFRP to be used confidently in real-time temperature-sensitive applications, it will be paramount that engineers parameterize the state of magnetic susceptibility (i.e., magnetic flux density) by real-time environmental temperature conditions.

With delamination density propagation in mind, defining the magnetic susceptibility in terms of a unit volume element V is appropriate. As delaminations form around Terfenol-D sensors, the bounds on the differential volume element dV will change, subsequently changing the degree of magnetization. Magnetization, M, can be mathematically defined as the vector sum of magnetic dipole moments by:

$$M_i = \frac{\sum^k (m_i)_k}{V} \tag{2.10}$$

where m_i is the individual vector magnetic moments ($A \cdot m^2$) and V is the unit volume. Rearranging equation (2.8) in terms of magnetic susceptibility with respect to magnetic dipole moments and volume:

$$\chi = \frac{\sum^k (m_i)_k}{H_i} \frac{1}{V}. \tag{2.11}$$

The magnetic susceptibility in terms of a differential volume element dV can be mathematically defined by:

$$d\chi = \frac{\sum^k (m_i)_k}{H_i} \frac{1}{V} dV. \tag{2.12}$$

Similarly, this same magnetization representation with respect to volume and be utilized to mathematically define polarisation J, as the material polarisation is expressed in the same quantity as

magnetization M but is scaled by the permeability μ:

$$J_i = \mu_{ij} M_j. \tag{2.13}$$

Rearranging equation (2.13) with respect to magnetic dipole moments and volume:

$$J_i = \mu_{ij} \frac{\sum^k (m_j)_k}{V}. \tag{2.14}$$

With equation (2.14), the differential magnetic polarisation in terms of a differential volume element dV can be mathematically defined by:

$$J_{i,V} = \mu_{ij} \frac{\sum^k (m_j)_k}{V} dV. \tag{2.15}$$

Subsequently, a new expression for magnetic flux density can be defined using equation (2.14), yielding:

$$B_i = \mu_{ij} \left(\frac{\sum^k (m_j)_k}{V} + H_j \right). \tag{2.16}$$

With equation (2.15), the differential magnetic flux density in terms of a differential volume element dV can be mathematically defined by:

$$B_{i,V} = \left[\mu_{ij} \left(\frac{\sum^k (m_j)_k}{V} + H_j \right) \right] dV. \tag{2.17}$$

Equations (2.16) and (2.17) allow the magnetic flux density to be expressed in terms of a pristine volume element V and a deformed volume element $V + dV$ (seen in Figure (2.1)). In the absents of loading and damage, the Terfenol-D sensors will be constrained by the surrounding fiber and matrix material. When delaminations form by the matrix bond energy-yielding to exceeded cohesive stress, critical stress intensity factor, and critical energy release rates, the volume element $V + dV$ will affect the overall localized magnetization and magnetic flux density. In the applications where the applied magnetic field is constant, it is apparent in equations (2.16) and (2.17) that an increase in volume will decrease the observed localized magnetic flux density.

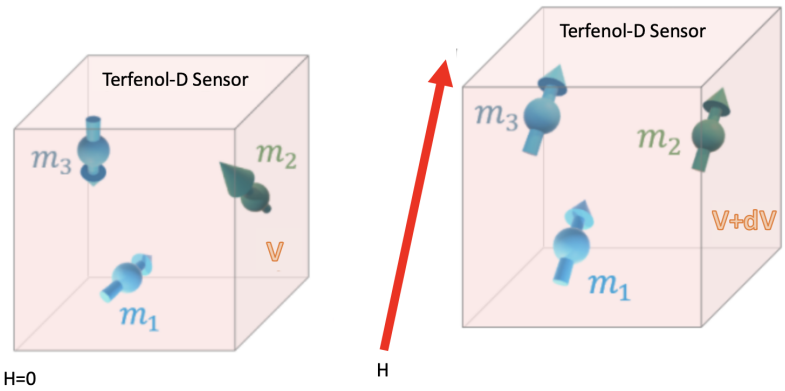

Figure 2.1: a. (left) Terfenol-D sensor volume element (V) with no applied magnetic field. b. (right) Terfenol-D sensor volume element (V+dV) with an applied magnetic field H [24, 27, 41].

2.1.3 MagCFRP Energy Outlook

When using magnetostrictive systems, such as MagCFRP, it is essential to understand the relationships between the various thermal, elastic, and magnetic potentials. From a thermodynamic potential energy perspective, several crucial material states and characteristics can be understood by studying the multi-physical relationships that exist in the system. Specifically for magnetic material systems, features, and attributes concerning the material behavior, phase transitions, and magnetic energy storage can be studied and understood. Establishing a thermodynamic basis is critical to understanding the evolution of delamination density propagation in MagCFRP systems.

The conservation of internal energy of an adiabatic magnetic system may be mathematically expressed as:

$$dU = TdS + \int_V \left[\sum_{ij} \sigma_{ij} d\eta_{ij} + \sum_i H_i dB_i \right] dV = 0 \tag{2.18}$$

where U is the internal energy, T is temperature, S is entropy, σ is a stress tensor, η is a Lagrangian strain tensor, H is magnetic field, B is magnetic flux density, and V is volume [17]. Under the conditions where the temperature is constant, and the stresses and magnetic field are specified, the internal energy per unit volume can be represented by $E = U/V_0$, where V_0 is the sample volume before the appearance of magnetism without any stress, and the thermodynamic potential per unit

volume can be expressed mathematically by the Generalized Gibbs Function, G, given by:

$$G = E - TS - \sum_{ij} \sigma_{ij} d\eta_{ij} - \sum_{i} H_i dB_i = 0 \tag{2.19}$$

where $S = \frac{S}{V_0}$. With this, the equilibrium condition is given by:

$$dG = -SdT - \sum_{ij} \eta_{ij} d\sigma_{ij} - \sum_{i} B_i dH_i = 0 \tag{2.20}$$

As mentioned in section 2.1.2, in magnetostrictive applications where the applied magnetic field is constant (i.e., generated by a neodymium magnetic), the observed magnetic flux density will be proportional to the differentiable volume element dV, thus changing equation (2.20) to:

$$dG = \left[-SdT - \sum_{ij} \eta_{ij} d\sigma_{ij} - \sum_{i} B_i H_i \right] dV = 0. \tag{2.21}$$

As dG is an exact differential, it is possible to express B_i strictly in terms of thermodynamic potential G, magnetic field H, and volume V, such that:

$$B_i = -\frac{\partial G}{H_i dV} \tag{2.22}$$

Knowing the thermodynamic potential and how it relates to localized magnetic flux density helps identify and study these phase transitions, such as the transition from a non-magnetic to a paramagnetic state. Understanding the thermodynamics of such transitions provides insights into the underlying critical constraint mechanisms (i.e., crack growth), critical temperatures, and the material's behavior near these transitions.

2.2 MagCFRP Fracture Mechanics

As mentioned in section 1.2.1, the dynamic delamination density propagation mechanics in CFRPs is not as simple as classical fracture mechanics for isotropic materials in that infinite stress crack tips are parameterized by an impending stress field which is then characterized by a stress intensity factor or energy release rate [14]. In CFRPs, cracks can form and grow in different constituents in multiple modes, such as fiber breaks, matrix cracks, ply debonding, particulate, and

interphacial cracks. Because there are various constituents and modes through which cracks can form, no single critical stress intensity factor and energy release rate can be continuously deployed. However, CFRP's main delamination density content will first exist in the matrix material.

One semi-classical fracture mechanics model that fits the interphase and progressive failure criteria of a MagCFRP system is the Local Delamination fracture mechanics model developed by T. Kevin O'Brien and the Structures Laboratory, U.S. Army Research and Technology Laboratories (AVSCOM) and NASA Langley Research Center, Hampton, VA 23665 in Delamination and Debonding of Materials, ASTM STP [2]. This model develops constitutive relationships between strain-energy release rate, G, and local delamination growth from a matrix ply crack. To deploy this model in MagCFRP applications, the primary assumption must be made is the initial crack surface, and size is defined as the shape and size of the embedded Terfenol-D sensor post-fabrication. For an elastic body containing a Terfenol-D sensor in the form of a crack that grows under a constant applied load, P, the strain energy release rate, G, is given by:

$$G = \frac{P^2}{2}\frac{dS}{dA_{TDS}} \tag{2.23}$$

where S is the compliance and A_{TDS} is the Terfenol-D sensor surface area created under fabrication conditions. A similar expression for G can be established regarding stress, σ, and the reciprocal of modulus, S_0, where $S_0 = \frac{\epsilon}{\sigma}$. Substituting S_0 for compliance S and using the chain rule, we can express equation (2.23) by:

$$S = \frac{S_0 l}{wt} \tag{2.24}$$

which yields,

$$G = \frac{1}{2}V\sigma^2\frac{dS_0}{dA} \tag{2.25}$$

where $\frac{dS_0}{dA}$ is the rate of change in S_0 as the flaw extends beyond the Terfenol-D sensor, and V is the volume of the element (i.e., $V = wtl$). To evaluate $\frac{dS_0}{dA}$ and subsequently G, an equation for laminate compliance as a function of Terfenol-D sensor size must be developed.

Figure (2.2) illustrates a MagCFRP laminate containing a single Terfenol-D sensor with a growing surrounding fracture surface in the form of a matrix ply crack. For brevity, this failure mode should be considered as delamination. The MagCFRP snapshot gauge length, l, is divided into a locally delaminated region, a, and a laminated region, $l - a$. Assuming that the MagCFRP

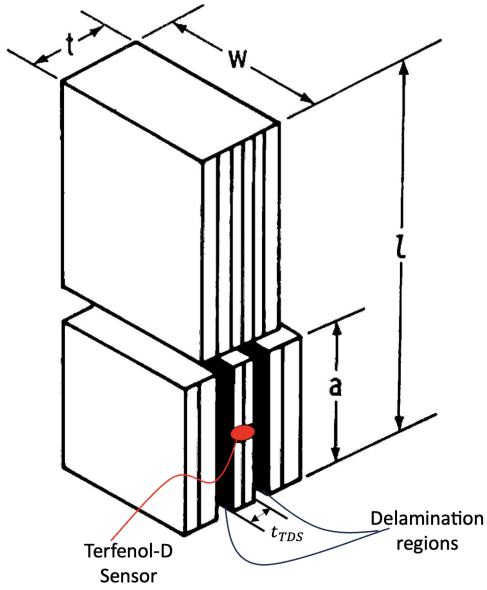

Figure 2.2: Modified T. Kevin O 'Brien cross-sectional model of a local CFRP delamination around an embedded Terfenol-D sensor (Modified delamination detectability $38.38\mu m \leq t_x \leq 107.06\mu m$) [2]

laminate snapshot displacements are the sum of the laminate snapshot subsection in a and $l-a$, and the total load, P, is equal to the loads carried by each subsection, by using Hooke's Law, $\Delta l = \frac{Pl}{AE}$, yields:

$$S_0 = \frac{1}{E} = \frac{A_{LAM}}{l}\left[\frac{(l-a)}{A_{LAM}E_{LAM}} + \frac{a}{A_{TDS}E_{TDS}}\right] \tag{2.26}$$

where A_{LAM} and E_{LAM} are the cross-sectional area and modulus of the laminated region, and A_{TDS} and E_{TDS} are the cross-sectional area and modulus of the local Terfenol-D sensor acting as a delamination region. Each area in equation (2.26) represents only the cross-sectional area that carries the applied load, hence:

$$A_{LAM} = wt \tag{2.27}$$

$$A_{TDS} = wt_{TDS} \tag{2.28}$$

where w is the MagCFRP width, t, and t_{TDS} are the thicknesses of the MagCFRP with and without a Terfenol-D sensor, respectively. Substituting equations (2.27) and (2.28) into equation (2.26) yields:

$$S_0 = a\left(\frac{t}{l}\right)\left(\frac{(1}{t_{TDS}E_{TDS}} - \frac{1}{tE_{LAM}}\right) + \frac{1}{E_{LAM}} \tag{2.29}$$

As seen in equation (2.29), the MagCFRP laminate compliance is a linear function of the local delamination region, a.

Returning to Figure (2.2), the strain-energy release rate associated with the growth of delaminations from a matrix ply crack around a Terfenol-D sensor can be calculated by assuming:

$$\begin{aligned} V &= twl \\ A &= mwa \\ dA &= mwda \end{aligned} \tag{2.30}$$

where m is the number of Terfenol-D sensors with surrounding delaminations growing from matrix ply cracking. Substituting equation (2.30) into equation (2.25) and differentiating equation (2.29) yields:

$$G = \frac{\sigma t^2}{2m}\left(\frac{(1}{t_{TDS}E_{TDS}} - \frac{1}{tE_{LAM}}\right) \tag{2.31}$$

or similarly, in terms of the applied load P:

$$G = \frac{P^2}{2mw^2}\left(\frac{(1}{t_{TDS}E_{TDS}} - \frac{1}{tE_{LAM}}\right) \tag{2.32}$$

As seen in equations (2.31) and (2.32), the strain-energy release rate is independent of delamination size [2]. The magnitude of G only depends on the laminate layup and thickness, the location of the Terfenol-D sensor, the surrounding delamination region, the applied load, and the laminate width, w. It is worth noting that this initial Terfenol-D delamination model is piecewise continuous concerning the material properties. As the delamination region's cross-section exceeds the Terfenol-D sensor's cross-sectional area, the material response will vary as the matrix material will carry the load as the crack grows. That is:

$$G(t_x) = \begin{cases} G = \frac{P^2}{2mw^2}\left(\frac{1}{t_{TDS}E_{TDS}} - \frac{1}{tE_{LAM}}\right) & \text{if } t_{TDS} \leq t_x \leq \delta t_{TDS} \\ G = \frac{P^2}{2mw^2}\left(\frac{1}{t_{LD}E_{LD}} - \frac{1}{tE_{LAM}}\right) & \text{if } \delta t_{TDS} < t_x \end{cases} \tag{2.33}$$

where δ is the small perturbation symbol, t_x is the instantaneous delamination thickness, and t_{LD} and E_{LD} are the thickness and modulus of the post-initiated delamination.

2.3 Micromechanical Analysis of MagCFRP

When designing traditional fiber/matrix composites, understanding the mechanical properties of individual constituents in a composite material is essential as it directly influences the overall material properties and performance. The constituent's properties, such as stiffness, strength, coefficient of thermal and moisture expansion, volume fraction, etc., will affect the overall properties of the composite. As with any other composite system, it is possible to use mechanics of composite materials to parameterize global material properties of MagCFRP by methods of micromechanics of lamina.

Using the Composite Cylinder Assemblage (CCA) elasticity model, it is possible to express the elastic moduli in terms of composite constituent concentration and material properties. The primary assumption in a CCA model is the fibers have a circular cross-section and are assembled in a continuous periodic fashion throughout the laminate (MagCFRP CCA model depicted in Figure (2.3)). By this assemblage, the composite can be composed of repeating elements called representative volume elements (RVEs) [14]. The RVE theoretically represents the composite and its mechanical behavior. When using these composite cylinder elements, it is essential to use the appropriate boundary conditions that correspond to the elastic moduli being calculated.

To determine the MagCFRP elastic moduli along the fiber direction, let there exists an axial load, P, that is applied in the direction of the fibers. Due to this load P, there will also exist an axial stress, σ_1, in the direction of the fibers. Let is prescribed stress σ_1 be defined as:

$$\sigma_1 = \frac{P}{\pi c^2}. \tag{2.34}$$

σ_1 can also be defined in terms of Hooke's law such that:

$$\sigma_1 = E_1 \epsilon_1 \tag{2.35}$$

where E_1 and ϵ_1 are the longitudinal Young's modulus and the axial strain in the MagCFRP lamina in the direction of the fiber, respectively. Setting equations (2.34) and (2.35) equal to each other:

$$\begin{aligned} E_1 \epsilon_1 &= \tfrac{P}{\pi c^2} \\ E_1 &= \tfrac{P}{\pi c^2 \epsilon_1} \end{aligned} \tag{2.36}$$

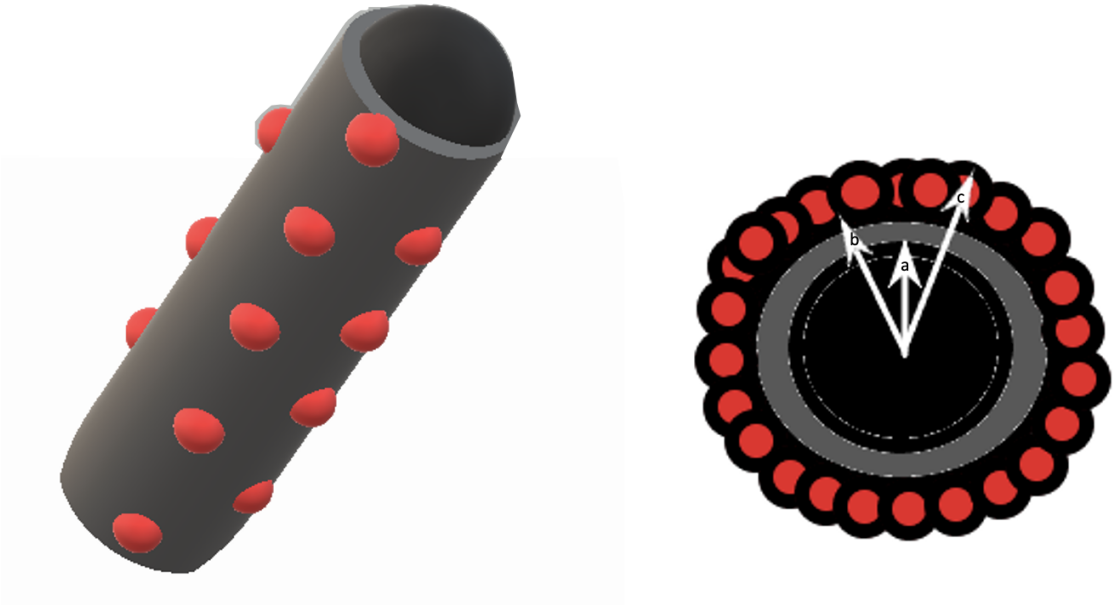

Figure 2.3: a. (left) Isometric view of MagCFRP assemblage. b. (right) Cross-sectional fiber view of MagCFRP assemblage ($a < b < c$).

To determine the MagCFRP's E_1 in terms of the material and geometrical properties of the fiber, matrix, and Terfenol-D constituents, the axial load, P, must be related to the axial strain, ϵ_1, by derivation. Using axisymmetric cylinder equilibrium conditions, the radial equilibrium equation can be expressed as:

$$\frac{d\sigma_r}{dr} + \frac{\sigma_r - \sigma_\theta}{r} = 0 \tag{2.37}$$

where σ_r and σ_θ are the radial and hoops stresses respectively. The classical normal stress-normal strain elasticity expression for an isotropic material with Young's modulus, E, and Poisson's ratio, υ, is given by:

$$\begin{bmatrix} \sigma_r \\ \sigma_\theta \\ \sigma_z \end{bmatrix} = \begin{bmatrix} \frac{E(1-\upsilon)}{(1-2\upsilon)(1+\upsilon)} & \frac{\upsilon E}{(1-2\upsilon)(1+\upsilon)} & \frac{\upsilon E}{(1-2\upsilon)(1+\upsilon)} \\ \frac{\upsilon E}{(1-2\upsilon)(1+\upsilon)} & \frac{E(1-\upsilon)}{(1-2\upsilon)(1+\upsilon)} & \frac{\upsilon E}{(1-2\upsilon)(1+\upsilon)} \\ \frac{\upsilon E}{(1-2\upsilon)(1+\upsilon)} & \frac{\upsilon E}{(1-2\upsilon)(1+\upsilon)} & \frac{E(1-\upsilon)}{(1-2\upsilon)(1+\upsilon)} \end{bmatrix} \begin{bmatrix} \epsilon_r \\ \epsilon_\theta \\ \epsilon_z \end{bmatrix} \tag{2.38}$$

In the $r - \theta - z$ coordinate system, the shear stresses and strains are zero for an axisymmetric

response. Defining the strain-displacement equations for an axisymmetric response:

$$\begin{aligned} \epsilon_r &= \tfrac{du}{dr} \\ \epsilon_\theta &= \tfrac{u}{r} \\ \epsilon_z &= \tfrac{dw}{dz} \end{aligned} \tag{2.39}$$

where u and w are the radial and axial displacements, respectively. Substituting the strain-displacement equation(s) (2.39) into the stress-strain equation (2.38), noting the $\epsilon_z = \epsilon_1$ everywhere gives:

$$\begin{bmatrix} \sigma_r \\ \sigma_\theta \\ \sigma_z \end{bmatrix} = \begin{bmatrix} \frac{E(1-\upsilon)}{(1-2\upsilon)(1+\upsilon)} & \frac{\upsilon E}{(1-2\upsilon)(1+\upsilon)} & \frac{\upsilon E}{(1-2\upsilon)(1+\upsilon)} \\ \frac{\upsilon E}{(1-2\upsilon)(1+\upsilon)} & \frac{E(1-\upsilon)}{(1-2\upsilon)(1+\upsilon)} & \frac{\upsilon E}{(1-2\upsilon)(1+\upsilon)} \\ \frac{\upsilon E}{(1-2\upsilon)(1+\upsilon)} & \frac{\upsilon E}{(1-2\upsilon)(1+\upsilon)} & \frac{E(1-\upsilon)}{(1-2\upsilon)(1+\upsilon)} \end{bmatrix} \begin{bmatrix} \frac{du}{dr} \\ \frac{u}{r} \\ \frac{dw}{dz} = \epsilon_1 \end{bmatrix} \tag{2.40}$$

Equation (2.40) can be simplified further by using stiffness coefficient notation such that:

$$\begin{bmatrix} \sigma_r \\ \sigma_\theta \\ \sigma_z \end{bmatrix} = \begin{bmatrix} C_{11} & C_{12} & C_{12} \\ C_{12} & C_{11} & C_{12} \\ C_{12} & C_{12} & C_{11} \end{bmatrix} \begin{bmatrix} \frac{du}{dr} \\ \frac{u}{r} \\ \epsilon_1 \end{bmatrix} \tag{2.41}$$

where:

$$\begin{aligned} C_{11} &= \tfrac{E(1-\upsilon)}{(1-2\upsilon)(1+\upsilon)} \\ C_{12} &= \tfrac{\upsilon E}{(1-2\upsilon)(1+\upsilon)} \end{aligned} \tag{2.42}$$

Substituting equation (2.41) into the equilibrium equation (2.37):

$$\frac{d^2u}{dr^2} + \frac{1}{r}\frac{du}{dr} - \frac{u}{r^2} = 0 \tag{2.43}$$

A solution to the linear ordinary differential equation (2.43) is found by assuming that:

$$u = \sum_{n=-\infty}^{\infty} A_n r^n. \tag{2.44}$$

Substituting equation (2.44) into equation (2.43) and simplifying yields:

$$\sum_{n=-\infty}^{\infty} (n-1)(n+1)A_n r^{n-2} = 0 \tag{2.45}$$

Equation (2.45) requires that $A_n = 0, n = -\infty, ..., \infty$, except for $n = 1$ and $n = -1$. Therefore, the form of the radial displacement is:

$$u = A_1 r + \frac{A_{-1}}{r}, \tag{2.46}$$

or more simply,

$$u = Ar + \frac{B}{r}, \tag{2.47}$$

These preceding equations are valid for a cylinder with an axisymmetric response. With this, the radial displacements, u_f, u_m, and u_{TDS} in the fiber, matrix, and Terfenol-D sensor cylinders, respectively, can be defined of the form:

$$u_f = A_f r + \frac{B_f}{r}, 0 \leq r \leq a \tag{2.48}$$

$$u_m = A_m r + \frac{B_m}{r}, a \leq r \leq c \tag{2.49}$$

$$u_{TDS} = A_{TDS} r + \frac{B_{TDS}}{r}, b \leq r \leq c \tag{2.50}$$

However, because the fiber is a solid cylinder and the radial displacement u_f is finite, B_f should equal 0. Otherwise, the radial displacement of the fiber u_f would be infinite. Thus:

$$u_f = A_f r, 0 \leq r \leq a \tag{2.51}$$

Differentiation equations (2.49), (2.50), and (2.51):

$$u_f = A_f \tag{2.52}$$

$$u_m = A_m + \frac{B_m}{r^2} \tag{2.53}$$

$$u_{TDS} = A_{TDS} + \frac{B_{TDS}}{r^2} \tag{2.54}$$

Substituting equation (2.52) into equation (2.41) with respect to the fiber components:

$$\begin{bmatrix} \sigma_r^f \\ \sigma_\theta^f \\ \sigma_z^f \end{bmatrix} = \begin{bmatrix} C_{11}^f & C_{12}^f & C_{12}^f \\ C_{12}^f & C_{11}^f & C_{12}^f \\ C_{12}^f & C_{12}^f & C_{11}^f \end{bmatrix} \begin{bmatrix} A_f \\ A_f \\ \epsilon_1 \end{bmatrix} \tag{2.55}$$

where:

$$\begin{aligned} C_{11}^{f} &= \tfrac{E_f(1-\upsilon_f)}{(1-2\upsilon_f)(1+\upsilon_f)} \\ C_{12}^{f} &= \tfrac{\upsilon_f E_f}{(1-2\upsilon_f)(1+\upsilon_f)} \end{aligned} \tag{2.56}$$

Similar stress-strain expressions can be formulated for the matrix and Terfenol-D sensor by substituting equations (2.53) and (2.54) into equation (2.41). Thus:

$$\begin{bmatrix} \sigma_r^m \\ \sigma_\theta^m \\ \sigma_z^m \end{bmatrix} = \begin{bmatrix} C_{11}^m & C_{12}^m & C_{12}^m \\ C_{12}^m & C_{11}^m & C_{12}^m \\ C_{12}^m & C_{12}^m & C_{11}^m \end{bmatrix} \begin{bmatrix} A_m - \frac{B_m}{r^2} \\ A_m + \frac{B_m}{r^2} \\ \epsilon_1 \end{bmatrix} \tag{2.57}$$

where:

$$\begin{aligned} C_{11}^{m} &= \tfrac{E_m(1-\upsilon_m)}{(1-2\upsilon_m)(1+\upsilon_m)} \\ C_{12}^{m} &= \tfrac{\upsilon_m E_m}{(1-2\upsilon_m)(1+\upsilon_m)} \end{aligned} \tag{2.58}$$

and

$$\begin{bmatrix} \sigma_r^{TDS} \\ \sigma_\theta^{TDS} \\ \sigma_z^{TDS} \end{bmatrix} = \begin{bmatrix} C_{11}^{TDS} & C_{12}^{TDS} & C_{12}^{TDS} \\ C_{12}^{TDS} & C_{11}^{TDS} & C_{12}^{TDS} \\ C_{12}^{TDS} & C_{12}^{TDS} & C_{11}^{TDS} \end{bmatrix} \begin{bmatrix} A_{TDS} - \frac{B_{TDS}}{r^2} \\ A_{TDS} + \frac{B_{TDS}}{r^2} \\ \epsilon_1 \end{bmatrix} \tag{2.59}$$

where:

$$\begin{aligned} C_{11}^{TDS} &= \tfrac{E_{TDS}(1-\upsilon_{TDS})}{(1-2\upsilon_{TDS})(1+\upsilon_{TDS})} \\ C_{12}^{TDS} &= \tfrac{\upsilon_{TDS} E_{TDS}}{(1-2\upsilon_{TDS})(1+\upsilon_{TDS})} \end{aligned} \tag{2.60}$$

In order to determine the unknown constants A_f, A_m, A_{TDS}, B_m, B_{TDS}, and ϵ_1, the following six boundary and interface conditions must be implemented:

1. The radial displacement is continuous at the fiber-matrix interface, $r = a$:

$$u_f(r = a) = u_m(r = a). \tag{2.61}$$

Then, from equation (2.49) and (2.51):

$$A_f a = A_m a + \frac{B_m}{a} \tag{2.62}$$

2. The radial displacement is continuous at the matrix-Terfenol-D sensor interphase, $r = b$:

$$u_m(r=b) = u_{TDS}(r=b). \tag{2.63}$$

Then, from equation (2.49) and (2.50):

$$A_m b + \frac{B_m}{b} = A_{TDS} b + \frac{B_{TDS}}{b} \tag{2.64}$$

3. The radial stress is continuous at the fiber-matrix interphase, $r = a$:

$$\sigma_r^f(r=a) = \sigma_r^m(r=a). \tag{2.65}$$

Then from equations (2.55) and (2.57):

$$C_{11}^f A_f + C_{12}^f A_f + C_{12}^f \epsilon_1 = C_{11}^m \left(A_m - \frac{B_m}{a^2} \right) + C_{12}^m \left(A_m + \frac{B_m}{a^2} \right) + C_{12}^m \epsilon_1 \tag{2.66}$$

4. The radial stress is continuous at the matrix-Terfenol-D sensor interphase, $r = b$:

$$\sigma_r^m(r=b) = \sigma_r^{TDS}(r=b). \tag{2.67}$$

Then from equations (2.57) and (2.59):

$$\begin{aligned} &C_{11}^m \left(A_m - \tfrac{B_m}{b^2} \right) + C_{12}^m \left(A_m + \tfrac{B_m}{b^2} \right) + C_{12}^m \epsilon_1 = \\ &C_{11}^{TDS} \left(A_{TDS} - \tfrac{B_{TDS}}{b^2} \right) + C_{12}^{TDS} \left(A_{TDS} + \tfrac{B_{TDS}}{b^2} \right) + C_{12}^{TDS} \epsilon_1 \end{aligned} \tag{2.68}$$

5. Because the surface at $r = c$ is traction free, the radial stress on the outside of the matrix surface, $r = c$, is zero:

$$\sigma_r^m(r=c) = 0 \tag{2.69}$$

Then, equation (2.57) gives:

$$C_{11}^m \left(A_m - \frac{B_m}{c^2} \right) + C_{12}^m \left(A_m + \frac{B_m}{c^2} \right) + C_{12}^m \epsilon_1 = 0 \tag{2.70}$$

6. The overall axial load over the fiber-matrix-Terfenol-D sensor cross-sectional area in the fiber direction is the applied load, P, then:

$$\begin{aligned} &\int_A \sigma_z dA = P \\ &\int_0^c \int_0^{2\pi} \sigma_z d\theta r dr = P \end{aligned} \tag{2.71}$$

Integrating (2.71):

$$\int_0^c \sigma_z 2\pi r dr = P. \tag{2.72}$$

Now,

$$\begin{aligned} \sigma_z &= \sigma_z^f, 0 \leq r \leq a \\ &= \sigma_z^m, a \leq r \leq c \\ &= \sigma_z^{TDS}, b \leq r \leq c \end{aligned} \tag{2.73}$$

Then, from equations (2.55), (2.57), and (2.59):

$$\begin{aligned} &\textstyle\int_0^a (C_{12}^f A_f + C_{12}^f A_f + C_{11}^f \epsilon_1) 2\pi r dr + \\ &\textstyle\int_a^c \left(C_{12}^m \left(A_m - \frac{B_m}{r^2}\right) + C_{12}^m \left(A_m + \frac{B_m}{r^2}\right) + C_{11}^m \epsilon_1\right) 2\pi r dr + \\ &\textstyle\int_b^c \left(C_{12}^{TDS} \left(A_{TDS} - \frac{B_{TDS}}{r^2}\right) + C_{12}^{TDS} \left(A_{TDS} + \frac{B_{TDS}}{r^2}\right) + C_{11}^{TDS} \epsilon_1\right) 2\pi r dr = P \end{aligned} \tag{2.74}$$

Solutions for A_m, A_f, A_{TDS}, B_m, and B_{TDS} are provided in Appendix A. Using the solutions for A_m, A_f, A_{TDS}, B_m, and B_{TDS} and substituting them into equation (2.74) and integrating will allow ϵ_1 to be defined in terms of material properties and P. Using equation (24) in Appendix A and substituting it into equation (2.36), it is possible to arrive at an analytical solution for E_1. Please see Appendix A for more details.

2.4 MagCFRP Deposition Protocols

One of the most critical steps in fabricating MagCFRP is the Terfenol-D sensor deposition process. How the sensors are embedded between lamina ply will drastically affect the magnetization response and material properties. Careless deposition can lead to diminished performance and premature failure. This work has three primary non-magnetically alignment deposition methods for fabricating MagCFRP. These methods include sprinkling, pre-preg b-stage, and sputtering. It is worth noting that micro and nano-size Terfenol-D sensors are pyrophoric. All deposition methods

in this work were performed in an inert gas environment (i.e., glove box).

When depositing Terfenol-D sensors in a MagCFRP laminate, it is essential to consider magnetic dipole moment pre-alignment. The inspiration for pre-aligning the magnetic dipole moments pre-polymerization came from magnetostrictive researchers such as Hamann [10] and Shanmugham [32], who have shown pre-aligning the dipole moment of magnetostrictive material will yield a more significant response to induced magnetization [24, 41, 17]. The pre-aligning magnetic dipole moments of the embedded Terfenol-D material can be visualized in the pre and post-SEM images taken by Shanmugham of Terfenol-D sensors in an epoxy matrix, as shown in Figure (2.4). As depicted in Figure (2.4b), the interphacial crack density of the non-magnetically aligned Terfenol-D sensors is twice as much and more fragmented when compared to the pre-aligned Terfenol-D sensors (Figure (2.4c)). Shanmugham and Bailey suggest that this high crack density interphacial failure seen in Figure (2.4b) is likely due to the low tensile strength of the ground sensors. Increasing the tensile strength of the particle should improve interphacial resilience.

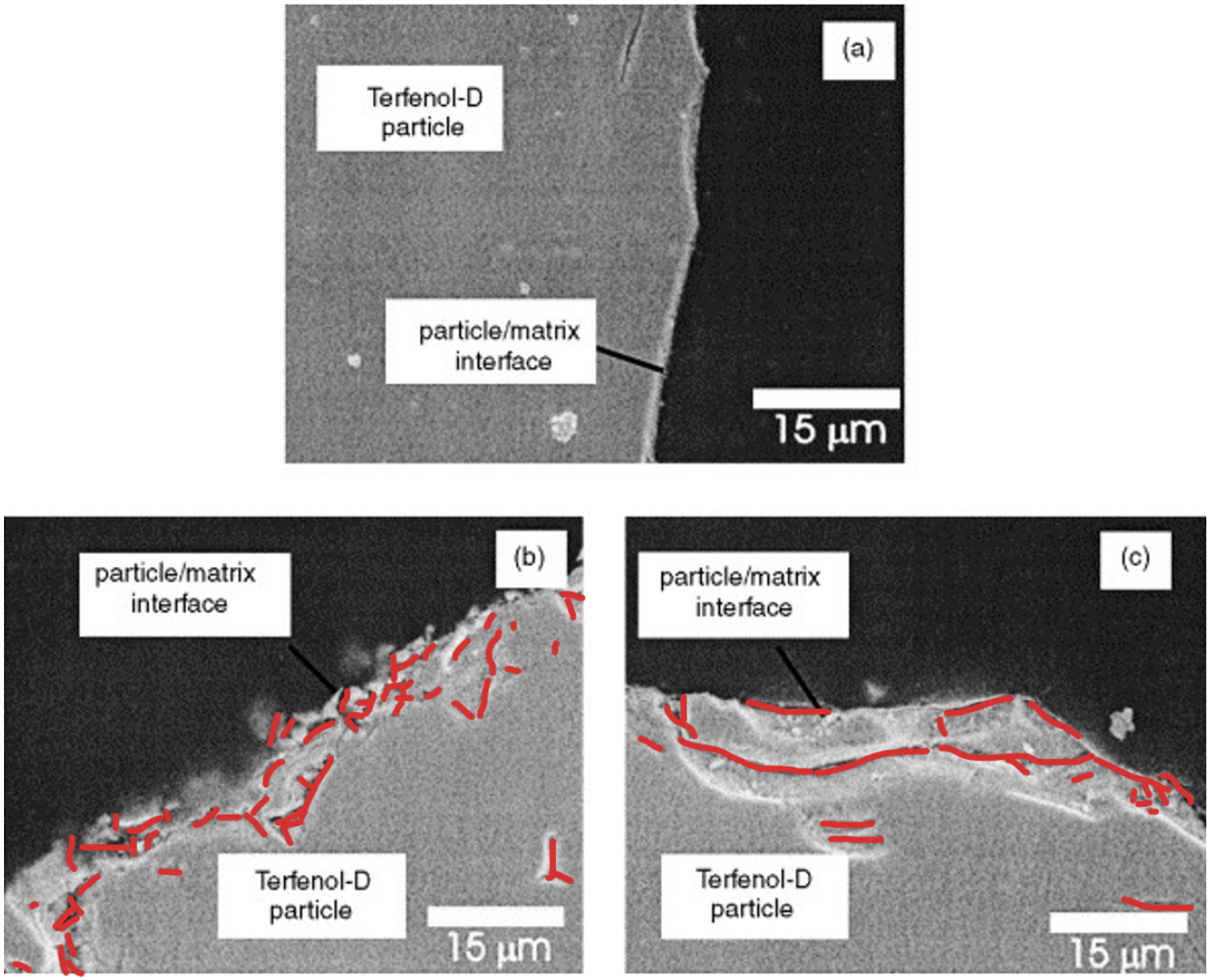

Figure 2.4: (Crack formations are highlighted in red) a. Pristine Terfenol-D-matrix interphase. b. Terfenol-D-matrix interphase for non-magnetically aligned sample. c. Terfenol-D-matrix interphase for magnetically align sample [32].

2.4.1 Sprinkling Deposition

Sprinkling deposition involves "sprinkling" a prescribed amount of Terfenol-D sensors between lamina plies. The sprinkling deposition process is effective in physically depositing Terfenol-D sensors in a composite. However, it does not allow a high level of homogeneity of sensor deposition. Early MagCFRP samples were produced using the sprinkling method, but newer advanced deposition methods are currently being studied and implemented into the MagCFRP fabrication process.

2.4.2 Pre-preg b-stage Deposition

Pre-preg CFRPs are the standard for producing high-grade composite materials in various industries. Pre-pregs are pre-impregnated fiber-matrix tape that is ready to use in laminate stacking. Once the pre-preg laminate is stacked, it can be immediately vacuum bagged for pressure and temperature-controlled curing. Figure (2.5) shows the process of how pre-pregs are made.

In this process, a row of fibers is passed through a resin bath, where the resin impregnates the fibers. The "wet" fibers are then passed through a heating sector to advance the polymerization process from a-stage to b-stage. Thermosetting resins have three curing stages: A, B, and C. Resins are manufactured in the a-stage, where the resin may transition into a solid or liquid phase but can flow when low to moderate heat is applied. The a-stage is sometimes referred to as the uncured stage. At the a-stage, there is no polymer cross-linking established.

The b-stage of pre-preg manufacturing is the middle stage of the thermosetting chemical reaction, where the resin is partially cured for ease of use during shipping, handling, and fabrication. The OH groups partially functionalize the polymer chains, creating a higher molecular weight material. The final stage of the thermoset polymerization process is the c-stage. During the c-stage, the laminate layup is complete, and the material is cured for thermosetting processing. At this point of polymerization, the polymer chains are completely cross-linked, which results in irreversible hardening and insolubility.

The b-stage pre-preg manufacturing method has the most significant potential to be used in MagCFRP mass production. The only phase that would need to be updated to transition a current pre-preg manufacturing process to produce MagCFRP pre-preg is introducing the Terfenol-D sensors directly in the resin bath under continuous mixing conditions. Introducing these sensors

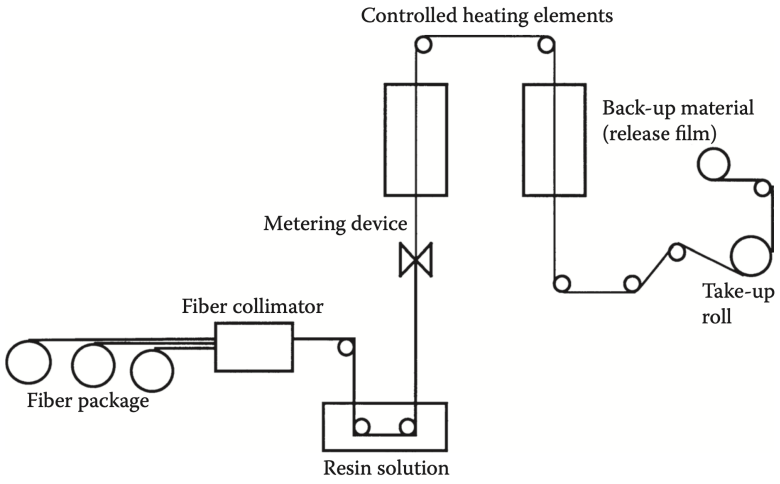

Figure 2.5: Pre-preg manufacturing process [14].

in the resin bath will allow the Terfenol-D sensor's composite geometric parameters to be controlled and updated when necessary. This update in the pre-preg manufacturing process can be visualized in Figure (2.6). As seen in Figure (2.6), the resin solution now has Terfenol-D sensors well mixed within the solution. Once this a-stage fiber, matrix, and Terfenol-D sensor composite passes through the controlled heating elements, the material can be backed with release film and rolled up as a MagCFRP pre-preg.

It is worth noting that this method is a global deposition process, meaning Terfenol-D sensors will be deposited continuously throughout the entire roll. The addition of Terfenol-D sensors in a composite system will affect the material and mechanical properties (e.g., density and Young's modulus). For applications where mass and weight optimization is essential, it is recommended that the MagCFRP lamina sheets primarily be used in regions where delamination density tracking is paramount (i.e., high-stress-strain geometrical areas). Using MagCFRP lamina in this manner allows the exploitation of composite engineering methods, as the application-specific design aspect is where the true beauty of composite materials lies.

2.4.3 Thin Film Deposition

Physical Vapor Deposition (PVD) is a method for depositing thin films onto a substrate by converting a solid material into vapor and then condensing it onto the substrate's surface. Sputtering is a specific type of PVD. Sputtering is widely used to deposit various materials, including metals,

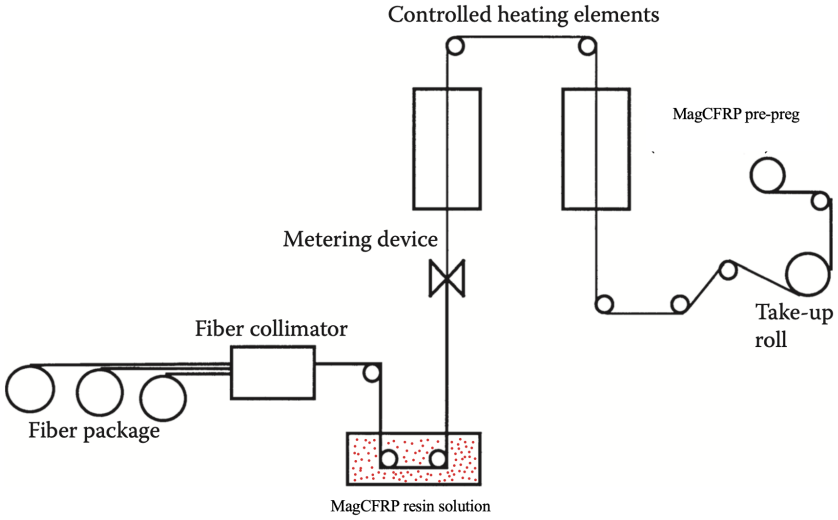

Figure 2.6: Updated pre-preg manufacturing process for MagCFRP.

semiconductors, ceramics, and even complex compounds. It offers good film uniformity, excellent adhesion, and compatibility with large-area deposition. During the sputtering process, high-energy ions dislodge atoms or molecules from the target surface by raw impact of the target material. These dislodged sensors then travel and deposit onto the substrate, forming a thin film [4].

In a vacuum chamber, plasma is created by introducing a suitable gas, such as argon. The gas is ionized, and the positively charged ions are accelerated toward the target material [4]. In depositing Terfenol-D sensor film onto CFRP, the target material would be bulk Terfenol-D. When the high-energy ions collide with the target surface, they transfer momentum to the atoms or molecules in the target material, causing them to be ejected or sputtered. These sputtered sensors are then free to travel and deposit on the substrate (i.e., CFRP pre-preg), creating a thin film.

The substrate is usually held at a lower temperature to aid film formation and control its properties. Sputtering has shown promising results in surface Terfenol-D thin film sensor deposition on 3D printed composite materials. These results will be discussed in greater detail in Chapter 3.

2.4.4 Field Structured Magnetoelastomers

Magnetoelastomers are a type of smart material that can change their shape in response to a magnetic field. They are made of a magnetic filler, such as Terfenol-D sensors, embedded in an elastomeric matrix. When a magnetic field is applied to the material, the magnetic sensors align

with the field, causing the material to change shape.

Magnetoelastomers have potential applications in various fields, including robotics, biomedicine, and energy harvesting. One of the advantages of magnetoelastomers is their ability to be tuned to respond to specific magnetic fields. This allows precise control over their shape change, making them ideal for sensitive applications. Additionally, they are relatively easy and inexpensive to produce, making them an attractive option for various industries.

"Magnetostriction of field-structure magnetoelastomers" by J. Martin et al. presents the science and implementation of multidimensional AC magnetic fields for organizing and structuring magnetic sensors into complex structures during polymerization. Using this technique, one can achieve a variety of structures that can be produced by this field-structuring method, including but not limited to particle chains, sheets, networks, and honeycombs. The sheet structure is the structure of interest in this current iteration of the MagCFRP work.

Terfenol-D sensors oriented orthogonal to the applied field have the greatest magnetization differential potential in delamination formation applications (i.e., max magnetic moment potential). At this orientation, flux leakage will be prominent and noticeable. Another reason particle sheets would be a superior field structuring orientation is that particle sheets exhibit a minimal magnetostrictive response when the field is applied normally to the sheets [21]. The MagCFRP work is not as concerned with magnetostriction as a physical magnetically deformable system but more so with the localized magnetostrictive sensitivity concerning changes in magnetization (i.e., damage). This is because magnetizable sensors in an elastic continuum can exhibit significant magnetostrictive stresses and strains if suitably arranged [21].

Using the field structuring method to produce magnetoelastomer Terfenol-D sheets will allow b-stage "sensor coupons" to be embedded between CFRP ply regions to create semi-MagCFRP structures. Producing and subsequently embedding the magnetoelastomer coupons throughout a structural laminate would allow highly structured NDE Terfenol-D sensors to be embedded with superior fidelity at damage-sensitive regions (i.e., high-stress-strain regions). These field-structured sheets are formed by using a biaxial magnetic field. A composite structured into sheets will have a unique axis normal to the sheets. Terfenol-D sensors were structured into sensor sheet magnetoelastomers using Dr. Dereje Seifu's (Professor at Morgan State University, Department of Physics) Magneto-optic Kerr effect (MOKE) biaxial field magnet. This system utilizes a GWM 5201 electromagnet that generates up to a 0.7 T multi-axial magnetic flux density in a thin planar volume near

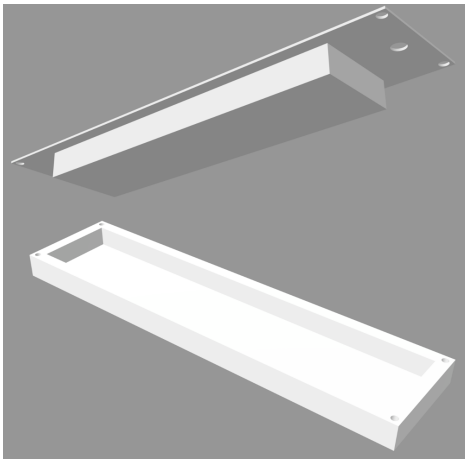

Figure 2.7: Two-part silicon mold dye for magnetoelastomer fabrication.

the magnetic source.

A two-part silicone mold die was designed and manufactured using SolidWorks and a 3D printer before the magnetoelastomer field structuring method could be used to produce sensor sheets (Figure (2.7)). The mold die's surfaces were wet sanded using 2000 grit sandpaper to ensure a smooth finish before pouring "Let's Resin's" silicone mold rubber into the two-part 3D printed mold die for curing. As mentioned earlier, due to Terfenol-D's pyrophoric nature, a 30-weight percent (wt%) Terfenol-D-resin slurries were mixed in an inert gas glovebox before the magnetoelastomer field structuring fabrication. Once Terfenol-D is passivated with a resin coating, it is safe to work with in oxygenated environments.

GMW Associates provides biaxial magnetic field data concerning the x direction for a $40mm$ region centered at the magnet's core. The variance in the B_x and the B_z magnetic flux densities centered around the core can be visualized in Figure (2.8). Using the B_x and B_z curves, scaled magnetic flux density field vectors can be calculated and used to determine how the resultant field directions change with x.

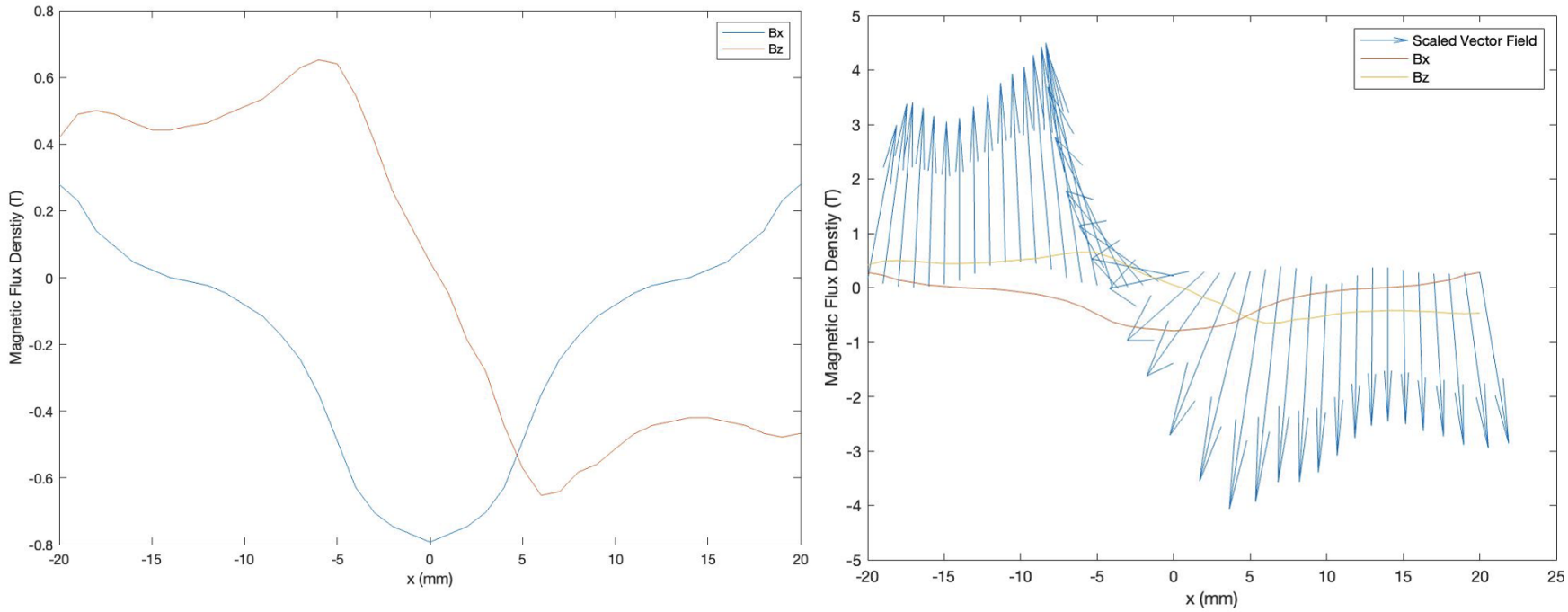

Figure 2.8: a. GWM 5201 electromagnet vector component potential with respect to longitudinal displacement. b. GWM 5201 electromagnet vector component potential and scaled vector field with respect to longitudinal displacement.

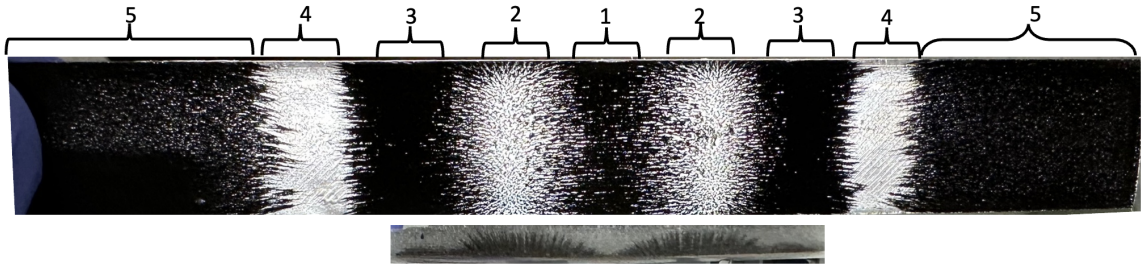

Figure 2.9: a. (top) Slurry A surface normal view (backed by a light source) of the field structured magnetoelastomer. b (bottom) Slurry A transverse cross-section view of the field structured magnetoelastomer.

Two Terfenol-D sensor slurries were used to study and implement the b-stage field structuring method (specific resin material properties can be found in the appendix). Slurry A used a two-part epoxy mount resin that cured at room temperature. Slurry B used a high-purity bisphenol A two-part epoxy resin that does not cure at room temperature. Since slurry A cured at room temperature, it was used first to study the field structure of the Terfenol-D magnetoelastomer. As seen in Figure (2.9), a five-phase field structuring was observed in the slurry A magnetoelastomer. The physically observed field structuring agreed well with the generated vector field based on the data prescribed by GMW. It must be noted that the calculated vector field does not encapsulate all five field structuring phases, as three of the five phases are outside of the 40mm vector field region. However, only one of the three phases outside the defined vector field is structured. As seen in Figure (2.8), phase one is the inflection phase (associated with the $x = 0mm$ region 1 in Figure (2.9) and region 1 in Figure (2.10)), phase two is the $\approx 90^o$ phases (associated with the $-20mm \leq x \leq 20mm$ regions 2 in Figure (2.9) and region 2 in Figure (2.10)), phase three is the $\approx 0^o$ sheet field structured phase (associated with the region 3 in Figure (2.10)), phase four is a resin phase (associated with the region 4 in Figure (2.10)), and phase five is an amorphous slurry phase (associated with the region 5 in Figure (2.10)).

Slurry B produced a sheet-structured Terfenol-D sensor b-stage coupon for MagCFRP. Since slurry B does not cure at room temperature, the solution was first introduced to a magnetic field for structuring. Once the Terfenol-D sensors were structured, the magnetic field was removed, and the silicone mold was placed in an oven for b-stage curing. Figure (2.10b) shows that an $\approx 15mm$ sheet structured Terfenol-D sensor b-stage coupon was cut out of the malleable five-phase

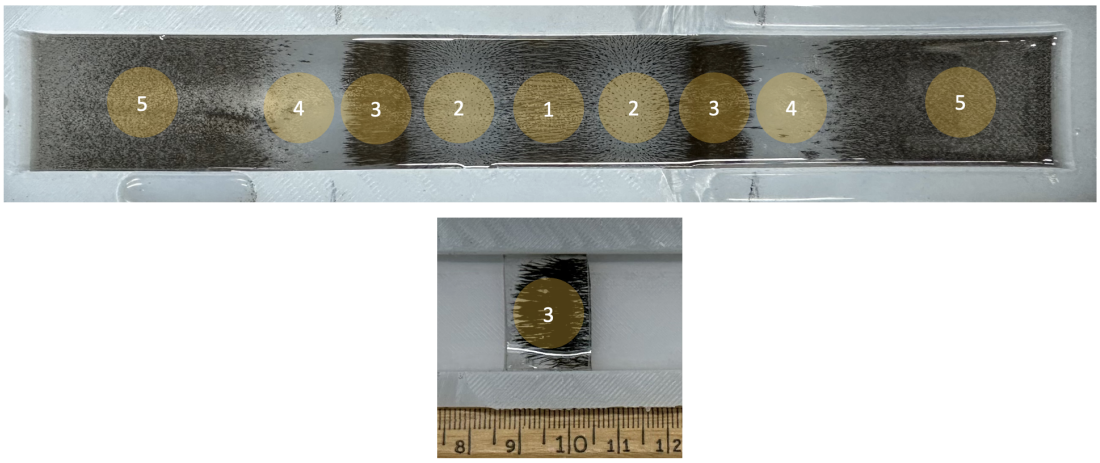

Figure 2.10: a. (top) Slurry B a-stage field structuring phases. b. (bottom) Slurry B b-stage sheet field structured magnetoelastomer coupon.

magnetoelaastomer. This coupon was then embedded in just the resin from slurry B for c-stage curing and subsequent testing. The process can be depicted in Figure (2.11).

2.5 Magnetization Stimulation of MagCFRP Systems

Magnetometry sensor efficacy is essential for MagCFRP to be used in a workflow environment (e.g., condition-based maintenance and real-time SHM protocols). Just as MagCFRP needs structural integrity, so does the MagCFRP magnetometry sensor that detects changes in magnetization. This MagCFRP magnetometry sensor must be robust and reliable in various environments and applications. Electromagnetic and indirect magnetization approaches are the two fundamental magnetometry sensor methods studied and utilized in the MagCFRP development. Both ways have shown the ability to track changes in magnetization. However, recent work has used indirect magnetization over electromagnetic stimulation due to the system's resolution, reliability, and simplicity.

2.5.1 Electromagnetic Stimulation

When a current flows through a coiled copper wire, it generates a magnetic field around the wire, according to Ampere's law. Ampere's law states that the magnetic field produced by a

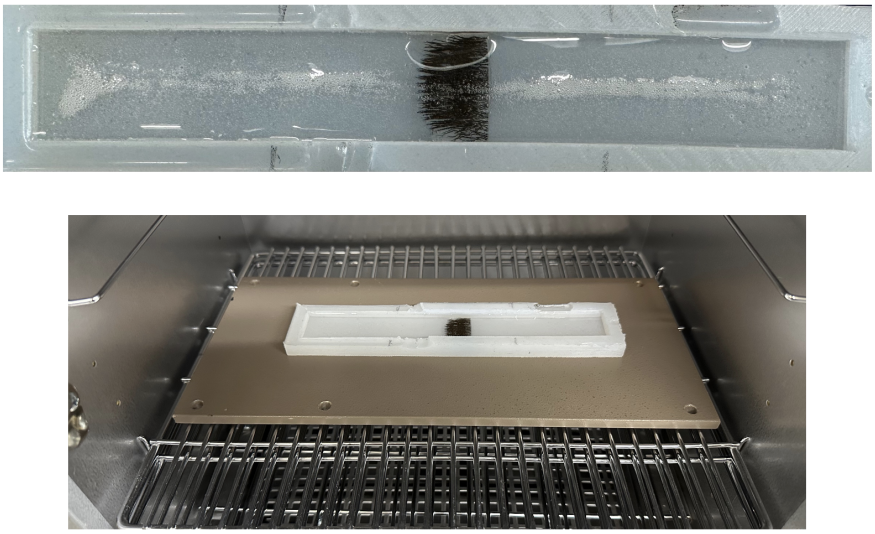

Figure 2.11: a. (top) Silicon mold containing epoxy resin embedded with b-stage sheet field structured magnetoelastomer coupon. b. B-stage curing processing in a small lab oven.

current-carrying wire is directly proportional to the current and the number of turns in the wire coil. Mathematically, it can be represented as:

$$\oint B_i \cdot dl_i = \mu_0(I) \tag{2.75}$$

where B is the magnetic field, dl is the change in length along a wire, μ_0 is the permeability of free space, and I is the current passing through a wire.This fundamental principle of electromagnetism was used to develop an electromagnetic magnetometry sensor termed the driving coil-pickup coil arrangement by Haile et al. [9]. The premise of this driving coil-pickup coil system is the generate an alternating magnetic field on the MagCFRP material. Using a larger diameter magnetic coil driving the magnetization (i.e., driving coil) and a smaller diameter magnetic coil recording the change in magnetization response (i.e., pickup coil), MagCFRP can be stimulated and scanned for damage. By observing the change in current over time, it is possible to track changes in the voltage frequency (using Faraday's Law) with respect to material stress and strain. The driving coil pickup coil arrangement can be visualized in Figure (2.12). It is worth noting that electromagnetic magnetization requires a Fast Fourier Transform (FFT) algorithm in post-processing to analyze the voltage RMS response.

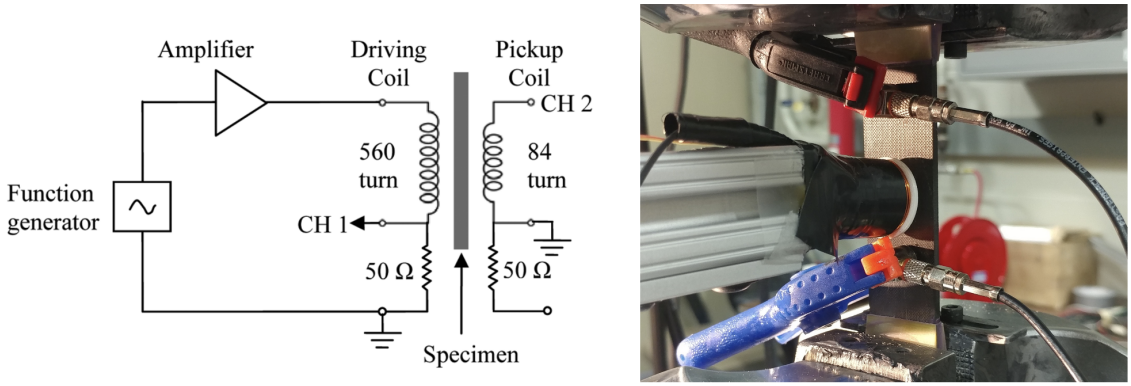

Figure 2.12: a. (left) Driving coil-pickup coil circuit schematic. b. (right) Picture of the physical driving coil-pickup coil system [9].

2.5.2 Indirect Magnetization Stimulation

Indirect magnetization stimulation of MagCFRP is a magnetization technique that uses a permanent or DC magnetic field to activate the embedded Terfenol-D sensor for localized damage detection. While electromagnetic magnetization is more likely to be implemented in workflow applications, indirect magnetization techniques have superior clarity for research and design environments. The Latest iteration of MagCFRP research utilizes a permanent neodymium magnet to provide a driving magnetic flux density on test specimens. As mentioned earlier, a traditional hall generator probe captures the projected magnetization from the MagCFRP. This indirect magnetization-magnetometry method can be visualized in Figure (1.7).

To ensure reliable and concentric indirect magnetization-magnetometry, a two-part C-Clamp bracket to hold a permanent neodymium magnet was designed and 3D printed to be attached to the Hall generator probe. The distance between the Hall generator probe and the magnet can be adjusted by sliding the clamp up or down on the probe shaft. The C-Clamp can be seen in Figure (2.13).

2.6 MagCFRP in an Atomistic Environment

Fracture generally occurs when the crack tip stresses overcome cohesive forces that keep neighboring atoms or molecules at equilibrium spacing. In a MagCFRP system, the cohesive force of

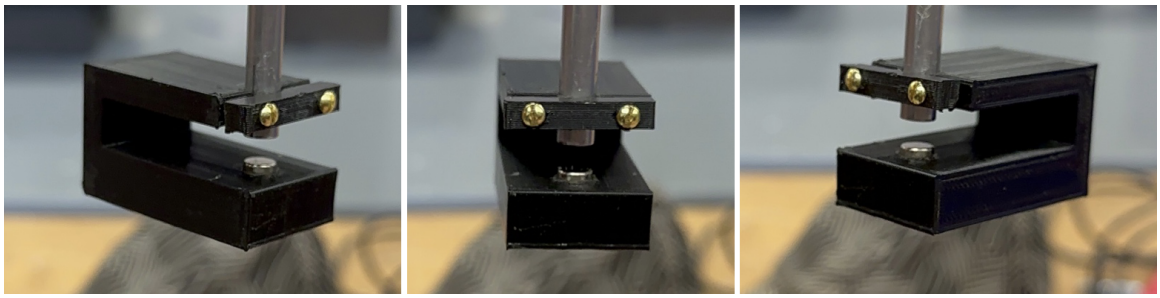

Figure 2.13: Two part indirect magnetization 3D printed c-clamp.

predominant interest is the cohesive force and stress of the Terfenol-D and the epoxy resin molecules. Figure (2.14) depicts a molecule schematic of a Terfenol-D sensor attached to pre-preg IM7 8552 resin.

In Figure 2, x_0 is the equilibrium spacing between the Terfenol-D and 8552 epoxy molecules, and λ is the bond energy wavelength between the Terfenol-D and 8552 molecules. Once the cohesive stress is overcome by external mechanical stress, there will be a release of bond energy. Bond energy is released when a fracture occurs, and new surfaces are created. Because of Terfenol-D's magneto-mechanical coupling and the Villari effect, this release in bond energy will relate to a localized change in the magnetic flux density during scanning. Using computational atomistic testing methods, like Molecular Dynamics (MD), could drastically accelerate the understanding of MagCFRP's nano and micro mechanics.

2.6.1 Dissipative Particle Dynamics for MagCFRP

Course-Grain Molecular Dynamics (CGMD) methods, such as Dissipative Particle Dynamics (DPD), can be used to study the behavior of complex polymer configurations like MagCFRP. DPD is a computational simulation method used to study the behavior of complex fluids, such as polymers, colloids, and biological systems. It is particularly suitable for systems with mesoscopic length and time scales, where the interactions between individual sensors are important. In DPD simulations, the fluid is represented by a collection of sensors, each representing a group of molecules. These sensors interact with each other through pairwise potentials consisting of conservative, dissipative, and random forces. The conservative force ensures that the sensors maintain their overall structure and shape, while the dissipative force dissipates energy from the system and allows for energy

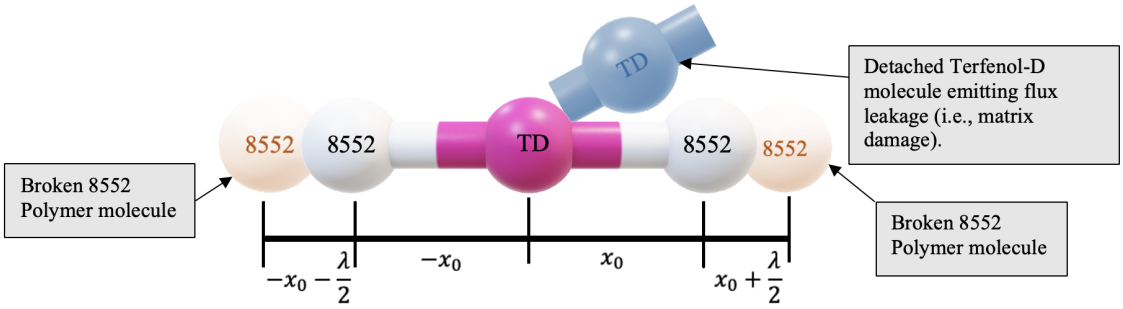

Figure 2.14: Molecular diagram of Terfenol-D bonded with 8552 molecules at equilibrium and cohesive spacing.

exchange between sensors. The random force introduces thermal fluctuations into the system.

DPD simulations are often used to study phenomena such as self-assembly, phase separation, rheology, and transport properties of complex fluids. They can provide insights into the dynamics and behavior of systems that are difficult to study experimentally or through other simulation methods. The DPD method has its limitations, as it is an approximation of the underlying molecular interactions and may not capture all the details of a system accurately. However, it has proven to be a valuable tool for understanding the behavior of soft matter and complex fluids and has found applications in various fields, including materials science, biophysics, and nanotechnology.

One feature of particular interest that could be captured relatively straightforward based on the "Dissipative particle dynamics simulation of microphase separation in polyurethane urea nanocomposites" by Dr. Yelena Sliozberg (2020) is capturing the thermodynamic compatibility between the resin matrix of MagCFRP and Terfenol-D sensors. For example, Sliozberg et al. [35] have shown that with increasing polymer density and wt% of CNT in polyurethane urea (PUU) nanocomposites, a thermodynamic incompatibility will arise in the form of phase separation of hard and soft domains in PUU.

Surprising in this work, the microphase separation of PUU blocks was favorable because it led to a rise of free volume and consequently increased conformational entropy of the flexible soft blocks where the hard domains form nano-phase columns between CNTs. Analogous to this PUU/CNT thermodynamics incompatibility would be to use DPD to study the morphology and compatibility of continuous carbon fiber immersed in a DGEBA-DDM/Terfenol- D medium.

2.6.2 Density Functional Theory (DFT) for MagCFRP

Density Functional Theory (DFT) is a computational quantum mechanical method used to study the electronic structure and properties of atoms, molecules, and solids. It provides a practical approach to solving the Schrödinger equation. The Schrödinger equation is a fundamental equation in quantum mechanics that describes the behavior of quantum systems, such as atoms, molecules, and subatomic sensors.

Using DFT to solve the Schrödinger equation uses a method of electron density fields rather than solving for the wave function of the entire system. One compelling use case for DFT is its ability to be used as a pipeline to computationally generate interphacial properties for multiphase composite systems, such as the MagCFRP magnetoelastomer system (Terfenol-D- epoxy system). A recent work titled "Interface binding and mechanical properties of MXene- epoxy nanocomposites" by Sliozberg et al. uses DFT to predict the structural and electronic properties of MXene-epoxy interphase under uniaxial tension. The work used DFT to evaluate the binding energies (cohesive forces) and how they vary with different molecule constructions, mainly terminal groups, coverage factors, and filler flake size and orientation.

Sliozberg et al.'s approach is to employ a multi-scale model method to study the atomistic and continuous behavior of Titanium base MXene-epoxy nanocomposites. The authors mention while there are limitations on the results due to length and time scale constraints, the results show microscale mechanisms of MXene-epoxy mechanical improvement in isolation of macroscale factors. Their computational results are compared with experimental findings on the MXene-epoxy nanocomposite.

The primary assumption made by Sliozberg et al. DFT model was to have the adsorption (the process by which a solid holds molecules of a gas or liquid or solute as a thin film) of one molecule of the lowest energy conformer of DGEBA on a well-separated slab of a single layer of MXene [34]. Similarly, in the MagCFRP work, the question arises if the same approach/assumption where a surface/slab of Terfenol-D adsorps one molecule of the lowest energy conformer of DGEBA. With this, it may be possible to define the binding energy of the MagCFRP-epoxy system.

With cohesive properties generated by DFT simulation, it would be possible to take a similar approach to Sliozberg et al. and employ CGMD simulations of polymer networks with embedded Terfenol-D sensors/flakes/filler using the standard bead-spring "Kremer-Grest" model.

In the aforementioned work, the model used was made from two types of constituents 1) three-dimensional highly cross-linked polymer networks and 2) two-dimensional filler sheets. It is worth mentioning that Terfenol-D can be manufactured into micro flakes as well, but it would come at a price of increased risk of combustion due to its pyrophoric nature. In their simulations, each flake was treated as an independent rigid body, so the set of sensors composing the flakes moved as a single entity, independent from other molecules.

2.6.3 Atomistic Feasibility of MagCFRP

When representing physical materials like Terfenol-D and resin epoxy in an atomistic simulation environment, one must consider the plethora of system parameters that must be defined to run the simulation. These parameters can range from straightforward box size and boundary conditions to solubility and functionalization parameters. Many of these MD simulation parameters are defined by experimental data from the literature. In the field of magnetostrictive materials like Terfenol-D, there are limited resources that provide material characteristics presented for atomistic simulations. L A Makarova et al. of "Tunable layered composites based on magnetoactive elastomers (MAE) and piezopolymer for sensors and energy harvesting devices" has stated that it is generally impossible to model MAE materials at an atomistic or molecular scale [7]. They mention other macro-scale methods could represent the movements of magnetic and non-magnetic material while the MD environment acts as a computer simulator, but there are no direct MD techniques.

In other works, like "Coarse-grained molecular dynamics simulation of small ferrogel objects" by A. V. Ryzhkov et al., the authors model soft (modulus on the scale of kPa) ferrogels with MD simulation. In this work, the magnetic grains are linked to the monomers by means of special (lock) sensors [30]. These special sensors are rigidly locked to their "master" grains. After researching different atomistic methods, it was determined that it is currently impossible to model MagCFRP without compromising scientific rigor.

2.7 MagCFRP in an FEA Enviroment

Finite Element Analysis (FEA) is a numerical technique used to analyze and solve unknowns in engineering systems. It itself deploys the finite element method (FEM), which is a numerical approach for approximating and solving differential equations governing the behavior of these systems.

Unlike classical mechanics of material methods, which require bulk material property definitions for the geometry of interest, FEA allows user-defined discretization based on sub-geometric constraints. By this, discretized elements can have unique material properties based on global and relative positioning. Composite materials have geometric-specific material properties by nature, making the FEA method a good candidate for solving the magnetoelasticity behavior that exists in MagCFRP systems.

The MagCFRP FEA was carried out in COMSOL. COMSOL is an FEA package that specializes in multiphysics platforms. Since Terfenol-D is a magnetostrictive material, COMSOL allows the magnetoelastic coupling to be studied in parallel. Although the Terfenol-D sensors in practice are amorphous in shape, the sensors in the FEA are assumed to be circular in shape. Modeling a laminate with ferroic constituents, externally applied loads, and magnetic fields will help better understand the formation and progression of delamination density propagation in MagCFRP.

2.7.1 COMSOL for MagCFRP

The model's geometry was constructed on the microscale level with homogenous and isotropic conditions. An indeterminate condition was assumed initially, so there are no initial displacement, velocity, or rotational fields. The accepted radii for each Terfenol-D sensor and ply thickness was 120 microns. All micro-sensors were created with uniform shapes. This geometry initialization can be visualized in Appendix B Figure (1).

After the geometry had been established in the model, the solid mechanic state of the composite was initialized. This initialization included defining constituent mechanical properties and setting boundary conditions. This step is necessary to compute the solid mechanics and the magnetic response portion of the model. It is worth noting that the boundary conditions and the fixed constraints seen in Appendix B Figure (2) will change with respect to the loading conditions that will be presented in the results and conclusion.

To study the effects of magnetostriction on the solid mechanic portion and vice versa, a magnetostrictive relation was added to the circular Terfenol-D sensors, as seen in Appendix B Figure (3). In the case of the linear magnetostriction model, the material data can be entered in the stain-magnetization form using the elasticity matrix and the coupling matrix or in the stress-magnetization form using the compliance matrix and the coupling matrix [5]. The initial values node defines initial values for the displacement field and structural velocity field that can serve as an

initial condition for a transient simulation or as an initial guess for a nonlinear analysis (Appendix B Figure (4)) [5].

Before applying external loads to the MagCFRP model, internal compressive loads were applied to the top and bottom boundaries of the Terfenol-D sensor region to simulate residual stress from fabrication. To solve the solid mechanics portion of the model, it is mandatory that the modeled domain's surface be fixed to a constraint. Fixed constraint nodes add a condition that makes the geometric entity fixed (i.e., the displacements are zero in all directions). Rotational degrees of freedom (DOF) will also be zero (Appendix B Figure (5 and 6)).

To study the magnetostrictive effect of the now semi-ferroic composite material, an external magnetic field must be applied to the domain of the modeled geometry. This will allow for high magnetic flux regions to be located and measured. This also allows for the physics interface to solve Maxwell's equations, which are formulated using the magnetic vector potential. The main node is Ampere's Law, which adds the equation for the magnetic vector potential and provides an interface for defining the constitutive relations and their associated properties, such as the relative permeability (Appendix B Figures (7 and 8)) [5].

Since the circular modeled Terfenol-D sensors are the only magnetic material in the MagCFRP system, it is given the magnetostriction relationship as seen in Appendix B Figure (9 and 10). The magnetoelastic multiphysics coupling nodes pass the appropriate magnetization contribution from the magnetostrictive material node in the solid mechanics interface to the Ampere's Law magnetostrictive node in the magnetic fields interface. These nodes also pass the mechanical stress contribution due to the applied magnetic field back to the magnetostrictive solid mechanics nodes [5].

The proper meshing of the domain is key to an accurate FEA model. Using COMSOL's adaptive meshing capability allowed the mesh refining to be physics driven. The adaptive meshing allows the MagCFRP interphase to have a finer mesh resolution than the far-field domain. This physics-driven adaptive meshing can be visualized in Appendix B Figure (11). Stationary studies were performed on the modeled composite to reduce the complexity of the solution as well as save computation time and power. Stationary studies are used when field variables do not change over time, such as the fabrication of MagCFRP.

Chapter 3

Results

3.1 MagCFRP Sensor Deposition

Protocol for depositing Terfenol-D sensors in CFRP has spanned from simple hand deposition techniques to advanced sputtering PVD. This section will present and compare results from the deposition processes discussed in section 2.4.

3.1.1 Sprinkle Deposition

As mentioned earlier, the sprinkling deposition technique involves "sprinkling" a prescribed amount of Terfenol-D sensors between lamina plies. As seen in Figure (3.1), the sprinkling deposition process is effective in physically depositing Terfenol-D sensors in a composite. However, it does not allow a high level of homogeneity of sensor deposition. This sprinkling deposition technique is not ideal for future production applications, as the distribution of Terfenol-D sensors is non-homogeneous on a microscopic scale. This non-homogeneous distribution of Terfenol-D sensors can be depicted in Figure (3.1). As seen in Figure (3.1) circled in red, the sprinkling deposition technique forms conglomerates of Terfenol- D.

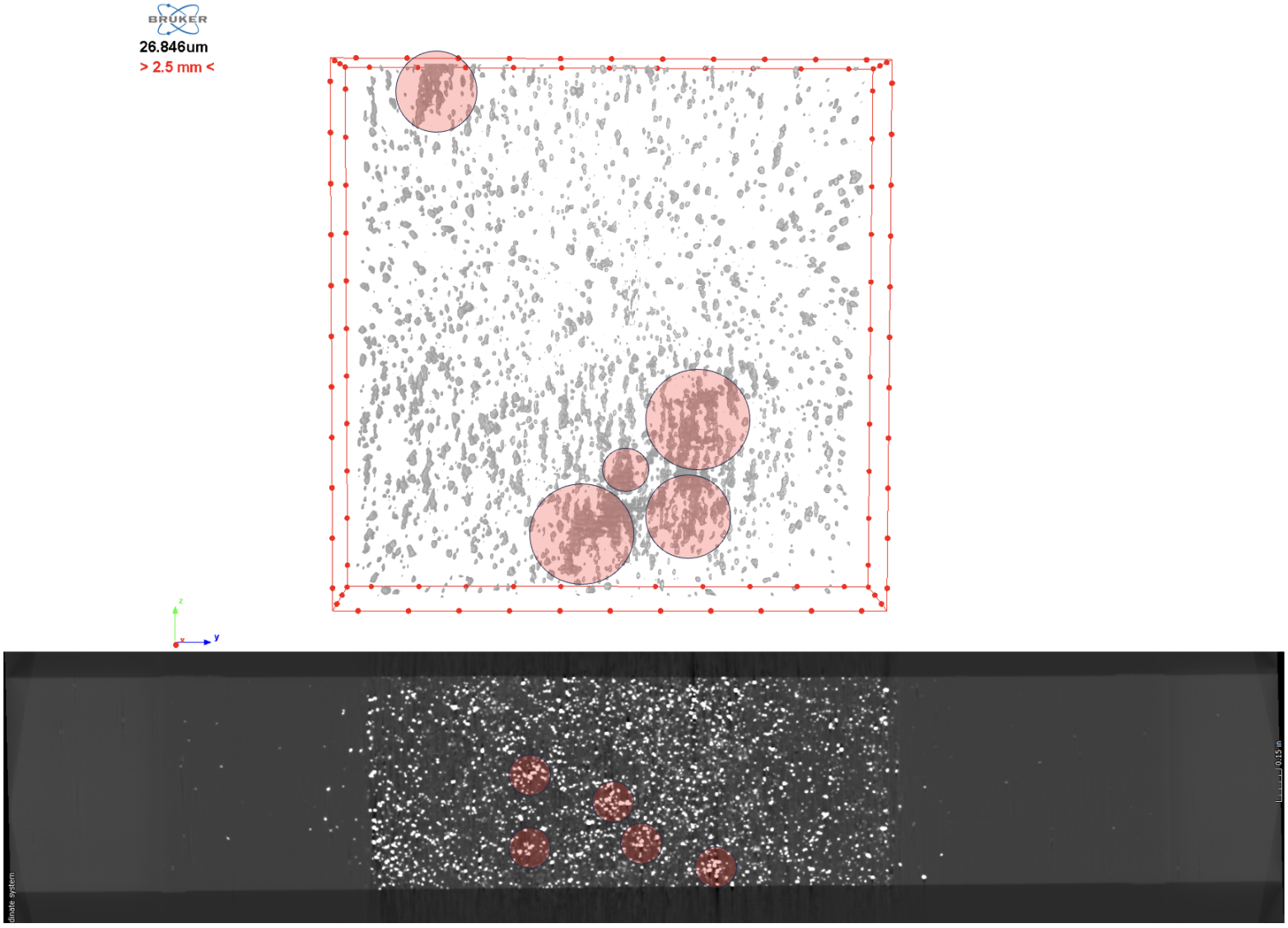

Figure 3.1: a. (top) Micro X-ray CT scan of MagCFRP using the sprinkling deposition technique (26.846-micron pixel resolution). b. (bottom) Full X-ray CT scan of MagCFRP using the sprinkling deposition technique.

3.1.2 Field Structured b-stage Deposition

As stated earlier in section 2.4.4, the objective for field structuring Terfenol-D sensors in b-stage epoxy coupons was to embed them between CFRP ply regions to create semi-MagCFRP structures. As seen in Figure (3.2), using Dr. Dereje Seifu's (Professor at Morgan State University, Department of Physics) Magneto-optic Kerr effect (MOKE) biaxial field magnet, fibrous sensor sheets were created and formed into embeddable Terfenol-D sensor coupons. As seen in Figure (3.2), structuring the Terfenol-D sensors in this manner gives the coupon an orthotropic material alignment in that the fibrous sensors are all oriented in one direction. Compared to the sprinkling deposition technique, Terfenol-D sensors from the magnetoelastomer field structuring technique have superior clarity and resolution on the macro and microscopic length scale.

This comparison between sprinkling and field structuring methods can be visualized in Figure (3.3). Figure (3.3) shows that the micro x-ray CT results show the difference in clarity and resolution of the embedded Terfenol-D sensors on the macroscopic scale. The X-ray CT scan in Figure (3.3a) was taken at a resolution three times higher than the Figure (3.3b) scan, and the difference in sensor distribution is evident. In Figure (3.3), the difference in sensor orientation and distribution density can be seen. The conglomerations seen in Figure (3.3b) are not present in the magnetoelastomer field structuring sample in Figure (3.3a).

The difference in deposition characteristics can be studied further on the microscopic scale. Figure (3.4) shows the microscopic snapshot of the Terfenol-D sensor formation post-MagCFRP consolidation. Figure (3.3a) was taken with a 1.78-micron pixel resolution of Terfenol-D sensors deposited using the sprinkling method. Figure (3.3b) was taken with a 0.71-micron pixel resolution of Terfenol-D sensors deposited using the magnetoelastomer field structuring method. By Figure (3.4), Terfenol-D sensor conglomeration is apparent in the sprinkling deposition method. In the magnetoelastomer field structuring snapshot, single-walled Terfenol-D sensors are oriented head to tail in the structured field direction. The sensor size in the magnetoelastomer field structuring snapshot also agrees with the manufactures specified sensor size between 38-106 microns. The sensor size in the sprinkling deposition snapshot is conglomerated in nature, meaning each sensor is a collection of multiple sensors forming a multi-walled Terfenol-D sensor. These more giant sensor formations are not ideal for interlaminar delamination density propagation applications, as these large sensors will impede ply-to-ply consolidation, which would diminish material properties

[25, 9, 10, 24, 6].

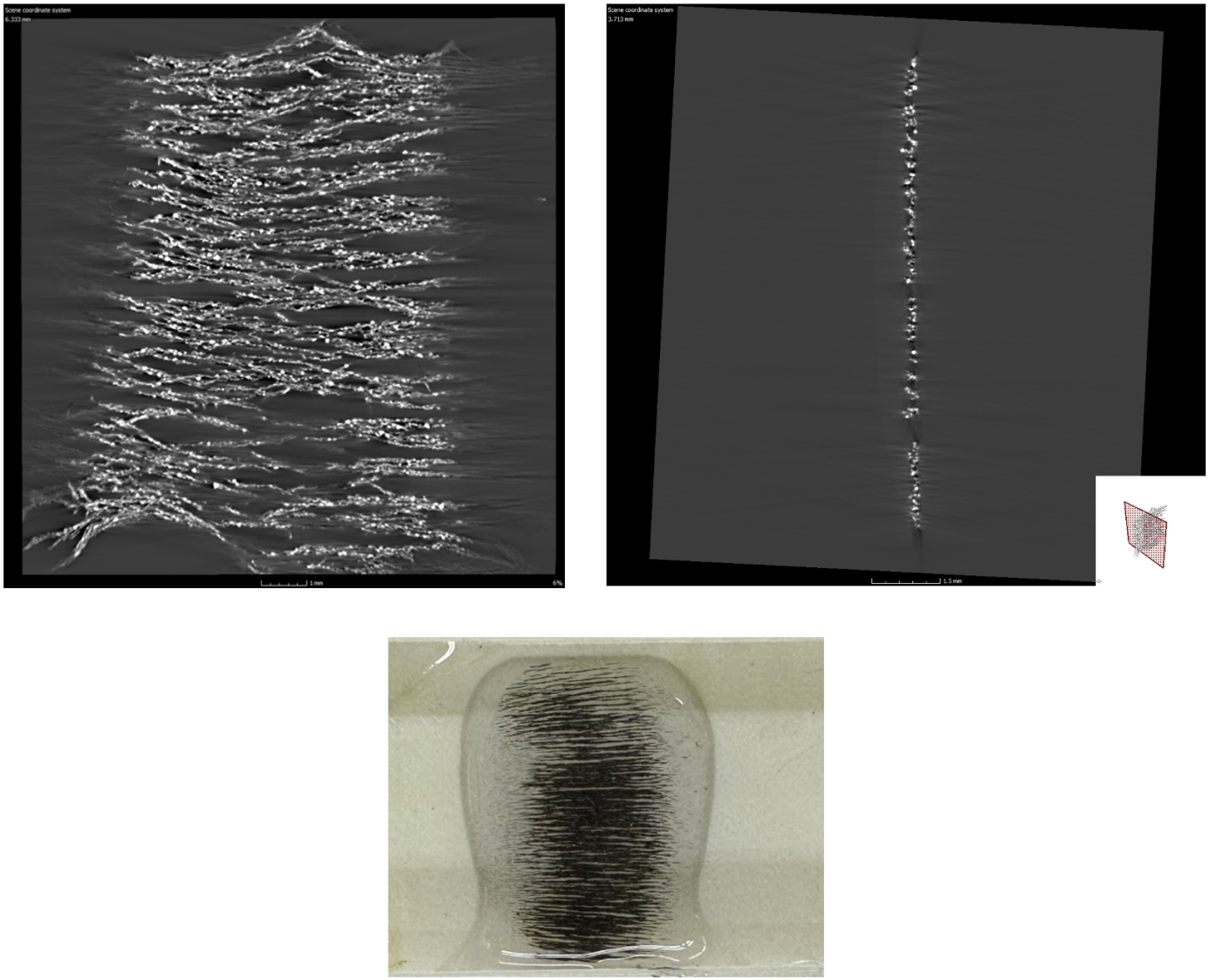

Figure 3.2: a. (top left) Micro X-ray CT scan of b-stage sheet field structured Terfenol-D magnetoelastomer coupon (0.71-micron pixel resolution). b. (top right) Cross-section view of b-stage sheet field structured Terfenol-D magnetoelastomer coupon (0.71-micron pixel resolution). c. (bottom) Sheet field structured Terfenol-D magnetoelastomer slurry coupon in a silicon mold.

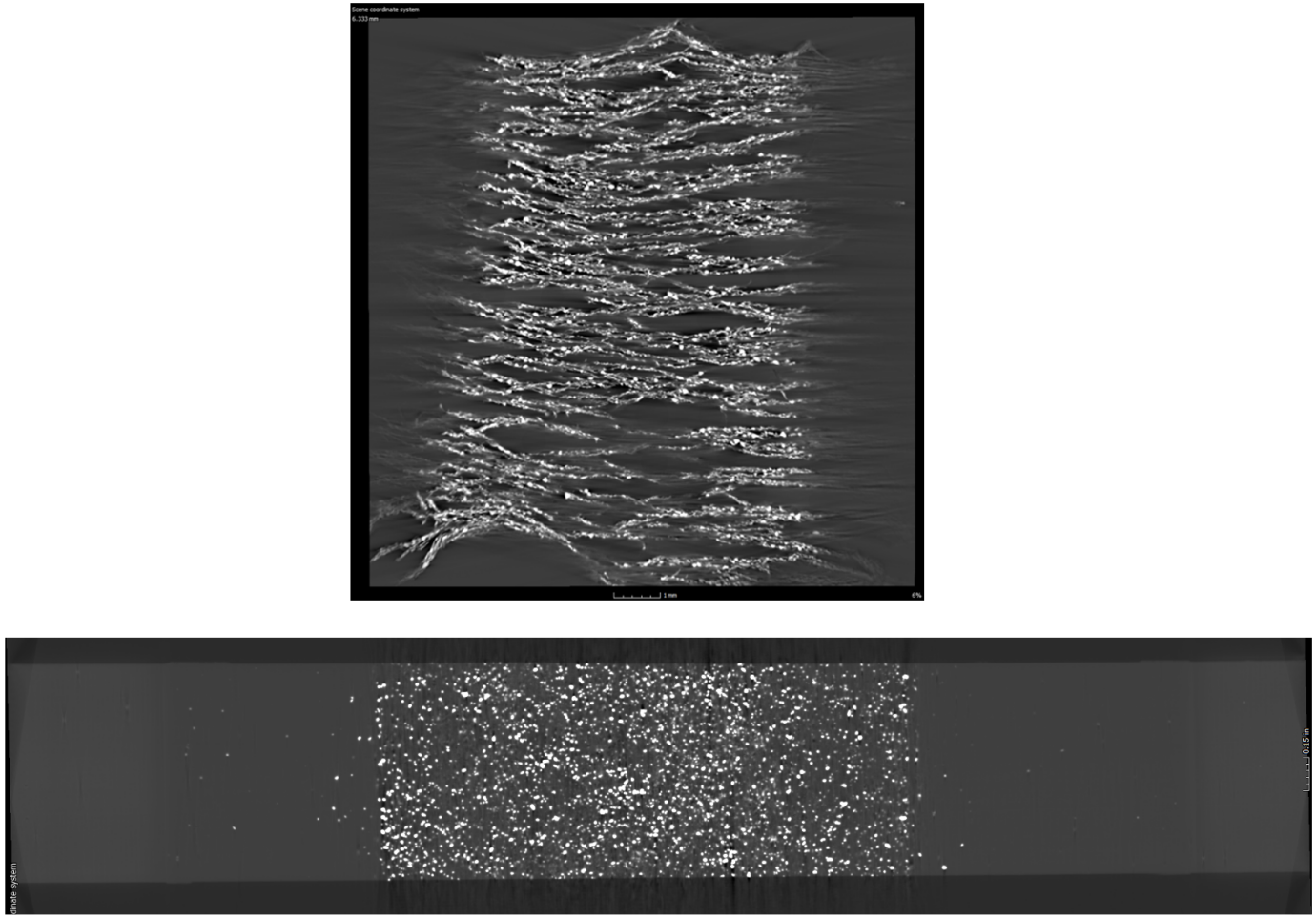

Figure 3.3: a. (top) Micro X-ray CT scan of b-stage sheet field structured Terfenol-D magnetoelastomer coupon (0.71-micron pixel resolution). b. (bottom) Full X-ray CT scan of MagCFRP using the sprinkling deposition technique.

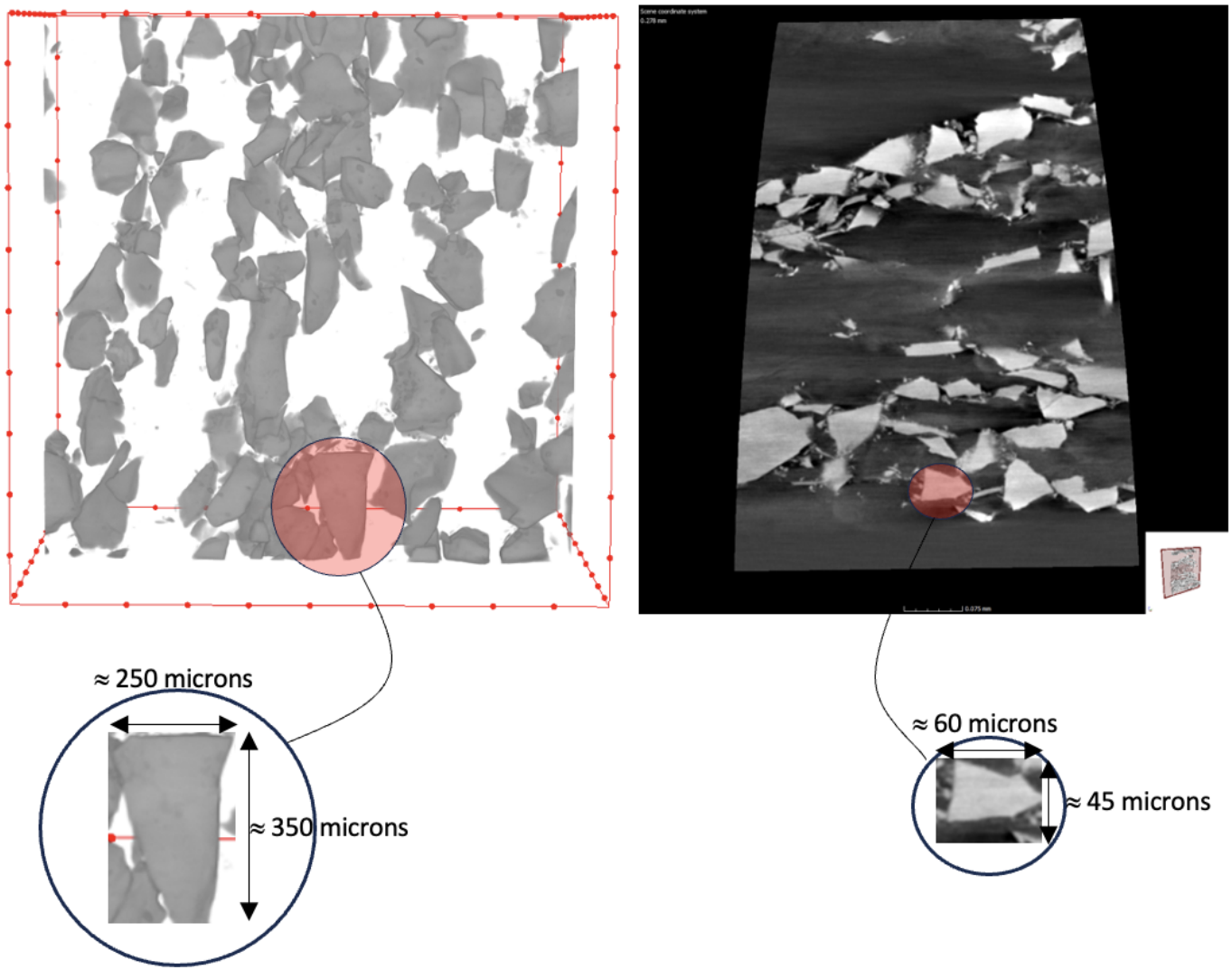

Figure 3.4: a. (left) Sprinkling deposition micro X-ray CT scan (1.78-micron pixel resolution) b. (right) Field structuring micro X-ray CT scan (0.71-micron pixel resolution).

3.1.3 Sputtering Deposition

This sputtering deposition research was done in collaboration with Dr. Dereje Seifu of Morgan State University. While the sputtering of Terfenol-D in this work for delamination density propagation is novel, the approach taken was a proof of concept rather than a practical approach. Due to limitations in deposition area and process environment location, it was not feasible to use CFRP as a substrate to sputter Terfenol-D film onto. Instead, Terfenol-D film was sputtered onto Onyx additive manufacturing material, as seen in Figure (3.5). Mechanical and magnetization response results from the 3D-printed Onyx material will be presented later in this chapter.

Upon insertion into the sputtering chamber, a circular clamp held the masked samples. The samples were masked so only the gauge area extrusion would be filled with Terfenol-D film. The substrates were heated to 80^oC for 30 min with 5 mTorr of argon to prepare the samples. The sputtering process cycled for 30 min at a sputtering power of 300 W using a 50.8 mm diameter Terfenol-D target. Deposition occurred at a pressure of $4 \cdot 10^{-3}$ Torr. Following the sputtering process, the Onyx substrate material was heat treated at 80^oC for 2 h in the chamber with a 5 mTorr argon chamber pressure. After the post-sputtering annealing process, the heating element was turned off, and the substrates cooled to approximately 35^oC before the pressure chamber was flushed and depressurized. At a deposition rate of 2 angstrom/sec, the Terfenol-D film's approximate thickness is 360 nanometers.

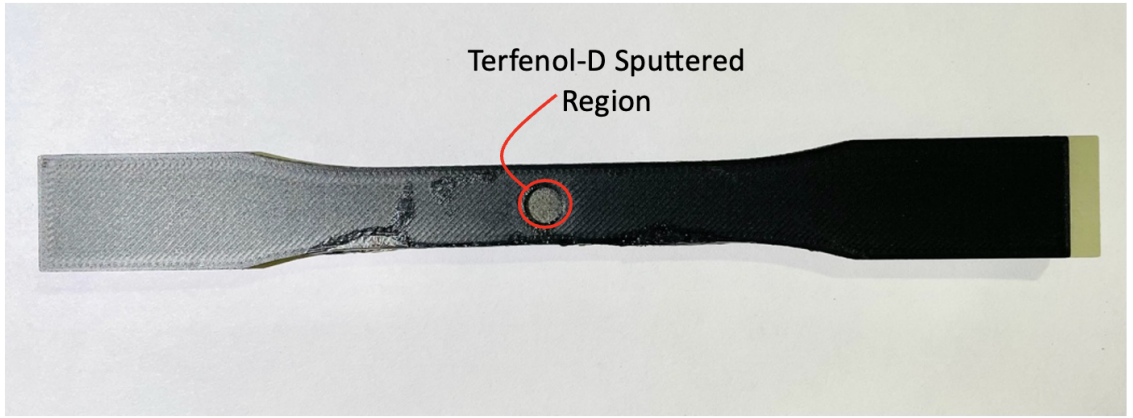

Figure 3.5: a. (top left) Dr. Dereje Seifu preparing the deposition vessel for sputtering. b. (top right) Onyx material masked with aluminum foil. c. (bottom) Onyx material with deposited Terfenol-D thin film.

3.2 Magnetostrictive Response

Throughout this work, the Terfenol-D particulate material embedded between MagCFRP lamina has been called "sensors." This sensor assessment is entirely accurate under the umbrella of magnetoelasticity in small displacement regimes in between composite lamina. As discussed throughout Chapter 2, Terfenol-D's magnetostrictive nature allows it to be used as a displacement sensor in interlaminar delamination density propagation in CFRPs. These sensors transmit relevant magneto-mechanical data via localized magnetic flux density, which enables it to be a completely wireless transmission system. In this section, the relative delamination density magnetostrictive results will be presented.

3.2.1 Voltage RMS Response

As discussed in section 2.5.1, it is possible to correlate the voltage generated in an AC magnetic field to magnetic flux density. The governing mechanics behind the principle of the driving-coil, pick-coil electromagnetization is discussed in greater detail in Haile et al. "Detection of damage precursors with embedded magnetostrictive particles."

Quasi-static tests were conducted on a 15 wt% MagCFRP specimen. This quasi-static test was on the scale of 0-70% of the MagCFRP's Ultimate Tensile Strength (UTS). The delamination validation technique used during this test was Acoustic Emission (AE) and Vibrating Sample Magnetometer (VSM). The raw voltage responses were processed using FFT algorithms. The baseline test of an identical composite material without Terfenol-D sensors did not exhibit any change in localized Voltage RMS during the 0-70% UTS loading interval. This can be seen in Figure (3.6), where the resonance frequency amplitude (i.e., voltage RMS, all waveforms are stacked on top of one another) or phase does not change throughout the loading interval.

Figure (3.7) shows 0-70% UTS quasi-static loading results from the 15 wt% MagCFRP specimen. As seen in Figure (3.7), the dominant voltage RMS variance exists between the "NO LOAD," "50% UTS", and "70 % UTS" curves. Because these results were produced by electromagnetic stimulation and the driving alternating magnetic field is much larger than the saturation magnetic field of Terfenol-D (i.e., $H_s << H_d$), it is challenging to physically interpret precisely what is happening during the amplitude and phase shifts seen in Figure (3.7). The physics and mechanics in Chapter 2 are based on non-transient magnetic fields but rather constant magnetic fields and magnetic flux

densities. Nonetheless, there was an observed change in voltage RMS concerning loading intervals.

A Vibrating Sample Magnetometer (VSM) is a scientific instrument used to measure the magnetic properties of materials. It is used in research and industry to characterize the magnetization behavior of various materials, including magnetic nanoparticles, thin films, bulk solids, and magnetic devices [4]. The basic principle of a VSM involves measuring the magnetic moment of a sample while subjecting it to an oscillating magnetic field. As discussed in section 2.1, changes in a magnetostrictive material's magnetization can be utilized to determine fundamental material properties and characteristics.

VSM measurements, performed by Dr. Dereje Seifu of Morgan State University, were taken of the 15 wt% MagCFRP specimen before and after mechanical testing. Figure (3.8) shows the observed magnetic moment change between the $45 - 135^o$ vibrating magnetometry angles before and after mechanical testing. As mentioned in Chapter 2, changes in a material's magnetization and permeability are directly related to the mechanical state of the ferroic material. Since the only ferroic material in MagCFRP are the Terfenol-D sensors, it can be deduced that the change in magnetization is associated with sensor reorientation within the matrix material.

AE results in Figure (3.9) show that as the load is increased during testing, so do the AE "hit" amplitude and event frequency increase (peak amplitude of 100dB). These AE results will be instrumental in concluding the mode and severity of interlaminar damage in future conclusion discussions.

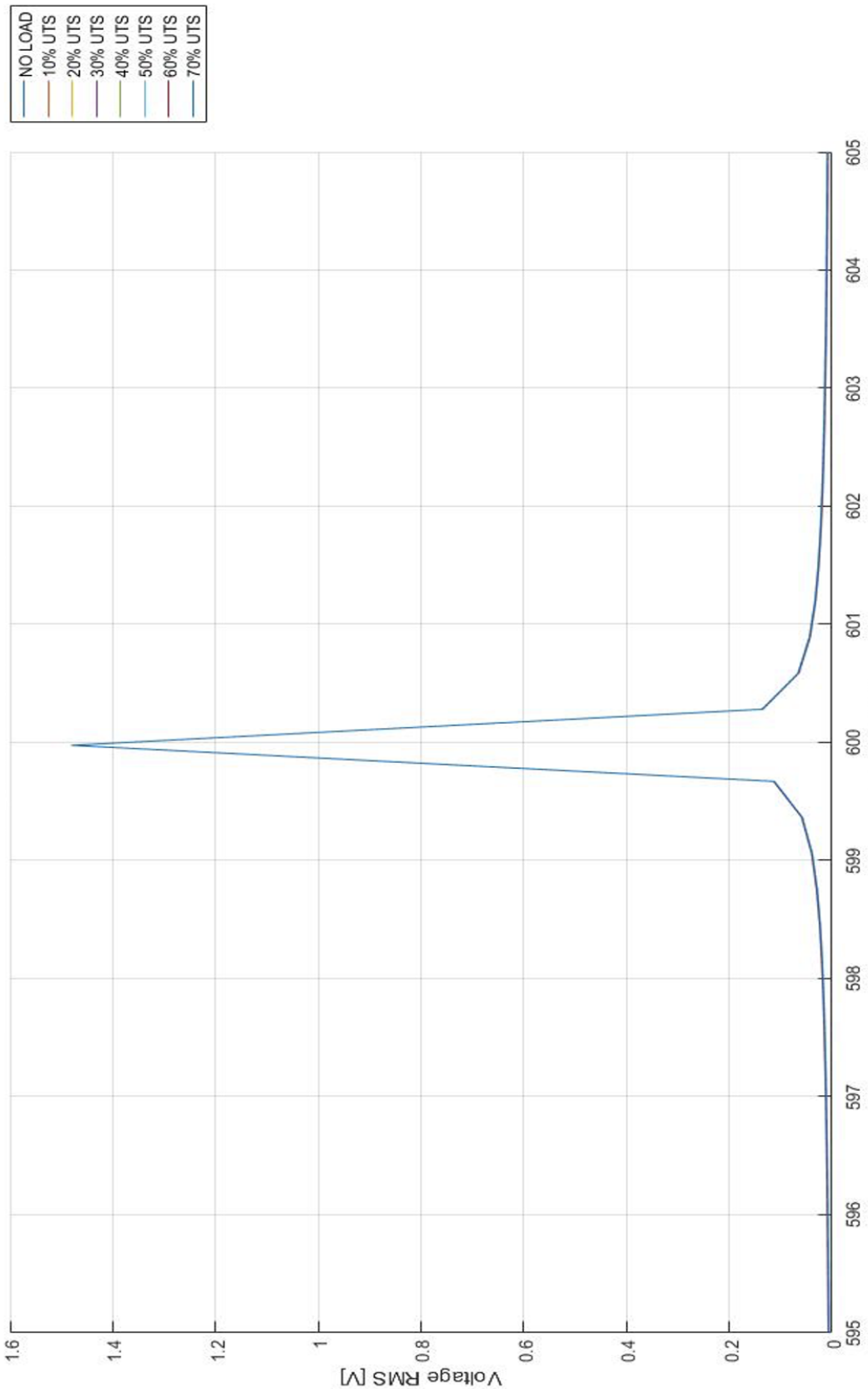

Figure 3.6: Baseline voltage RMS response

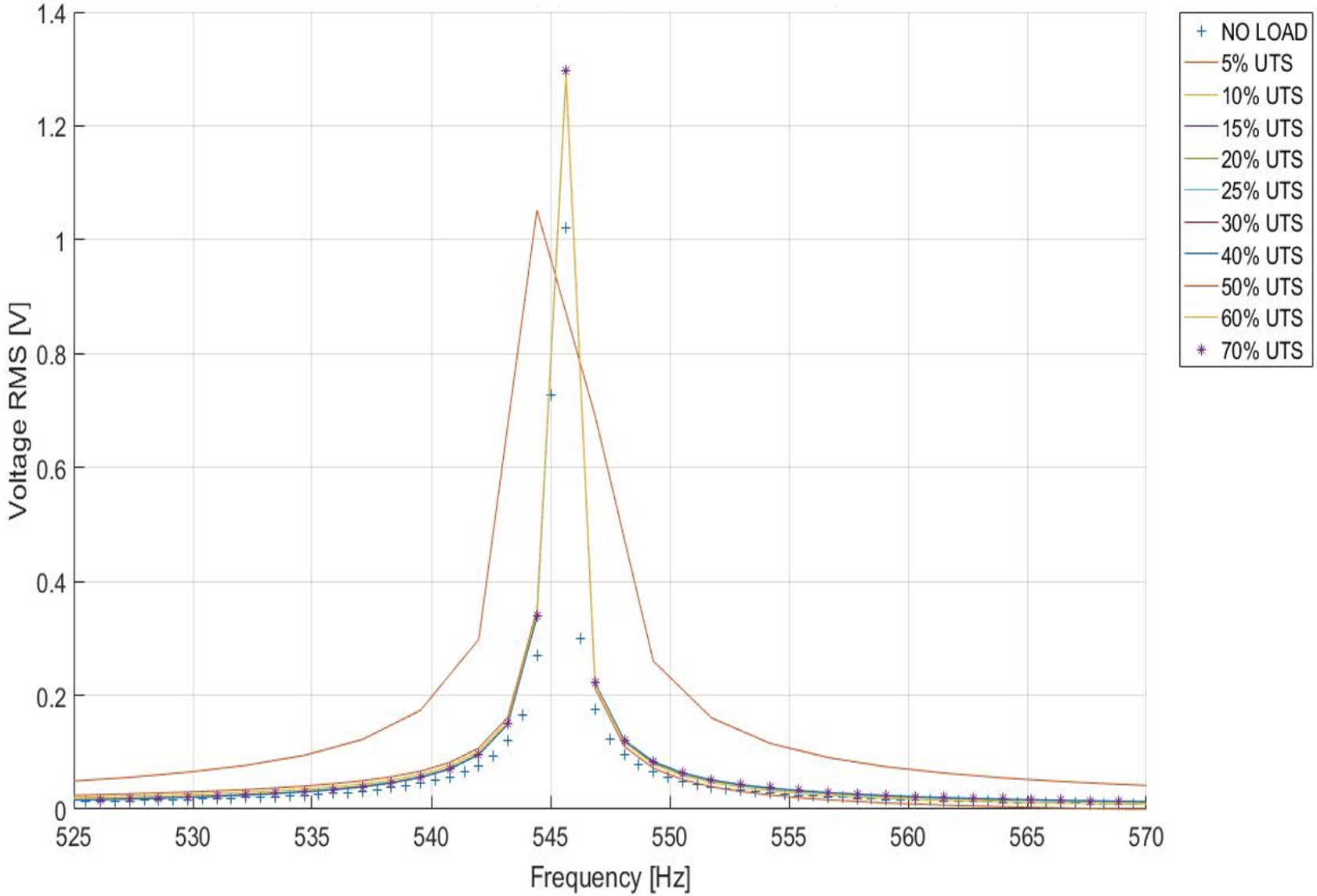

Figure 3.7: 15 wt% voltage RMS reponse

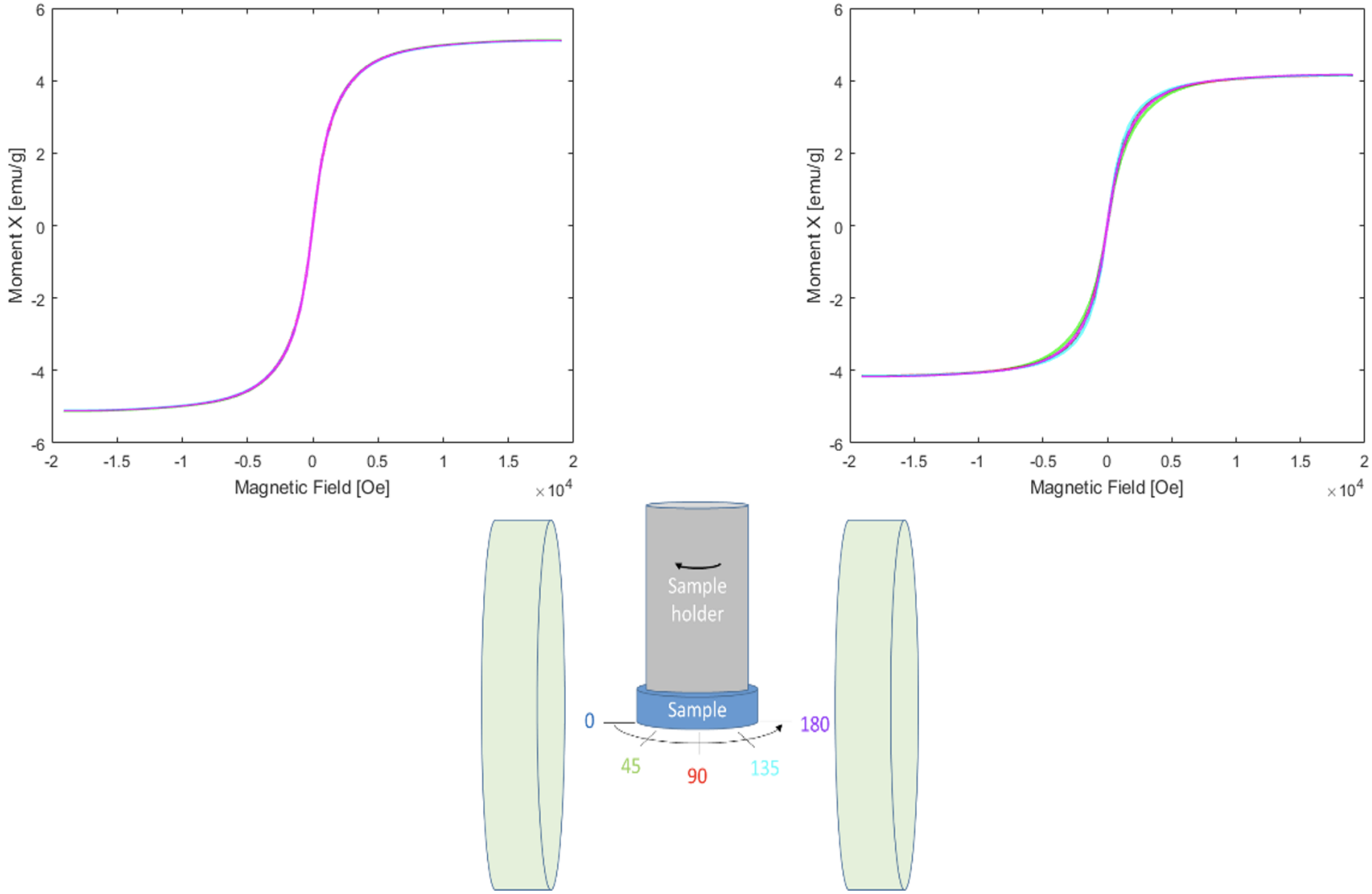

Figure 3.8: 15 wt% VSM response.

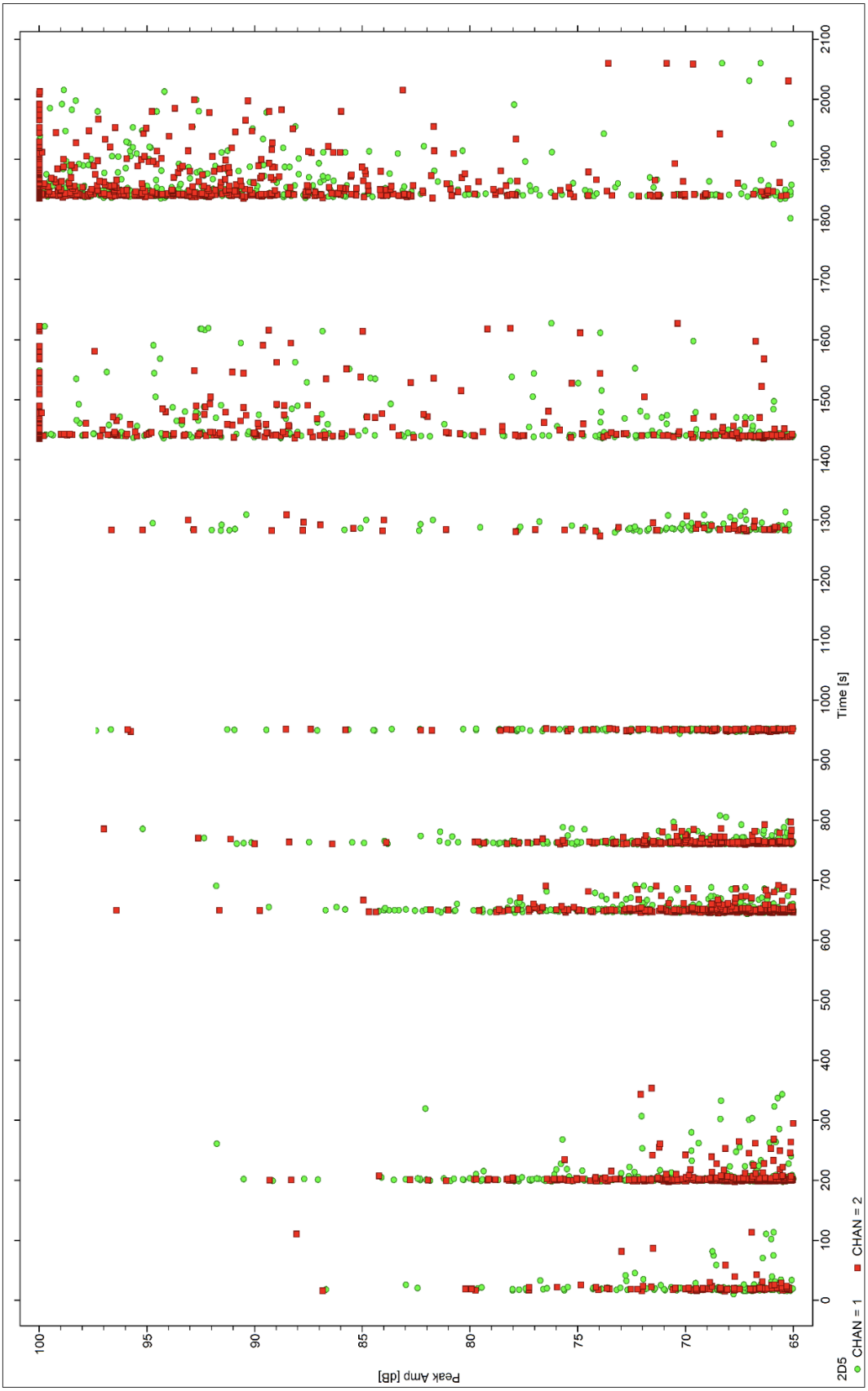

Figure 3.9: 15 wt% AE response for electromagnetic stimulation.

3.2.2 Thin Film Magnetostrictive Response

Terfenol-D thin film deposition can potentially be used for small strain damage progression analysis. By using PVD techniques like sputtering, it is possible to achieve atomistic level strain clarity and resolution for surface and sub-surface delamination density propagation. Five Onyx samples (three baselines and two Terfenol-D coated) were mechanically tested to study the change in localized magnetization for surface-sputtered Terfenol-D thin films, as seen in Figure (3.10).

The baseline results validated the non-ferroic interaction assumption for 3D printer Onyx tensile specimens not coated in Terfenol-D film. As seen in Figure (3.11), there is no change in localized magnetic flux density as the stress and strain in the material increase. Initial results for the Terfenol-D thin film samples agree well with the general mechanics of magnetoelasticity (Figure (3.12)). As the tensile stress increases, there should be a localized decrease in available magnetic flux density. The results show that there is an initial net decrease in magnetostrictive response by 14% in sample 1 and 8% in sample 2. This was expected because the magnetostriction coefficient from equation (2.3), d_{32}, is negative in tension and positive in compression. Progressing even further into the governing mechanics, the framework presented in Chapter 2 expresses that increases in Terfenol-D volume elements will reduce magnetostrictive response. This is driven by elasticity, in that elongation in any one principal direction does not result in equal shrinkage in the other two off-axis directions (i.e., $\nu_{2,3} < 0.5$).

As seen in Figure (3.12), the trend in reduced magnetization as stress increases does not continue and suddenly jumps up. This is due to the Terfenol-D film moving outside the scanning region as the load frame stretches the material. As mentioned in section 3.1.3, the Terfenol-D film was only deposited in the circular printed extrusion. Once this Terfenol-D film region is no longer in the scanning field, it does not respond. The out-of-field sensor region can be seen in Figure (3.13).

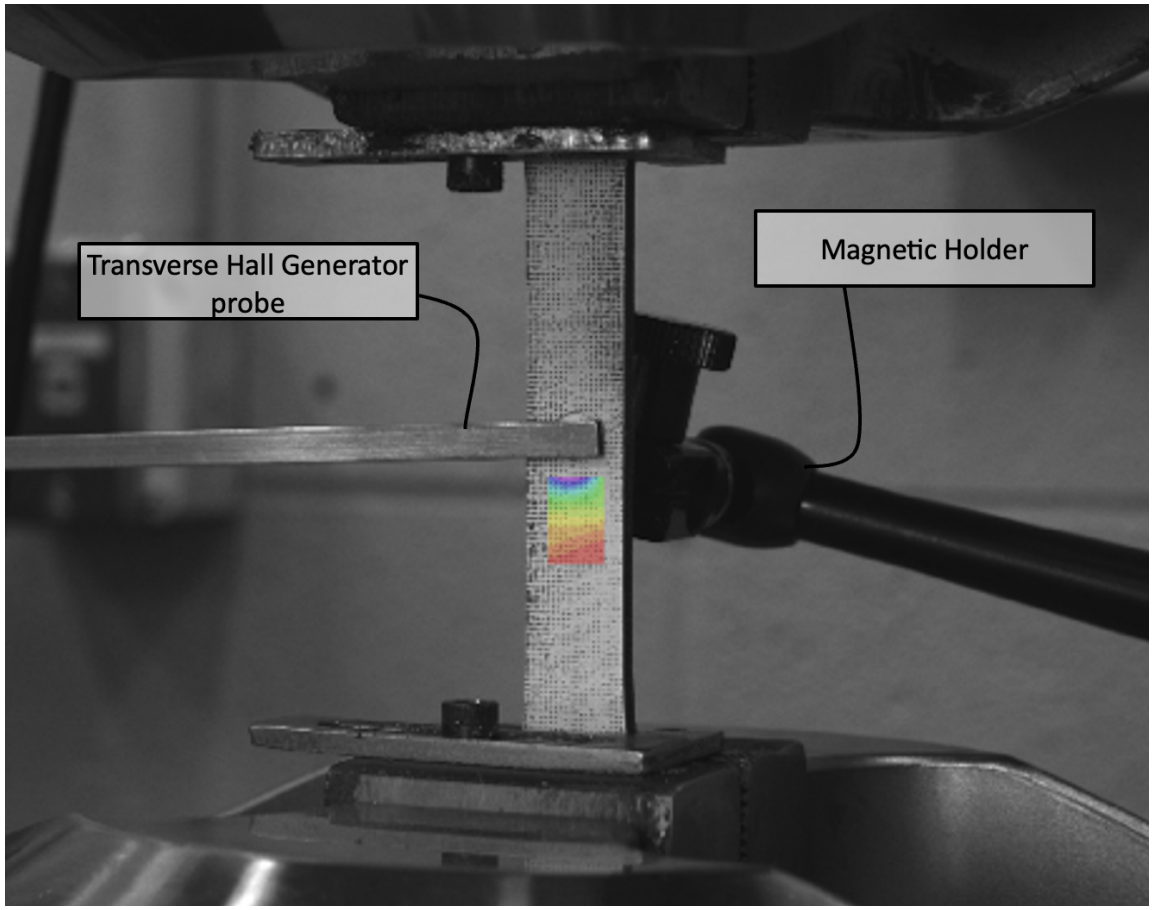

Figure 3.10: Sputtered Onyx test specimen.

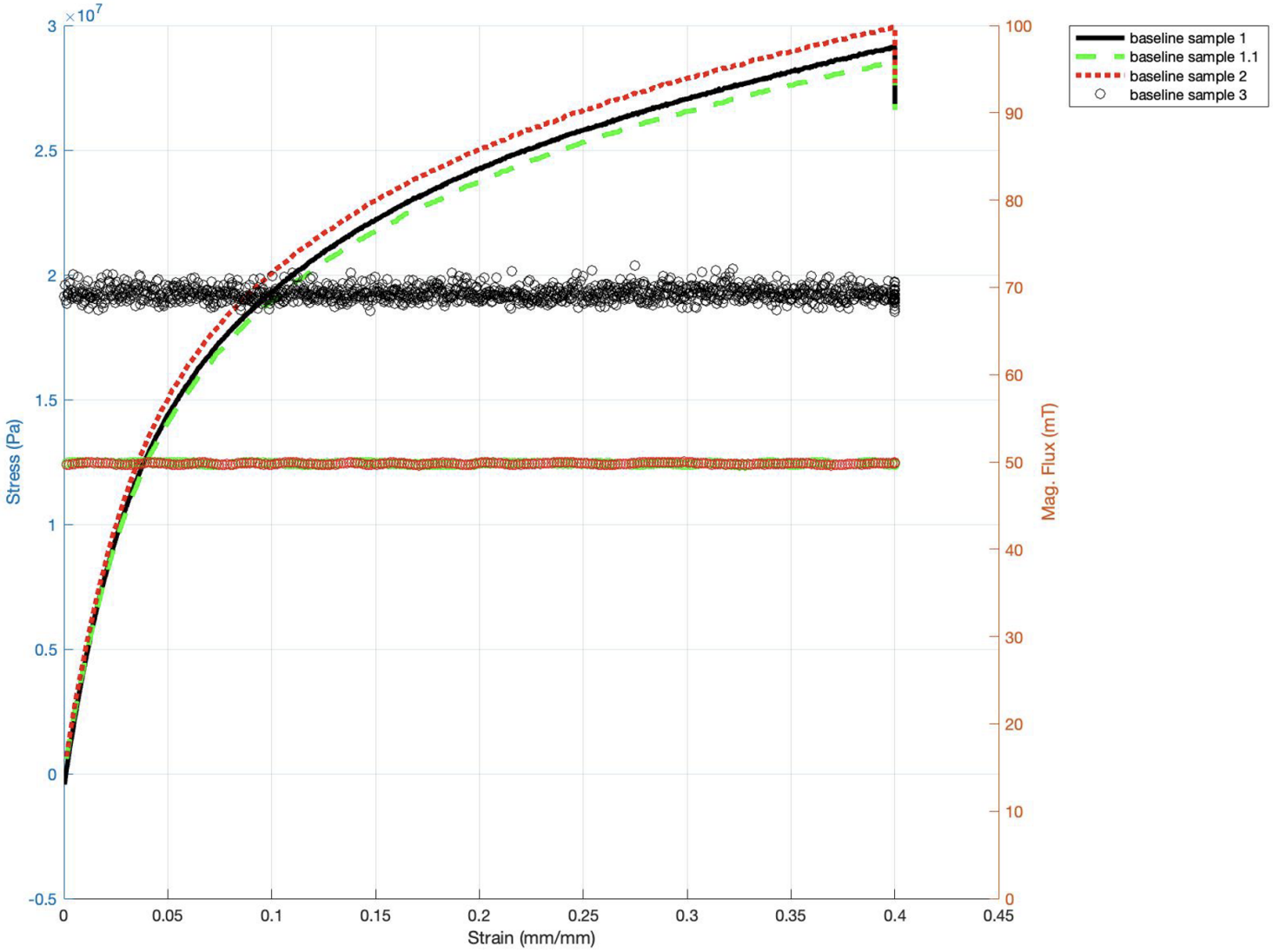

Figure 3.11: Onyx baseline results.

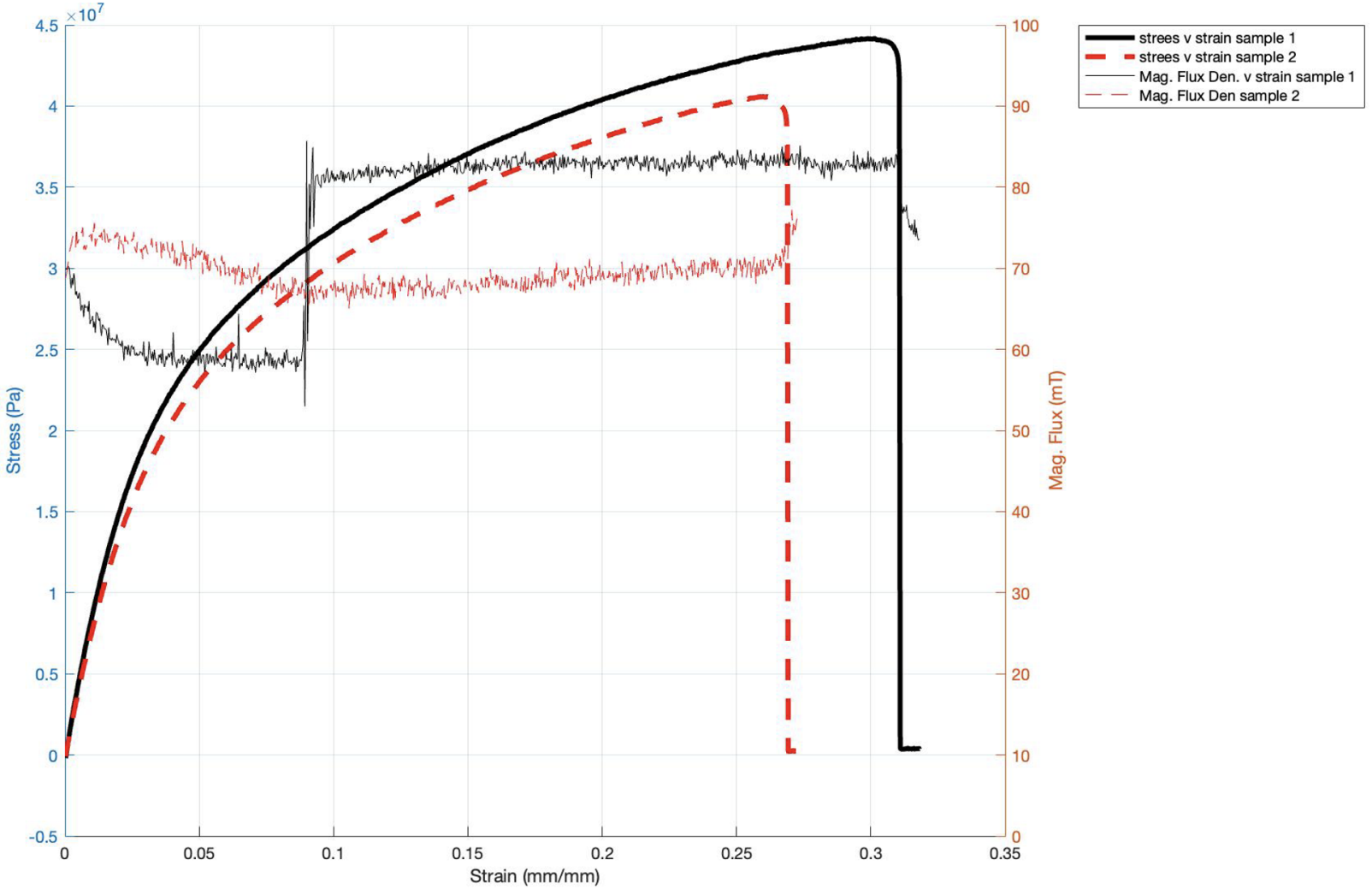

Figure 3.12: Onyx Terfenol-D thin film sensor response.

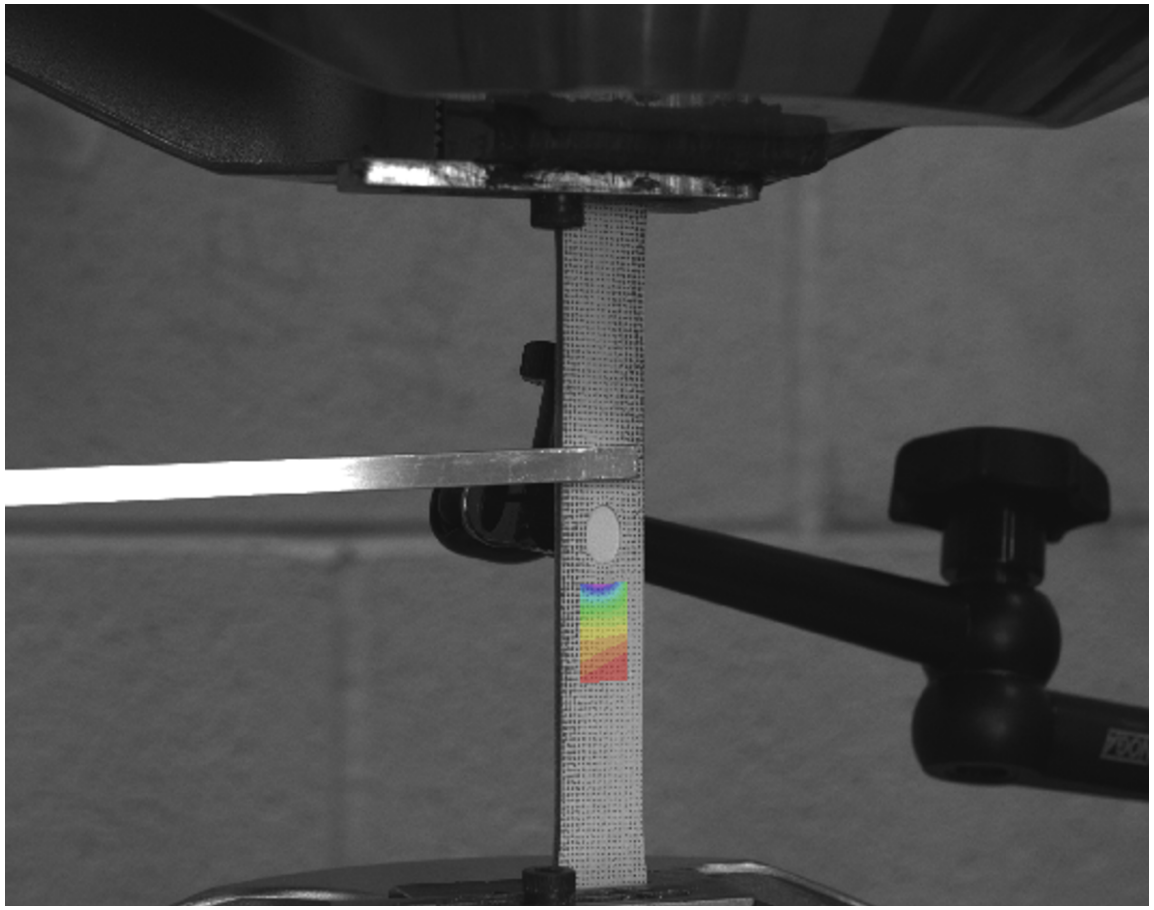

Figure 3.13: Onyx Terfenol-D thin film sensor out-of-field displacement

3.2.3 MagCFRP Magnetostrictive Response

The 15 wt% MagCFRP magnetostriction analysis was performed using the indirect magnetization method. Figure (3.14) illustrates normalized stress vs. localized magnetic flux density vs. strain graphs of each non-ferromagnetic baseline specimen. The stress axis was normalized with an average UTS of 1.6 GPa to make a direct correlation between failure stress and magnetic flux density values. This allowed for relationships to be studied regardless of the composite stacking sequence. The vivacious diagonal lines illustrate the stress vs. strain curves of the baseline CFRP samples. These linear stress/strain curves are associated with the left y-axis (Normalized Stress), and the horizontally oriented lines are associated with the right y-axis (Localized Magnetic Flux Density).

The magnetic flux density data in Figure (3.14) (the horizontally oriented colored lines matching their respective loading profile) illustrates a uniform driving flux density produced by the permanent magnet. As expected, there was no observed magnetoelastic response from the baseline samples that were not embedded with Terfenol-D sensors, as the CFRP is a non-ferroic material. This non-ferroic interaction can be visualized in the strictly horizontal magnetic flux density lines in Figure (3.14). As the load increases on each specimen, there is no change in magnetic flux density. The difference in the driving magnetic flux density values can be attributed to the change in the distance between the magnet and the Hall generator probe for each unique tested sample. The first-order magnetometer uncertainty was ± 0.0178 mT. This uncertainty is not a measure of variance between the unique driving magnetic flux density curves but a measure of variance in the magnetometer. All baseline and MagCFRP samples were taken to failure during mechanical testing.

When comparing two unique materials, it is essential to compare the difference in the strength of the materials. Specific to the MagCFRP system, it is necessary to understand how changes in deposition technique change the strength of the material when compared to baseline material strength data. Figure (3.15) illustrates the linear regression of the stress vs. strain data for the baseline and 15 wt% Terfenol-D embedded MagCFRP samples. Like the baseline samples, the 15 wt% Terfenol-D embedded MagCFRP also had an average UTS of 1.6 GPa. Although the average UTS of the baseline and 15wt% samples were the same, mechanical analysis of the stress vs. strain data showed a 4% reduction in strength and a 6% reduction in toughness between the baseline and 15 wt% samples. The baseline samples also have a higher modulus of elasticity (approx. 102 GPa) when compared to the MagCFRP samples (approx. 100 GPa), as seen in Figure (3.15). Terfenol-

D's magneto-mechanical coupling properties have the potential to increase interphase shear strength and shear modulus within the fiber-matrix-particle interphase bonding (Cole, 2017; Haile, 2015, Zhu, 2012, pp. 1316–1331). With improvements in deposition and fabrication, it is hypothesized that the Terfenol-D sensor deposition will increase the shear modulus and overall strength of the MagCFRP material. More research basic research must be conducted to prove this hypothesis.

A load-controlled test was performed on a 15wt% MagCFRP specimen to study the localized magnetic response. The load-step increments were 5% UTS up until 40% UTS. This load-step method was taken to break the magnetostriction response into moderate and severe damage sectors. Previous AE results from section 3.2.1 show that the onset of severe damage AE event amplitude is between the 40-50 % UTS loading intervals. The load-step hold intervals were manually controlled concerning the AE activity. When the AE "events" ceased, the load profile was increased by 5% UTS. Once 40% UTS was achieved, the load was stepped back down in 5% increments until material stress of 0% UTS was achieved. All the AE, load, and magnetization data were recorded via a data acquisition computer (DAC) at a sampling rate of 1000 Hz for uniform test step acquisition.

Figure (3.16) illustrates the relationship between the localized ($32mm^2$ FOV)) magnetic flux density responses (left y-axis) and normalized stress (right y-axis normalized by averaged failure stress) concerning time (index). The inertia effects were neglected since the testing procedures are not dynamic. Thus, this system's independent time component was converted to an index component, observing that all parametric data were sampled at the same frequency and time step.

As seen in Figure (3.16), an inverse relationship exists between the applied load and localized magnetic flux density, which is expected due to the aforementioned principles of magnetoelasticity. There was an observed jump in the localized magnetic flux density at the 30% UTS load increment (associated with the left y-axis). With damage precursors in mind, this sudden increase in magnetic flux density response could signify a severe Terfenol-D sensor reorientation. The hypothesis is that the sudden increase in load caused sudden sensor reorientation, which could be directly correlated to micro-cracking in the matrix material. This failure is likely explained by the Terfenol-D sensors' high conglomerate population, as seen in Figure (3.4). Since the Terfenol-D is embedded in the matrix material, the microcracking causes a release in stress/strain surrounding the sensors. This release in stress would cause an increase in localized magnetic flux density due to the aforementioned principles of magnetoelasticity.

After the 30% UTS loading increment, the inverse relationship between the localized mag-

netic flux density and load follows its trend. Figure (3.17) shows that 100% reversible localized magnetic flux density is achieved with a maximum load of only 40% UTS. Hamann and Shanmugham [32, 10] suggest that irreversible changes in flux and strains indicate permanent damage. Since the maximum load was only 40% of the UTS (moderate damage regime), it was expected to achieve complete reversible flux.

For the severe damage response mechanical testing, the load-step increments were 5% UTS until 70% UTS was achieved. The step intervals were manually controlled concerning the AE activity. When the AE "events" ceased, the load profile was increased by 5% UTS. Once 70% UTS was achieved, the load step was backed down to 0% UTS. As seen in Figure (3.18), the inverse relationship between applied loads and localized magnetic flux density still exists. However, the 100% localized reversible magnetic flux density was not achieved (reversible magnetic flux density of only 25%).

With interphacial degradation in mind, there was an observed drop-off in the return rate of reversible flux after 70% UTS loading. This response n magnetization signifies permanent damage at the sensor-matrix interphase and the fiber-matrix interphase. Observing equation (2.3), this reduction in out-of-plane magnetic response is sustained by the variance of the magnetostrictive coefficient d_{32} (depicted in Figure(s) 15 and 16 by the change in magnetic flux density concerning stress, i.e., σ_{yy}) and/or the change in permeability μ_{23}. Changes in a material's permeability are a well-accepted indicator of permanent damage [11, 17]. At this stress level, delamination fields and microcracking are present in the matrix material. Since the Terfenol-D is embedded in the material's matrix, it can concur that the irreversible degradation of localized magnetic flux density is associated with severe localized damage in the matrix material. This conclusion is validated with the corresponding AE data. Figure (3.19) is an explicit representation of the drop-off in residual magnetic density before and after 0-70% UTS testing. Results from Figure (3.19) are derived from localized magnetic flux scans taken before and after testing in the exact same gauge area. As seen in Figure (3.19), there is a $1.218mT$ decrease in residual magnetic flux density before and after testing (uncertainty of $\pm 0.0178mT$).

When AE is coupled with the magnetostriction sensor, there is a positive correlation between the AE event intensities and the diminished magnetostriction response. As depicted in Figures (3.20) and (3.21), the green points represent AE sensor 1, and the red points represent AE sensor 2. These AE sensors in this application capture acoustic wave events and their respective peak intensity in decibels (dB). The sensor-specific AE peak amplitude and localized magnetic flux density associated

with each load step are captured in Figures (3.20) and (3.21).

The localized magnetic flux density data (left y-axis) plotted in Figure (3.20) was formed by averaging the magnetic response for each loading interval (x-axis) and merging the AE data (right y-axis) on those same loading intervals. As seen in Figure (3.20), the exact inverse relationship between localized magnetic flux density and normalized stress is illustrated in Figure (3.16). For the 0-40% UTS loading interval (flux path under loading, depicted by pink line), as the stress increases, the localized magnetic flux decreases. For the 40-0% UTS loading interval (flux path load released, depicted by the black line), the localized magnetic flux increases as the stress decreases. In equation (2.3), the gradient of this localized flux vs. normalized stress plots experimentally gives you a solution for the elastic magnetostriction coefficient d_{32}, which was experimentally extracted by linear regression to be -11 nm/A. This magnetostriction coefficient can be determined using a more sophisticated least-squares model and used in numerical solutions to yield a more accurate result.

Revisiting the damage precursor discussion, the AE data in Figure (3.20) shows that at the 30% UTS load interval, there was an observed peak amplitude of 85 dB. At this dB level, mode II shear/ply delamination failure is initiated [1]. Although this type of defect is not what the Army would consider a precursor, it is still significant that MagCFRP locally responds to this type of damage initiation.

For the severe damage loading interval on 0-70% UTS, the localized magnetic flux density decreases as the stress increases. However, the rate of return of the localized magnetic flux density concerning the stress was significantly diminished. For the max load interval of 0-70% UTS, the peak AE amplitude observed was more than 100 dB, as seen in Figure (3.21).

At this dB level, mode I and mode II fiber-matrix debonding, cracking, and shear delamination failure have been initiated and propagated [1, 3]. The irreversible localized magnetic flux density is attributed to the specimen's high onset of interphacial damage. This severe level of composite damage is not what the Army would consider a damage precursor, as other traditional NDE methods could detect these defects.

However, because MagCFRP is an embedded sensing smart material, delamination density propagation at this level could be tracked wirelessly throughout the structure or component's geometry continuously. Other NDE methods, such as AE and strain gauge sensors, require wired connectivity and are only valuable for limited displacement field regions. AE specifically is subjected to the attenuating properties of CFRP in that events can only be detected within proximity of the

AE sensor [3, 1]. Acknowledging that AE is a well-known and well-accepted NDE technique is essential in solidifying the capability of MagCFRP to be a valuable NDE solution for future high-stress Army CFRP aerospace structures and components.

X-Ray CT was used as a post-processing technique to capture images of actual damage and compare them to recorded magnetostriction data. Due to highly intense beam hardening artifacts, little micro–X-Ray CT information was captured about the embedded Terfenol-D sensors' damage. However, areas away from the conglomeration of sensors validated the severe onset of damage after a 70% UTS loading interval (fiber breakage, surface ply delamination/cracking), as seen in Figure (3.22).

Figure (3.23) illustrates a micro–X-Ray CT post-processing technique called nominal actual comparison. Nominal actual comparison takes two images of a specimen before and after testing and measures the deformation. As seen in Figure (3.23), the observed deformation of the Terfenol-D sensor conglomerates occurred predominantly at the particle-matrix interphase and did not exceed $100\mu m$. Both compression and extension deformation were observed in X-Ray CT nominal comparison images. This observed interphacial deformation further supports how MagCFRP could be a viable solution for real-time localized composite interphase NDE.

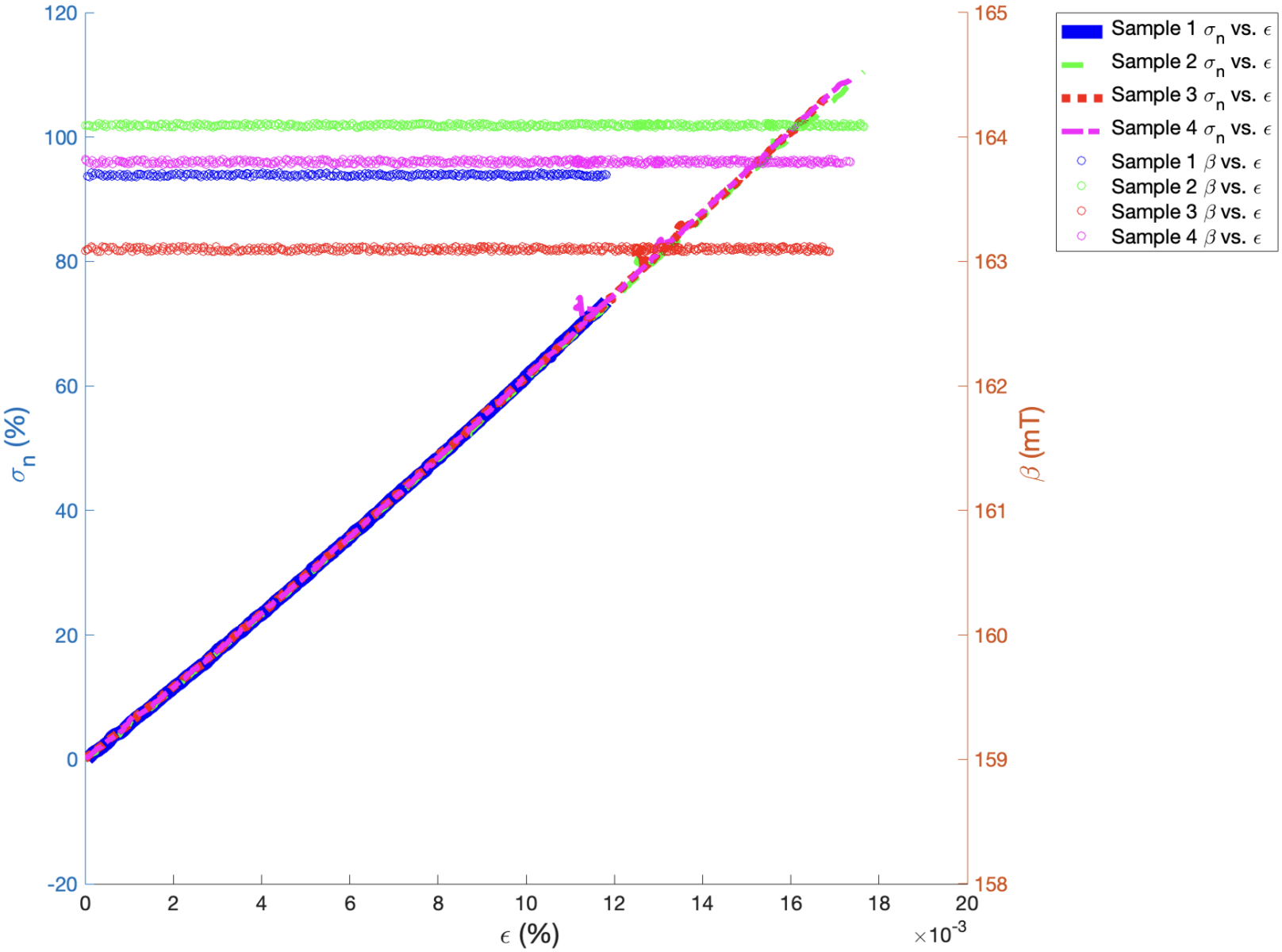

Figure 3.14: MagCFRP baseline results.

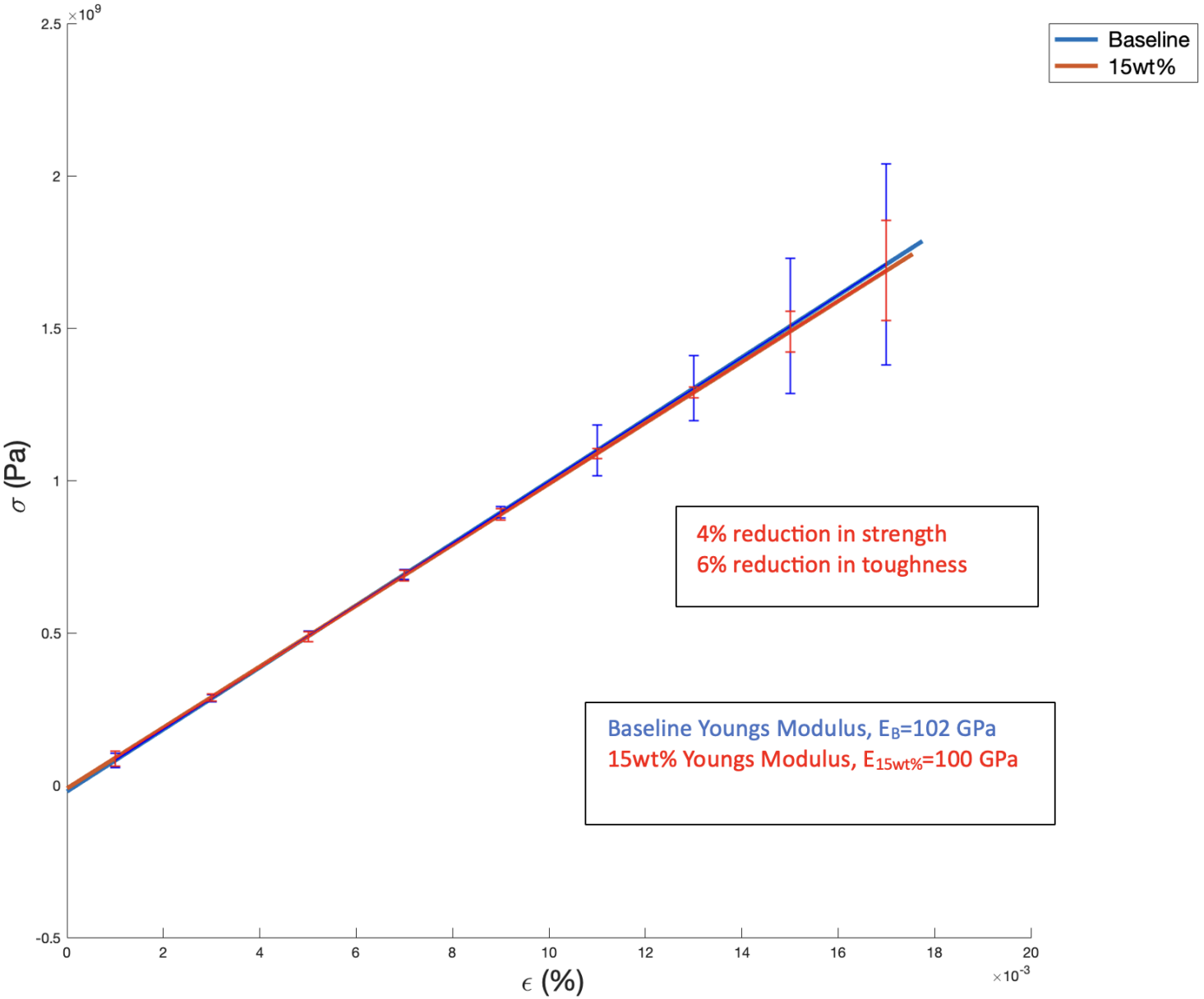

Figure 3.15: 15 wt% MagCFRP and CFRP baseline mechanical comparison.

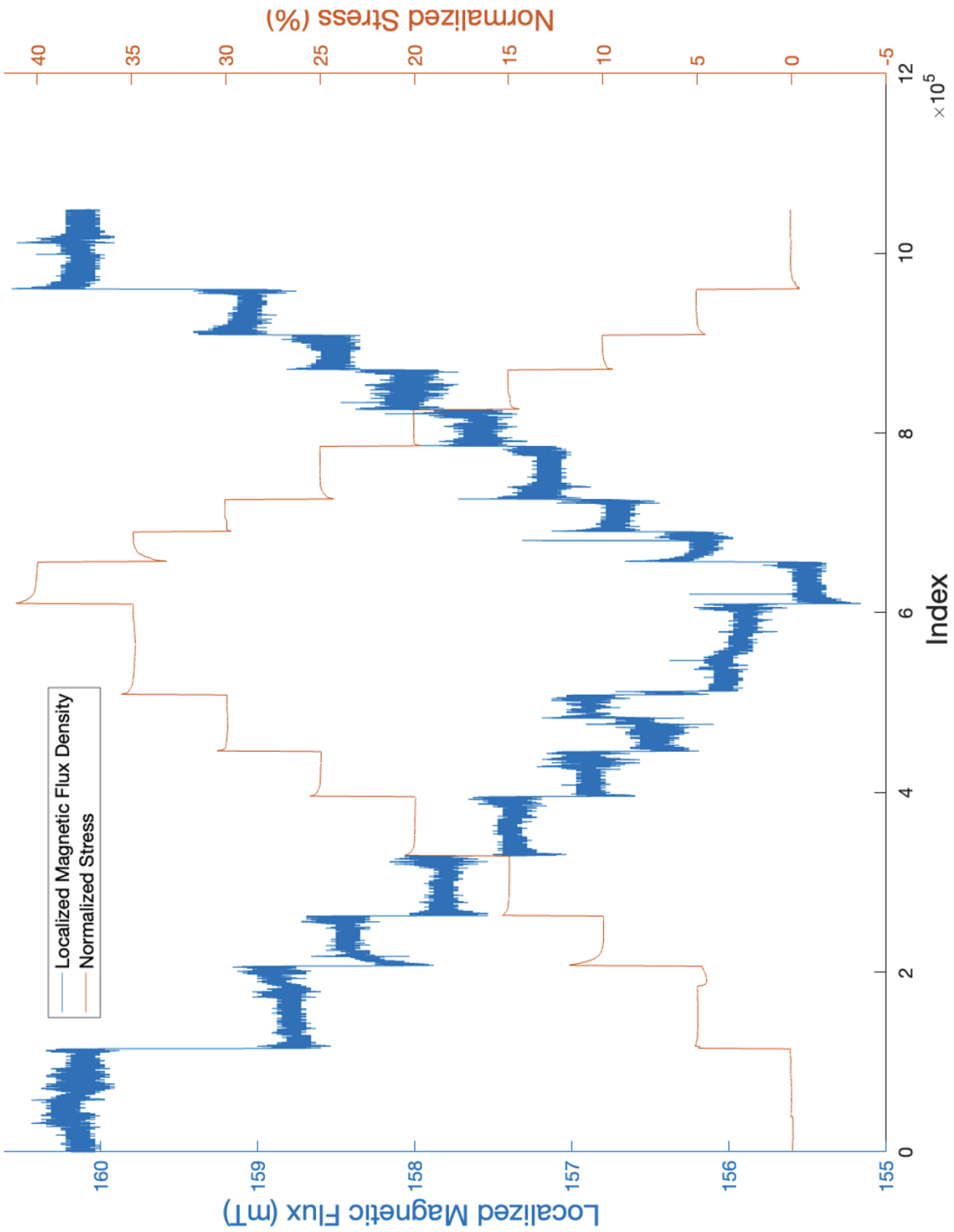

Figure 3.16: MagCFRP 0-40 % UTS response.

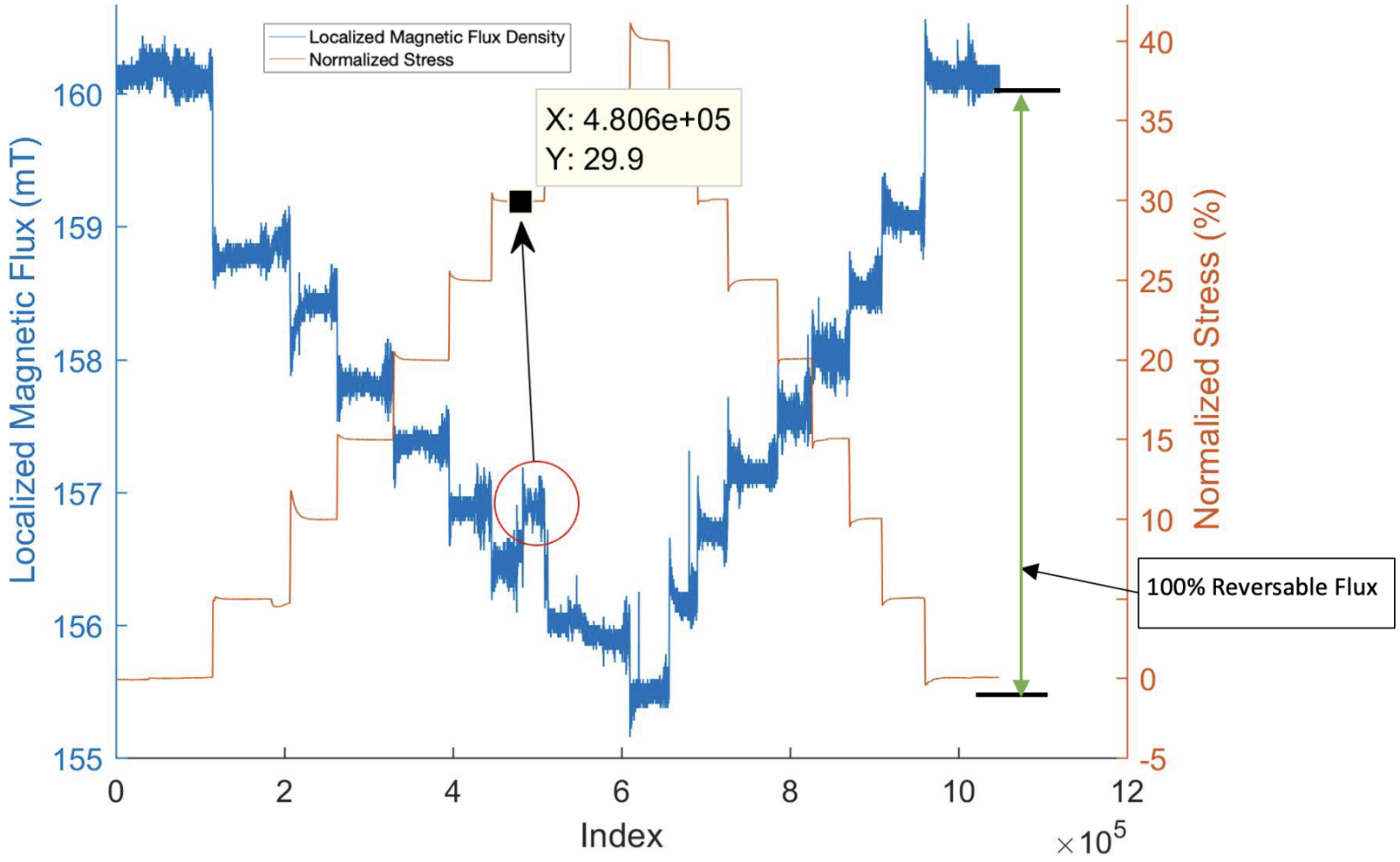

Figure 3.17: MagCFRP 0-40 % UTS response with reversible flux density.

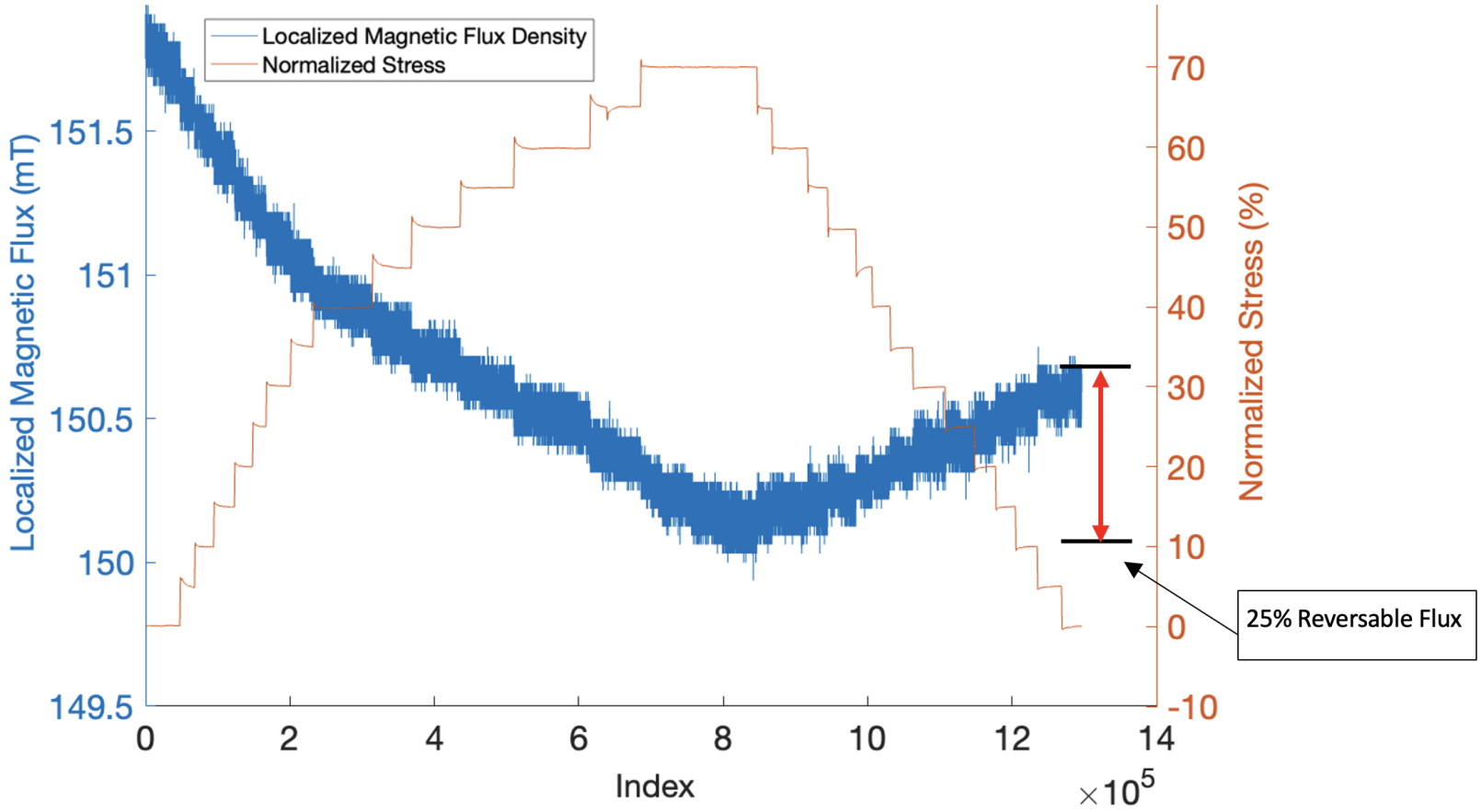

Figure 3.18: MagCFRP 0-70 % UTS response.

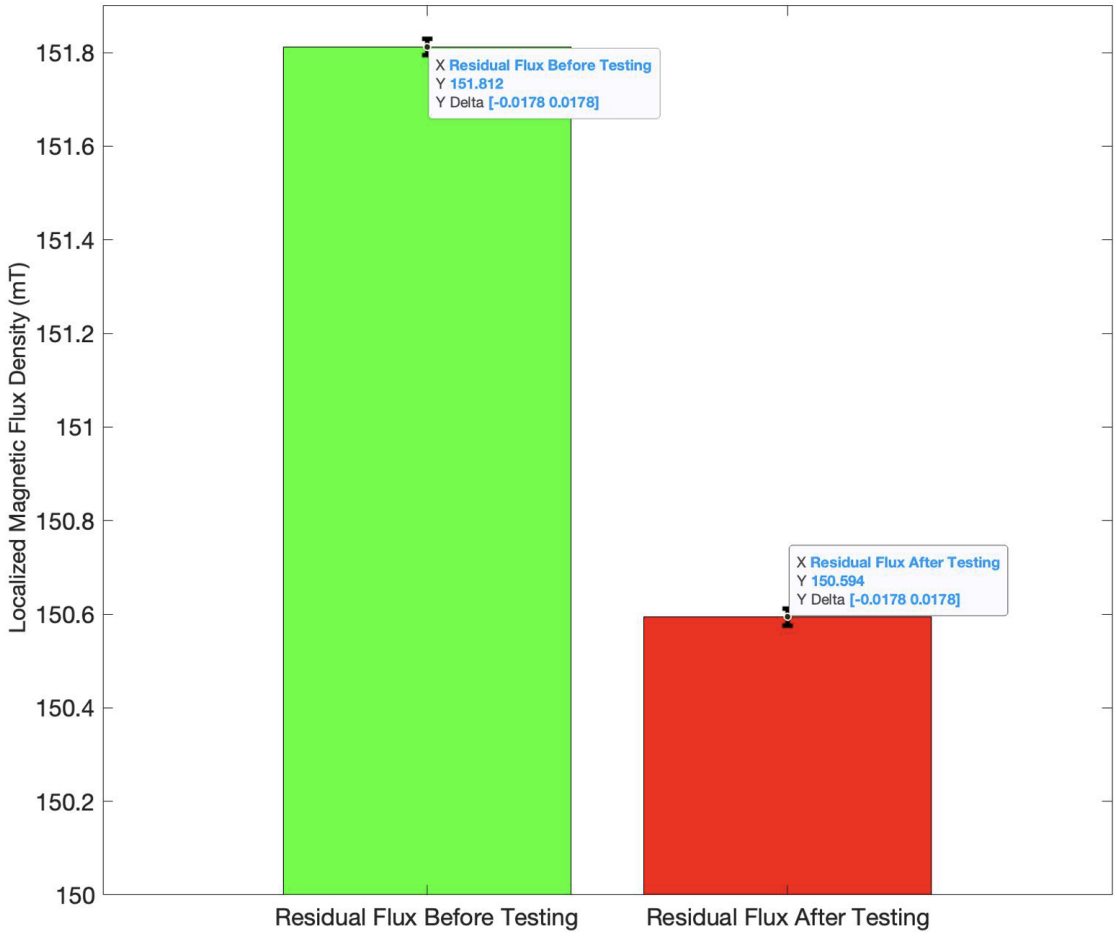

Figure 3.19: MagCFRP 0-70 % UTS residual magnetic flux density response.

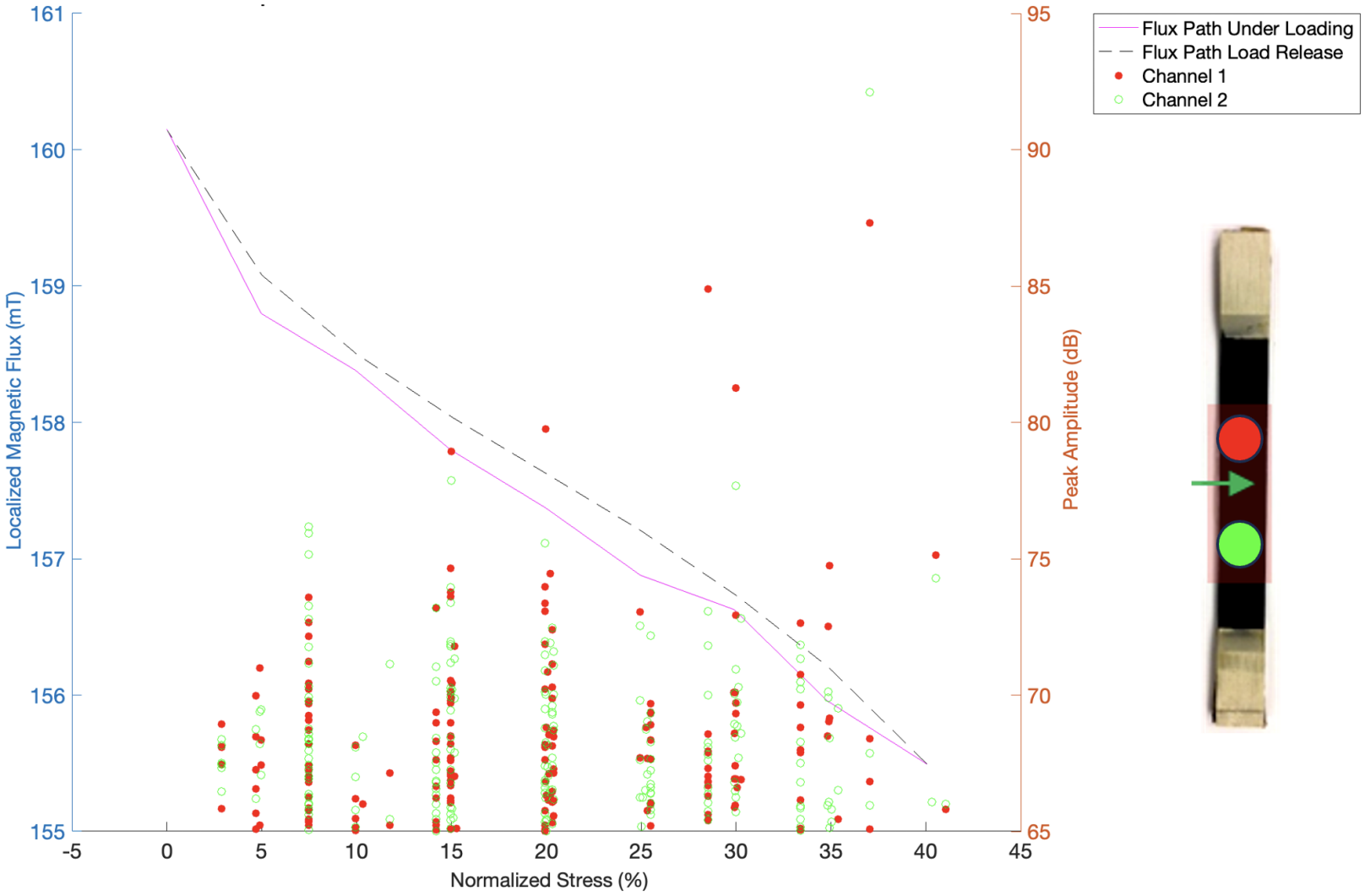

Figure 3.20: MagCFRP 0-40 % UTS AE and magnetostrictive response.

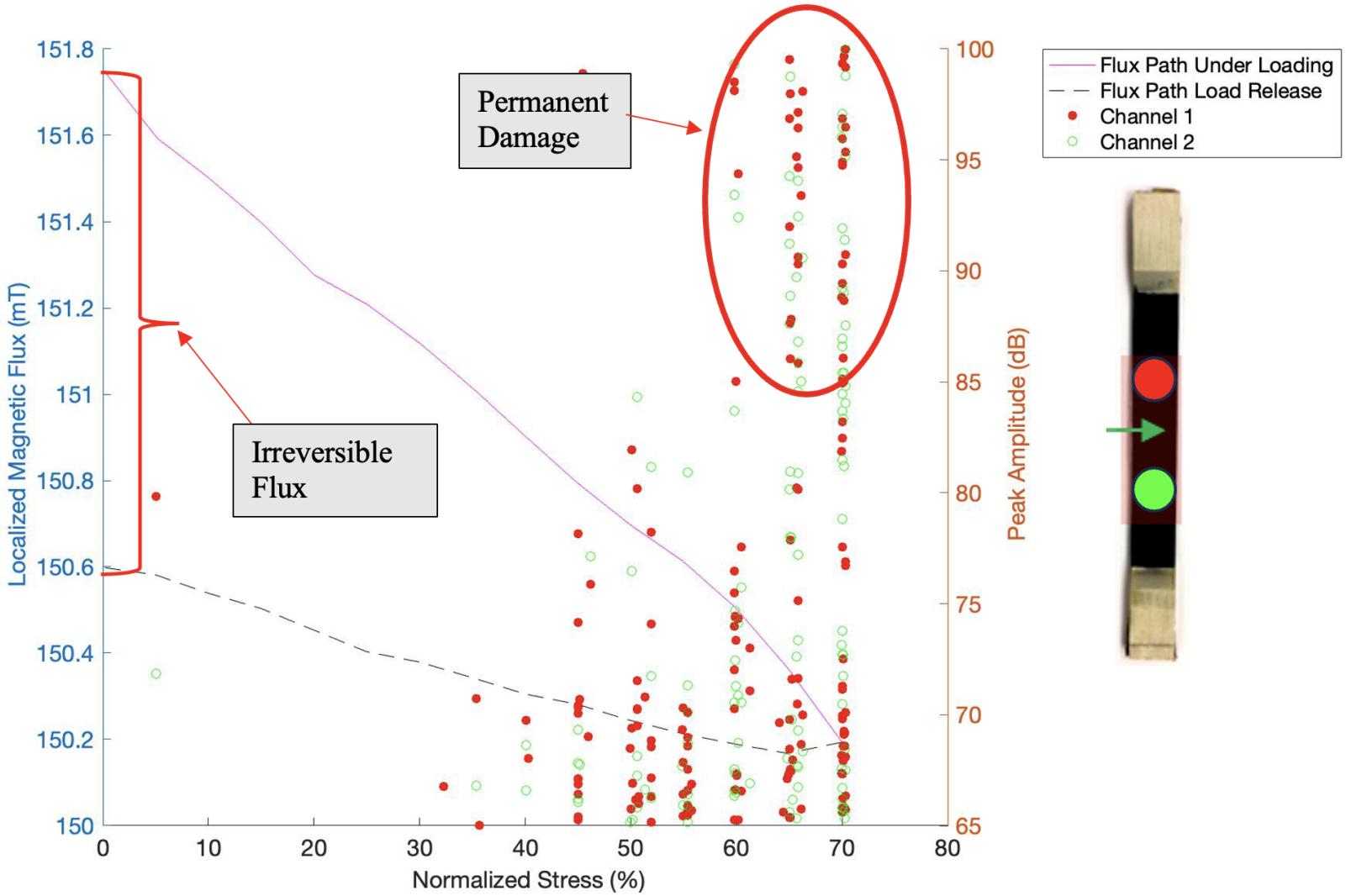

Figure 3.21: MagCFRP 0-40 % UTS AE and magnetostrictive response.

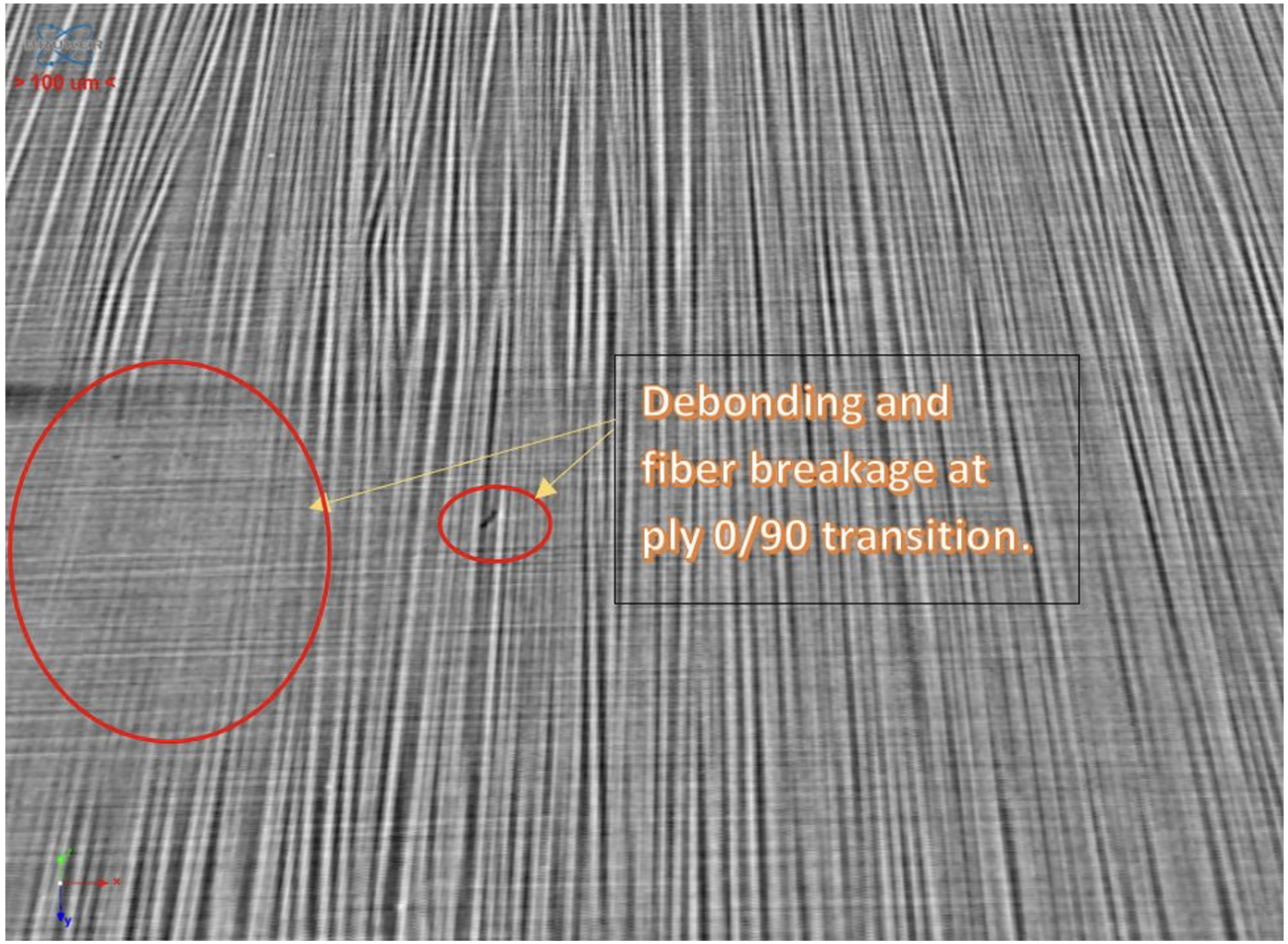

Figure 3.22: Micro X-ray CT damage verification for 15 wt% MagCFRP.

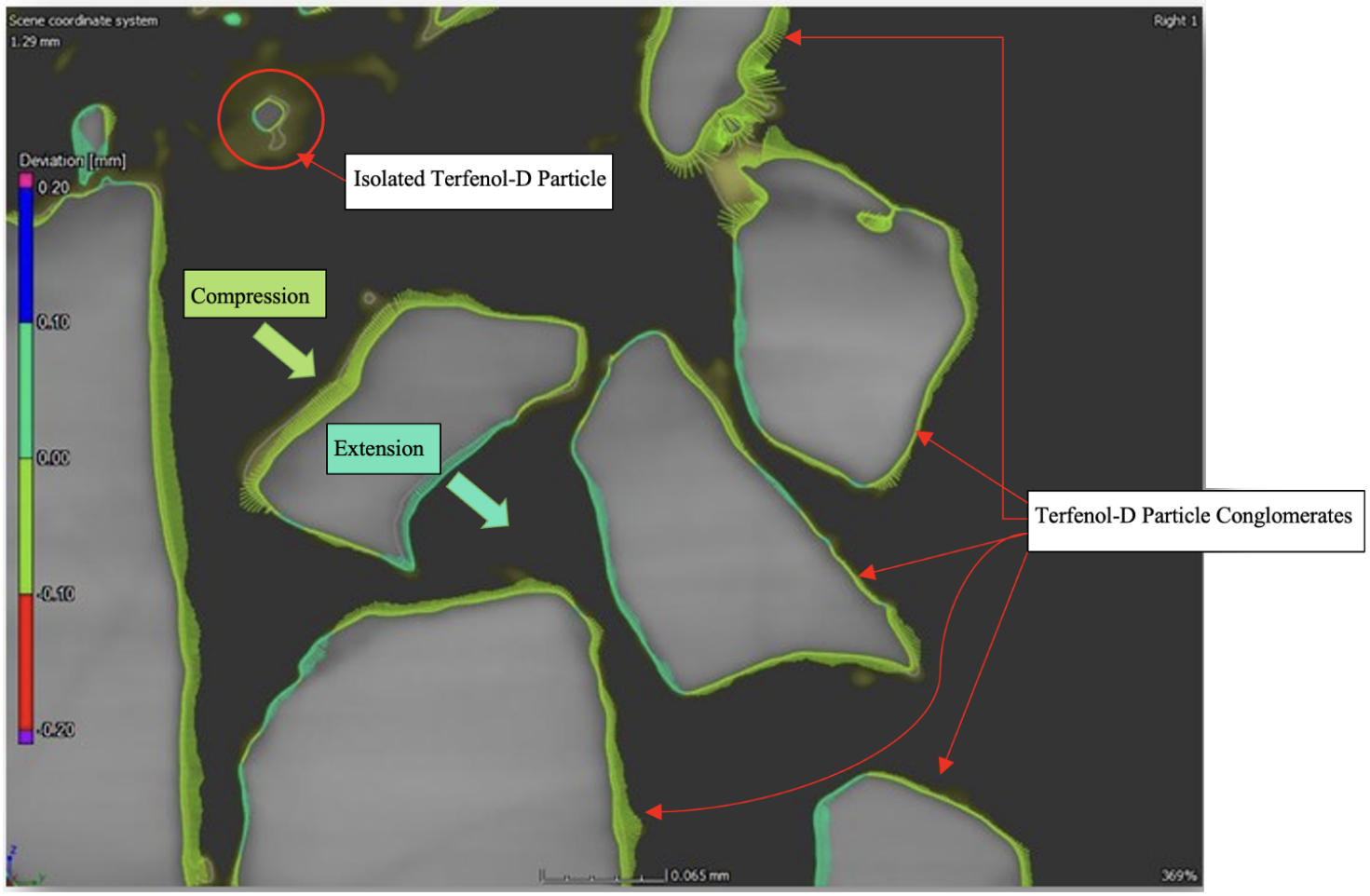

Figure 3.23: Nominal actual comparison results for 15 wt% MagCFRP.

3.3 FEA for MagCFRP

COMSOL FEA simulations deployed a normal constant saturation magnetic flux density over the domain to simulate the direct magnetization method numerically. As seen in Figure (3.24), COMSOL FEA results for MagCFRP fabrication stress analysis show a maximum general magnetic flux density for embedded Terfenol-D sensors to be $2.5mT \pm 0.5mT$ over a reduced sensor area from fabrication stresses and ply constraints. Figure (3.24) shows a maximum displacement of $0.0045\mu m$. Note the magnitude and direction of the principal stresses as some stress elements are rotated at the interphase of the Terfenol-D sensors. There was an observed maximum von Mises stress of 2 MPa at the sensor matrix interphase, as seen in Figure (3.25).

To simulate the magnetostrictive behavior of ply delamination, a 1 GPa stress was applied to the top surface of the MagCFRP model, as seen in Figure (3.26). There was an observed maximum von Mises stress of 4 GPa at the sensor matrix interphase, as seen in Figure (3.27). With this applied delamination stress came a change in the principal stress field, as seen in Figure (3.26). These changes in the stress field subsequently changed the size and orientation of the embedded Terfenol-D sensors. The applied delamination stress caused an increase in sensor area by over 83%. This increase in size also causes an increase in magnetic flux density absorption in the Terfenol-D sensors, which agrees well with the governing magnetoelasticity mechanics presented in Chapter 2. Since the applied field in this model is a constant direct magnetic field, in a real-world application, there would be an observed dropoff in magnetometry response for the delamination stress case. As seen in Figure (3.28), delamination stress results show a maximum magnetic flux density for embedded Terfenol-D sensors to be $4.5mT \pm 0.5mT$. This maximum magnetic flux density for the delamination stress simulation is also absorbed over a significantly larger area as the size of the sensors increase by over 83%.

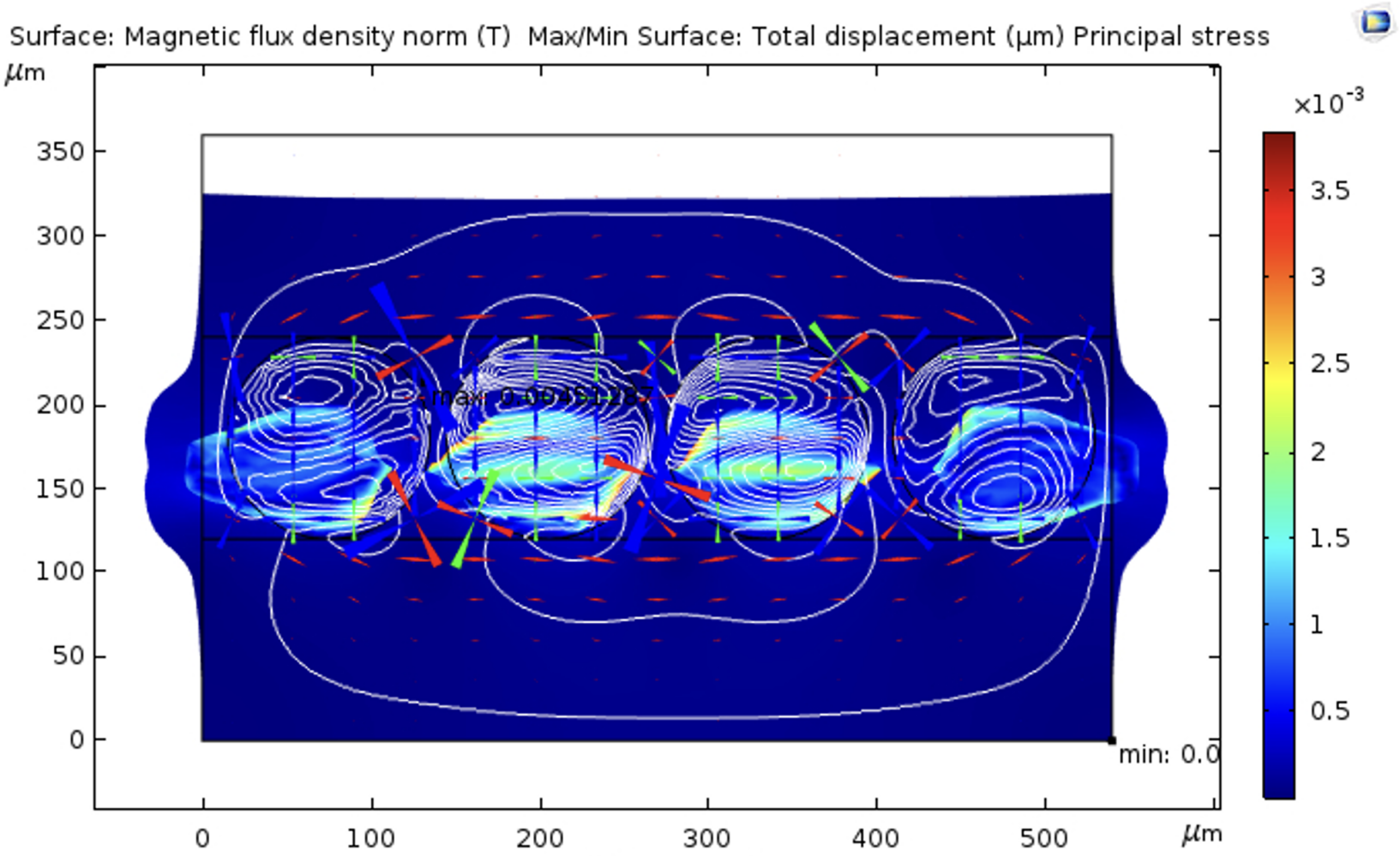

Figure 3.24: COMSOL MagCFRP fabrication response.

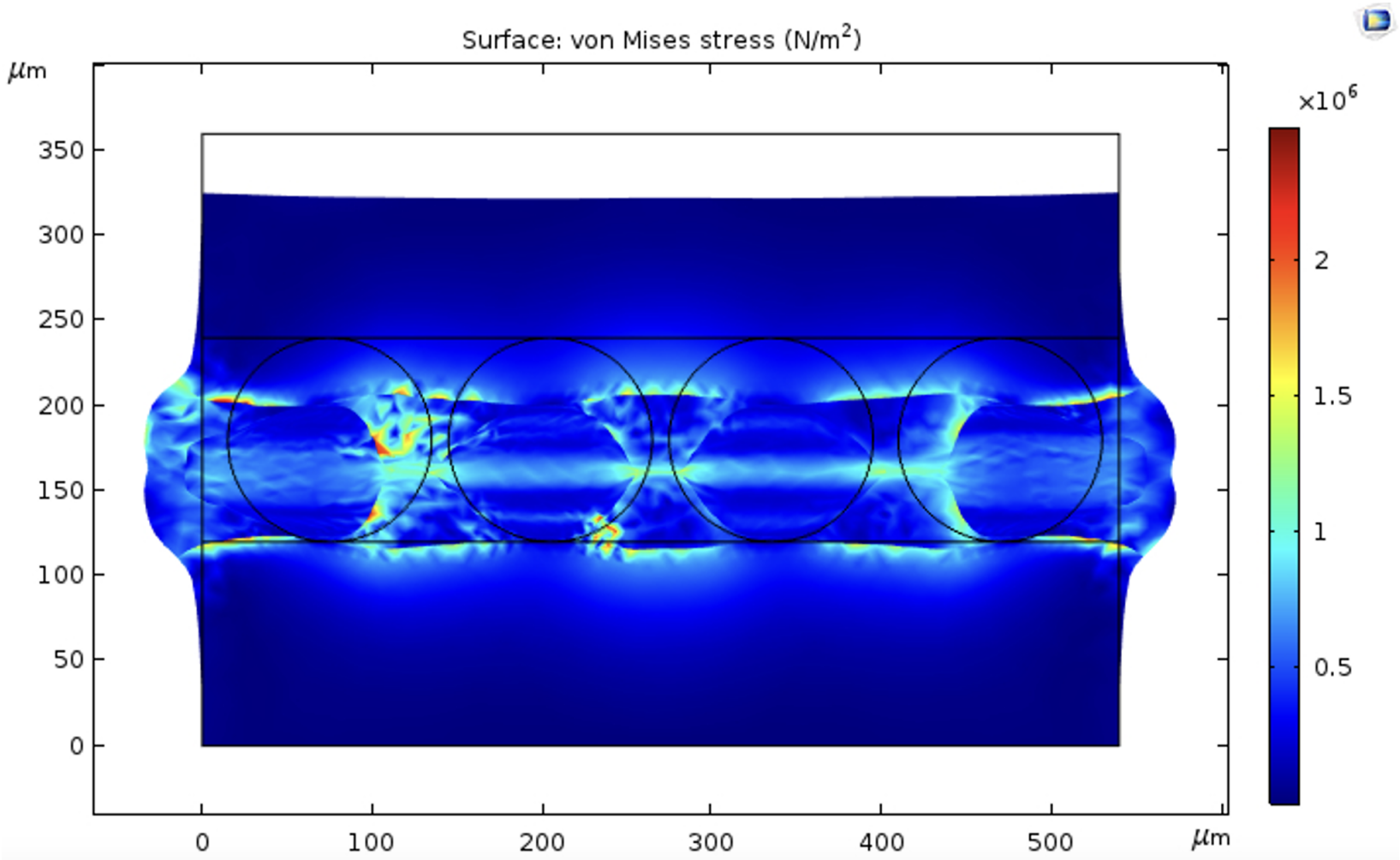

Figure 3.25: COMSOL von Mises fabrication stress field.

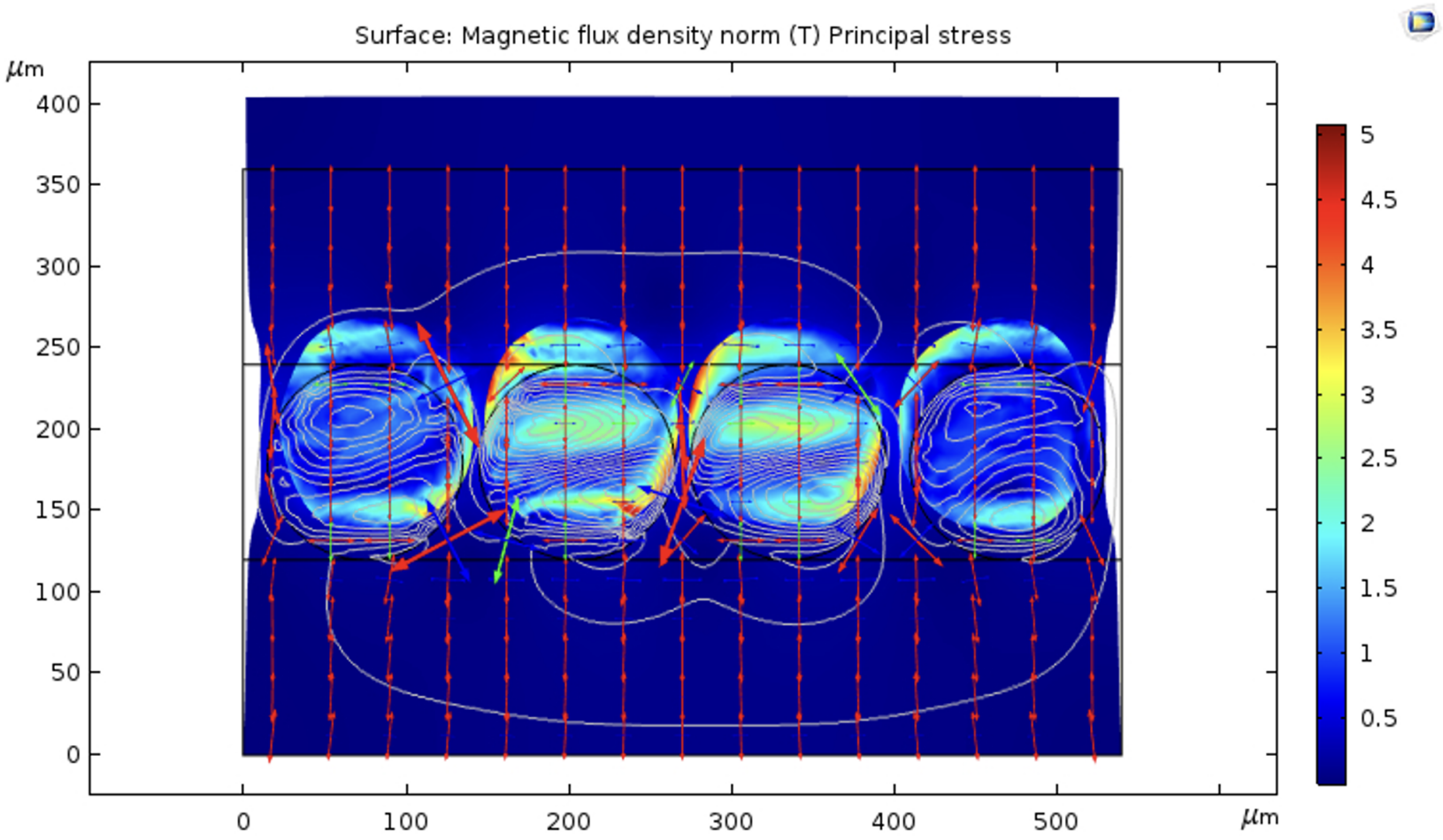

Figure 3.26: COMSOL MagCFRP delamination initiation response.

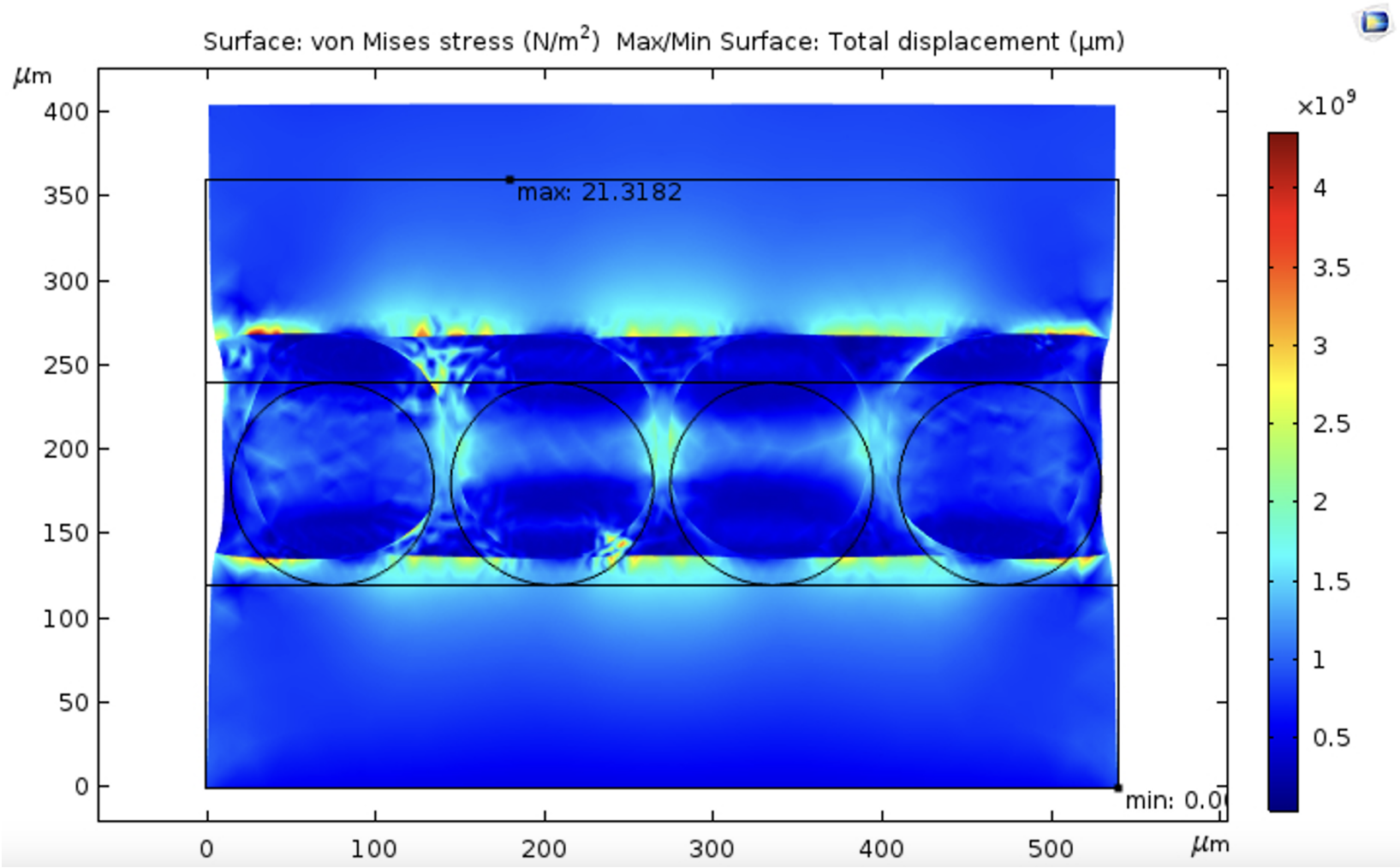

Figure 3.27: COMSOL MagCFRP delamination initiation stress field.

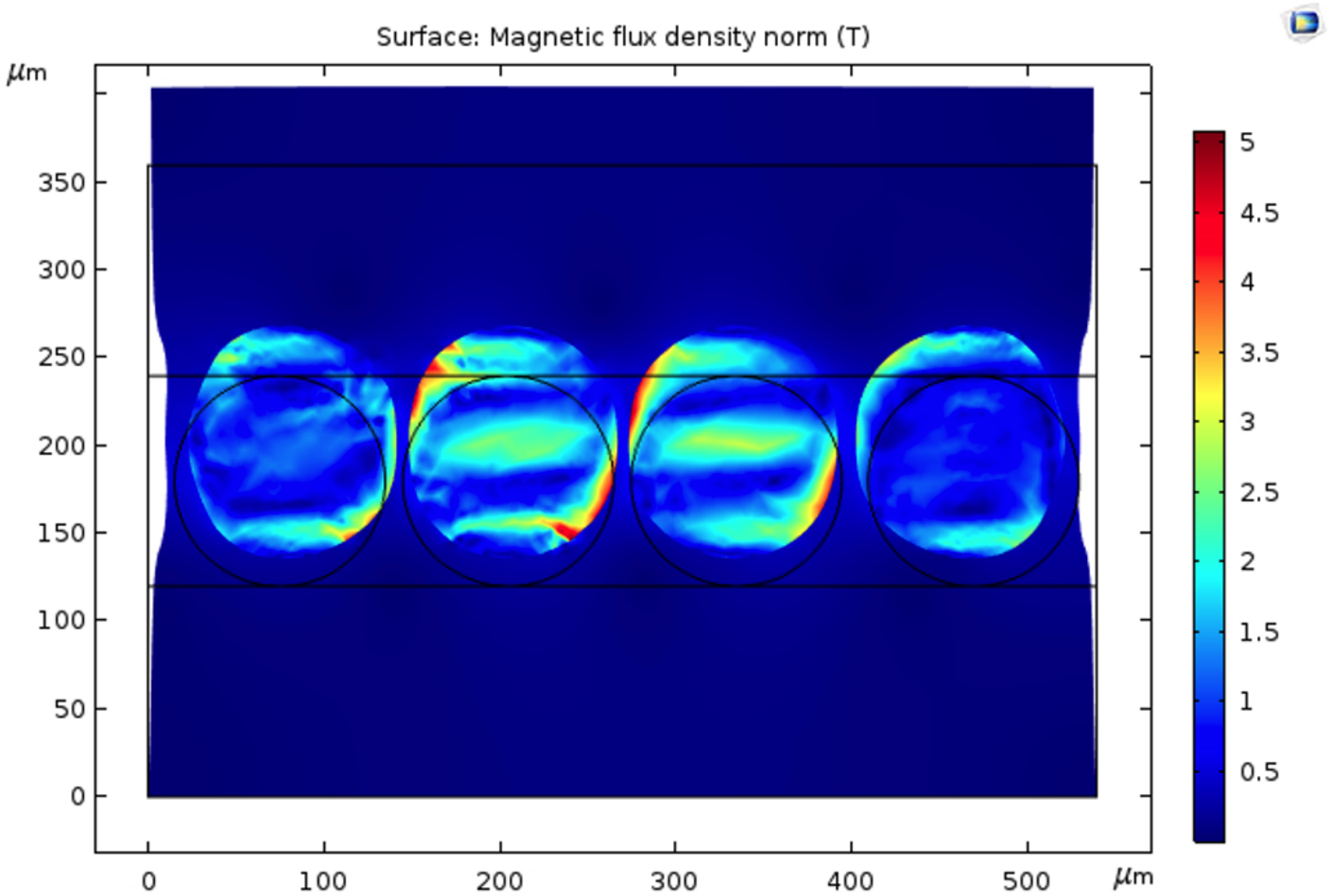

Figure 3.28: COMSOL MagCFRP delamination initiation magnetic flux density response.

3.4 Conclusion of Results

The sprinkling deposition process effectively physically deposits Terfenol-D sensors in a composite. However, it does not allow a high level of homogeneity of sensor deposition. This sprinkling deposition technique is not ideal for future production applications, as the distribution of Terfenol-D sensors is non-homogeneous on a microscopic scale. Compared to the sprinkling deposition technique, Terfenol-D sensors from the magnetoelastomer field structuring technique have superior clarity and resolution on the macro and microscopic length scale. Micro X-ray CT results in Figure (3.3) show the difference in clarity and resolution of the embedded Terfenol-D sensors on the macroscopic scale. The X-ray CT scan in Figure (3.3a) was taken at a resolution three times higher than the Figure (3.3b) scan, and the difference in sensor distribution is evident. In Figure (3.3), the difference in sensor orientation and distribution density can be seen. The conglomerations seen in Figure (3.3b) are not present in the magnetoelastomer field structuring sample in Figure (3.3a).

The difference in deposition characteristics can be studied further on the microscopic scale. Figure (3.4) shows the microscopic snapshot of the Terfenol-D sensor formation post-MagCFRP consolidation. Figure (3.4a) was taken with a 1.78-micron pixel resolution of Terfenol-D sensors deposited using the sprinkling method. Figure (3.3b) was taken with a 0.71-micron pixel resolution of Terfenol-D sensors deposited using the magnetoelastomer field structuring method. By Figure (3.4a), Terfenol-D sensor conglomeration is apparent in the sprinkling deposition method. In the magnetoelastomer field structuring snapshot, single-walled Terfenol-D sensors are oriented head to tail in the structured field direction. The sensor size in the magnetoelastomer field structuring snapshot also agrees with the manufactures specified sensor size between 38-106 microns.

While a proof of concept approach was taken in the sputtering PVD method, preliminary results have shown promising deposition characteristics in depositing thin film Terfenol-D sensors onto structural substrates. By using PVD techniques like sputtering in future works, it is possible to achieve atomistic level strain clarity and resolution for surface and delamination density propagation.

Quasi-static tests were conducted on a 15 wt% MagCFRP specimen using electromagnetic stimulation. Figure (3.7) shows 0-70% UTS quasi-static loading results from the 15 wt% MagCFRP specimen. As seen in Figure (3.7), the dominant voltage RMS variance exists between the "NO LOAD," "50% UTS", and "70 % UTS" curves. Because these results were produced by electro-

magnetic stimulation and the driving alternating magnetic field is much larger than the saturation magnetic field of Terfenol-D (i.e., $H_s << H_d$), it is challenging to physically interpret precisely what is happening during the amplitude and phase shifts seen in Figure (3.7). Nonetheless, there was an observed change in voltage RMS concerning loading intervals.

VSM measurements were taken of the 15 wt% MagCFRP specimen before and after mechanical testing. Figure (3.8) shows the observed magnetic moment change between the $45 - 135^o$ vibrating magnetometry angles before and after mechanical testing. Changes in a material's magnetization and permeability are directly related to the mechanical state of the ferroic material [17, 11]. Since the only ferroic material in MagCFRP are the Terfenol-D sensors, it can be deduced that the change in magnetization is associated with sensor reorientation within the matrix material.

Initial results for the Terfenol-D thin film samples agree well with the general mechanics of magnetoelasticity. The results show that there is an initial net decrease in magnetostrictive response by 14% in sample 1 and 8% in sample 2.

The 15 wt% MagCFRP magnetostriction analysis was performed using the direct magnetization method. As expected, there was no observed magnetoelastic response from the baseline samples that were not embedded with Terfenol-D sensors, as the CFRP is a non-ferroic material. Like the baseline samples, the 15 wt% Terfenol-D embedded MagCFRP also had an average UTS of 1.6 GPa. Although the average UTS of the baseline and 15wt% samples were the same, mechanical analysis of the stress vs. strain data showed a 4% reduction in strength and a 6% reduction in toughness between the baseline and 15 wt% samples. The baseline samples also have a higher modulus of elasticity (approx. 102 GPa) when compared to the MagCFRP samples (approx. 100 GPa), as seen in Figure (3.15).

To study the localized magnetic response, a load-controlled test was performed on a 15wt% MagCFRP specimen. As seen in Figure (3.16), an inverse relationship exists between the applied load and localized magnetic flux density, which is expected due to the aforementioned principles of magnetoelasticity. Figure (3.17) shows that 100% reversible localized magnetic flux density is achieved with a maximum load of only 40% UTS. Hamann and Shanmugham (Hamann, 2017, pp. 1–3; Shanmugham, 2004, pp. 267–274) suggest that irreversible changes in flux and strains indicate permanent damage. Since the maximum load was only 40% of the UTS (moderate damage regime), it was expected to achieve complete reversible flux.

For the severe damage response mechanical testing, the load-step increments were 5% UTS

until 70% UTS was achieved. As seen in Figure (3.18), the inverse relationship between applied loads and localized magnetic flux density still exists. However, the 100% localized reversible magnetic flux density was not achieved (reversible magnetic flux density of only 25%). This response in magnetization signifies permanent damage at the sensor-matrix interphase and the fiber-matrix interphase. Figure (3.19) is an explicit representation of the drop-off in residual magnetic density before and after 0-70% UTS testing.

When AE is coupled with the magnetostriction sensor, there is a positive correlation between the AE event intensities and the diminished magnetostriction response. For the 0-40% UTS loading interval (flux path under loading, depicted by pink line), as the stress increases, the localized magnetic flux decreases. For the 40-0% UTS loading interval (flux path load released, represented by the black line), the localized magnetic flux increases as the stress decreases. For the severe damage loading interval on 0-70% UTS, the localized magnetic flux density decreases as the stress increases. However, the rate of return of the localized magnetic flux density concerning the stress was significantly diminished. For the max load interval of 0-70% UTS, the peak AE amplitude observed was more than 100 dB, as seen in Figure (3.21).

At this dB level, mode I and mode II fiber-matrix debonding, cracking, and shear delamination failure have been initiated and propagated [1, 3]. The irreversible localized magnetic flux density is attributed to the specimen's high onset of interphacial damage. This severe level of composite damage is not what the Army would consider a damage precursor, as other traditional NDE methods could detect these defects. However, because MagCFRP is an embedded sensing smart material, delamination density propagation at this level could be tracked wirelessly throughout the structure or component's geometry continuously.

As seen in Figure (3.23), the observed deformation of the Terfenol-D sensor conglomerates occurred predominantly at the sensor-matrix interphase and did not exceed $100\mu m$. Both compression and extension deformation were observed in X-Ray CT nominal comparison images.

COMSOL FEA simulations deployed a normal constant saturation magnetic flux density over the domain to numerically simulate the direct magnetization method. As seen in Figure (3.24), COMSOL FEA results for MagCFRP fabrication stress analysis show a maximum general magnetic flux density for embedded Terfenol-D sensors to be $2.5mT \pm 0.5mT$ over a reduced sensor area from fabrication stresses and ply constraints. Figure (3.24) shows a maximum displacement of $0.0045\mu m$. There was an observed maximum von Mises stress of 2 MPa at the sensor matrix interphase, as seen

in Figure (3.25).

To simulate the magnetostrictive behavior of ply delamination, a 1 GPa stress was applied to the top surface of the MagCFRP model, as seen in Figure (3.26). There was an observed maximum von Mises stress of 4 GPa at the sensor matrix interphase, as seen in Figure (3.27). The applied delamination stress caused an increase in sensor area by over 83%. This increase in size also causes an increase in magnetic flux density absorption in the Terfenol-D sensors. Figure (3.28) shows that delamination stress results show a maximum magnetic flux density for embedded Terfenol-D sensors to be $4.5mT \pm 0.5mT$. This maximum magnetic flux density for the delamination stress simulation is also absorbed over a significantly larger area as the size of the sensors increase by over 83%.

Chapter 4

Conclusions and Discussion

4.1 MagCFRP as a Working System

As the present and future demand for advanced materials continues to grow, the science and engineering community must establish dynamic protocols to assess and analyze the instantaneous structural health of these advanced materials. One material that could answer the call for lighter and stronger materials in the automotive, aerospace, and general structural material sectors is CFRP.

While CFRPs have exceptional mechanical properties concerning their overall weight, their failure profile in demanding high-stress environments raises reliability concerns. Two crucial limiting factors in CFRP reliability are low-strain material degradation and low fracture toughness. Due to the low strain degradation characteristics of CFRP, a wide variety of damage can be sustained to the CFRP interlaminar interphase without any appreciable change to the physical structure itself. The CFRP component's capacity and overall life cycle highly depend on the composite's interlaminar Delamination density progression.

Magnetostrictive Carbon Fiber Reinforced Polymer (MagCFRP) is a self-sensing structural health composite material that is magnetically activated by an external magnetic field. MagCFRP composite constituents are carbon fiber, resin matrix, and Terfenol-D sensors. The magnetically activated Terfenol-D sensors are embedded between the lamina of the composite. These magnetostrictive embedded sensors respond to their surrounding stress field, allowing them to be used as damage sensors. By embedding Terfenol-D sensors into CFRP's matrix, creating a magnetoelastomer, real-time magnetostriction data can be tracked and analyzed.

The beauty of MagCFRP for delamination density propagation lies in its ability to wirelessly detect changes in mechanical states by monitoring one feature, that is, magnetic flux density. Pristine MagCFRP systems will have an associated pristine magnetic response that captures the physical health of the composite as it refers to localized sensor orientation and magnetization. As the structural health of the MagCFRP system is diminished due to external loads, there will be a change in the material's magnetization, ultimately due to embedded sensor reorientation at the fiber-matrix-sensor interphase. This behavior of differential magnetization, as it refers to the MagCFRP interlaminar health, is established and supported by mechanics of magnetoelasticity, magnetic material susceptibility, and conservation of internal energy methods.

While the dynamic delamination density propagation mechanics in CFRPs is not as simple as classical fracture mechanics approaches for isotropic materials, the initiation of delamination fracture mechanics of MagCFRPs can be defined by using a similar approach to Local Delamination fracture mechanics model developed by T. Kevin O'Brien and the Structures Laboratory, U.S. Army Research and Technology Laboratories (AVSCOM) and NASA Langley Research Center, Hampton, VA 23665 in Delamination and Debonding of Materials, ASTM STP [2]. By treating embedded Terfenol-D sensors as crack-tip surfaces, it is possible to define the strain energy release rate in terms of Terfenol-D sensor thickness and modulus of elasticity for small perturbations from the instantaneous delamination thickness.

Using the Composite Cylinder Assemblage (CCA) elasticity model, it is possible to express the elastic moduli of MagCFRP in terms of composite constituent concentration and material properties. Using the derived solutions for A_m, A_f, A_{TDS}, B_m, and B_{TDS} and substituting them into equation (2.74) and integrating will allow ϵ_1 to be defined in terms of material properties and an applied axial load, P. With equation (24) in Appendix A and substituting it into equation (2.36), it is possible to arrive at an analytical solution for E_1 in terms of the geometric assemblage of MagCFRP.

While the sprinkling deposition technique is effective in physically depositing Terfenol-D sensors in a composite, research in b-stage magnetoelastomer field-structuring and sputtering PVD has shown excellent results for next-gen MagCFRP deposition techniques. Sputtering PVD deposition results for MagCFRP applications have shown thin film Terfenol-D sensors can be effectively deposited on a structural substrate. However, the feasibility of using this deposition technique on a large scale is limited by the process environment and size limitations. Mass production applications

of MagCFRP will likely utilize a combination of the Terfenol-D resin bath mixture for pre-preg manufacturing and magnetoelastomer field structuring.

MD methods, such as DPD and DFT, can be used to study the behavior of complex polymer configurations like MagCFRP. When representing physical materials like Terfenol-D and resin epoxy in an atomistic simulation environment, one must consider the plethora of system parameters that must be defined to run the simulation. Many of these MD simulation parameters are defined by experimental data from the literature. In the field of magnetostrictive materials like Terfenol-D, there are limited resources that provide material characteristics presented for atomistic simulations.

L A Makarova et al. of "Tunable layered composites based on magnetoactive elastomers (MAE) and piezopolymer for sensors and energy harvesting devices have stated, "it is generally impossible to model MAE materials at an atomistic or molecular scale [7]." In other works, like "Coarse-grained molecular dynamics simulation of small ferrogel objects" by A. V. Ryzhkov et al., the authors model soft (modulus on the scale of kPa) ferrogels with MD simulation. In this work, the magnetic grains are linked to the monomers by means of special (lock) sensors [30]. These special sensors are rigidly locked to their "master" grains. After researching different atomistic methods, it was determined that it is currently impossible to model MagCFRP without compromising scientific rigor.

Mechanical tests for baseline CFRP and MagCFRP show promising material resilience characteristics, as both materials had an average UTS of 1.6 GPa. Although the average UTS of the baseline and 15wt% samples were the same, mechanical analysis of the stress vs. strain data showed a 4% reduction in strength and a 6% reduction in toughness between the baseline and 15 wt% samples. The baseline samples also have a higher modulus of elasticity (approx. 102 GPa) when compared to the MagCFRP samples (approx. 100 GPa).

The overall magnetostrictive responses from all MagCFRP testing have been within the scope of the presented governing mechanics of magnetoelasticity and general magnetization. Results from analytical, numerical, and experimental approaches agree well with one another in that sensor orientation and magnetization directly correlate with interlaminar stresses and strains, or the lack thereof. While the results presented in this work are promising, MagCFRP for delamination density propagation is still considered advanced basic research. For MagCFRP to be used in working systems, such as vehicle chassis, airframes, and other structural applications, there must be an interdisciplinary system optimization development for MagCFRP. With time and effort, MagCFRP

will be the next-gen self-sensing CFRP.

4.2 Future Work

While the presented work has established a strong mechanical foundation for MagCFRP as a self-sensing NDE material, future work is necessary to expand the fundamental knowledge base needed to integrate MagCFRP in structural components for real-time NDE. The primary future work topics include but are not limited to, MagCFRP saturation magnetization, magneto-mechanical validation, MagCFRP deposition response of sputtered and field-structured magnetoelastomer coupon, numerical geometry refinement, and MagCFRP fatigue response.

4.2.1 Saturation Magnetization

The most prominent opportunity to improve the current iteration of MagCFRP research is to induce the system to a saturation environment during testing. Terfenol-D sensors have a saturation magnetization of 1 T. Most of the current work presented in the discussion was limited to a driving magnetic flux density of 0.3-0.5 T. Dr. Derje Seifu of Morgan State University has done torque magnetometry work with 15 wt.% embedded Terfenol-D in CFRPs. His work shows that in a relatively small magnetic field (around 0.5-1 kOe or 0.05-0.1 T), the observed torque is negligible ($\pm$100 Dyne-cm for θ 0-360) when compared to magnetic fields of 20 kOe or higher where the observed torque was $\pm$1200 Dyne-cm for θ 0-360 [31]. This difference in torque magnetometry can be depicted in Figure (4.1). The recommendation for generating a saturation magnetic flux density on MagCFRP during testing and workflow system is to redeploy a revised version of the driving coil, pickup coil electromagnetic stimulation method a develop application-specific water-cooled Helmholtz Coils.

Helmholtz Coils, which are air wound coils of specified diameter connected to a power supply aligned on a common axis for the measurement and study of magnetic fields. When the Helmholtz Coils' axial distance is set and connected in series, a uniform magnetic flux is generated along the coils' neutral axis. The governing equation for the magnitude of magnetic flux produced at the center of the coil is derived from the Biot-Savart law:

$$B = \frac{32\pi NI}{5\sqrt{5}R} \times 10^{-7} T \tag{4.1}$$

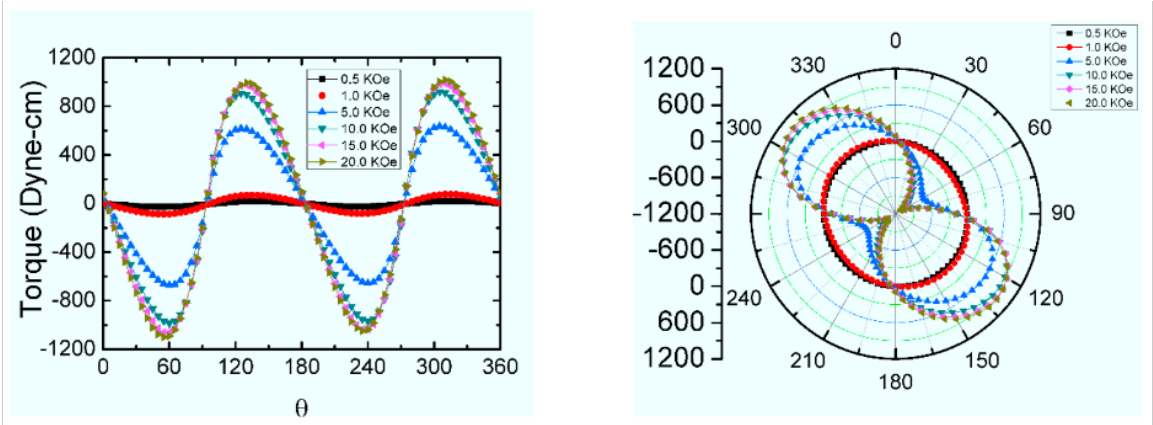

Figure 4.1: Torque magnetometry of 15 wt.% MagCFRP sample [31].

where B is the magnetic flux density, N is the number of turns around the Helmholtz Coils, I is the current, and R is the radius of the Helmholtz Coils. The coils' performance depends on their operating temperature i.e., higher coil temperature yields higher resistivity, so it is also recommended that the design implement a cooling element or a heat sink.

4.2.2 Magneto-Mechanical Validation

As mentioned in section 3.2.3, Terfenol-D sensors embedded between lamina ply can potentially increase interphase shear strength and shear modulus based on the general principles of magneto-mechanical coupling. Martin et al. have shown that orienting magnetostrictive sensors in a suitable arrangement can exhibit significant magnetostrictive stresses [21]. However, with the apropos directional magnetization of embedded Terfenol-D sensors, it is possible to tune and control MagCFRP's material response based on applied magnetization. It is necessary to understand how MagCFRP's material properties will change with varying magnetization.

4.2.3 Advanced MagCFRP Deposition Response

Sputtering and field-structured magnetoelastomer b-stage coupons can solve MagCFRP's sensor deposition concerns. In future works, it is necessary to study the general magnetostrictive response of MagCFRP concerning deposition methods. For example, the sputtering deposition technique may have the best magnetostrictive sensitivity response when compared to field-structured deposited sensors, but by how much? There needs to be future work in magnetostrictive deposition

characteristics to determine an optimal sensor deposition method based on desired material response (i.e., sensitivity).

4.2.4 Numerical Geometry Refinement

Figure (3.4b) shows that isolated Terfenol-D sensors are not spherical. Using micro X-ray CT scan results, like those found in Figure (3.4), it is possible to simulate actual geometry in a numerical environment and directly compare the results with experimental data. This approach is in sequence with section 4.2.2 in that both geometry and magneto-mechanical validation can be captured in an FEA environment and then directly compared with experimental results (i.e., localized magnetic flux density, magnetostrictive stresses, and magnetostrictive strains).

4.2.5 MagCFRP Fatigue Response

CFRP aeronautical structures, such as airframes, wings, and helicopter rotor blades, are subjected to repeated cyclic loading during use. These cyclic loadings can weaken the material over time, which decreases the component's service life. For example, a composite helicopter blade may have an approximate service life of 10,000 hours based on an interval-based model [14]. Besides MagCFRP's composite strength, other factors will contribute to the fatigue properties of MagCFRP laminates, such as stacking sequence, fiber/matrix properties, constituent geometric properties, and interfacial properties.

As mentioned in Chapter 1, the aerospace sector has many use cases for MagCFRP in structural components. For this innovation to commence, MagCFRP S-N-Localized Magnetic Flux Density response needs to be studied in great detail. Concerning delamination density propagation, S vs. N vs. Localized Magnetic Flux Density analysis has the best potential to track how delamination progresses in a pilot workpiece. The expected outcome from fatigue analysis of MagCFRP is a gradual dropoff in localized magnetic flux density as cycles increase.

Appendices

Appendix A MagCFRP Elastic Modulus by Elasticity Theory

Let:

$$\begin{aligned} C_{11}^{m} &= \phi \\ C_{12}^{m} &= \chi \\ C_{11}^{f} &= \psi \\ C_{12}^{f} &= \omega \\ C_{11}^{TDS} &= \Gamma \\ C_{12}^{TDS} &= \Delta \end{aligned} \tag{2}$$

and

$$\begin{aligned} A_m &= \alpha \\ B_m &= \beta \\ A_f &= \lambda \\ A_{TDS} &= \mu \\ B_{TDS} &= \nu \\ \epsilon_1 &= \epsilon \end{aligned} \tag{3}$$

By condition 1, and equation (2.62):

$$\begin{aligned} \lambda(a) &= \alpha(a) + \tfrac{\beta}{a} \\ \lambda &= \alpha + \tfrac{\beta}{a^2} \end{aligned} \tag{4}$$

Proceeding to condition 3 and equation (2.66):

$$\psi\lambda + \omega\lambda + \omega\epsilon = \phi\left(\alpha - \tfrac{\beta}{a^2}\right) + \chi\left(\alpha + \tfrac{\beta}{a^2}\right) + \chi\epsilon \tag{5}$$

By equation (3):

$$\psi\left(\alpha + \tfrac{\beta}{a^2}\right) + \omega\left(\alpha + \tfrac{\beta}{a^2}\right) + \omega\epsilon = \phi\left(\alpha - \tfrac{\beta}{a^2}\right) + \chi\left(\alpha + \tfrac{\beta}{a^2}\right) + \chi\epsilon \tag{6}$$

Solving for α:

$$\alpha = \frac{(\chi - \omega)\epsilon - (\psi + \omega)\left(\tfrac{\beta}{a^2}\right) + (\phi - \chi)\left(\tfrac{\beta}{a^2}\right)}{\psi + \omega - \phi + \chi} \tag{7}$$

Proceeding to condition 5 and equation (2.70):

$$\phi\left(\alpha-\frac{\beta}{c^2}\right)+\chi\left(\alpha+\frac{\beta}{c^2}\right)+\chi\epsilon=0 \tag{8}$$

Substituting α from equation (6) into equation (7):

$$\phi\left(\left(\frac{(\chi-\omega)\epsilon-(\psi+\omega)\left(\frac{\beta}{a^2}\right)+(\phi-\chi)\left(\frac{\beta}{a^2}\right)}{\psi+\omega-\phi+\chi}\right)-\frac{\beta}{c^2}\right)+\chi\left(\left(\frac{(\chi-\omega)\epsilon-(\psi+\omega)\left(\frac{\beta}{a^2}\right)+(\phi-\chi)\left(\frac{\beta}{a^2}\right)}{\psi+\omega-\phi+\chi}\right)+\frac{\beta}{c^2}\right)+\chi\epsilon=0 \tag{9}$$

Solving for β:

$$\beta=-\frac{\left(\phi(\chi-\omega)\varepsilon+\chi(\chi-\omega)\varepsilon+\chi(\psi+\omega-\phi+\chi)c^2+\chi\varepsilon\right)}{(\psi+\omega-\phi+\chi)\frac{\phi(\phi-\chi)\left(\frac{1}{a^2}\right)+\chi(\phi-\chi)\left(\frac{1}{a^2}\right)+\chi(\psi+\omega-\phi+\chi)}{\psi+\omega-\phi+\chi}} \tag{10}$$

Substituting equation (9) for β in equation (6) and simplifying:

$$\alpha=\frac{(\chi-\omega)\epsilon-(\psi+\omega)\left(\frac{-\frac{\left(\phi(\chi-\omega)\varepsilon+\chi(\chi-\omega)\varepsilon+\chi(\psi+\omega-\phi+\chi)c^2+\chi\varepsilon\right)}{(\psi+\omega-\phi+\chi)\frac{\phi(\phi-\chi)\left(\frac{1}{a^2}\right)+\chi(\phi-\chi)\left(\frac{1}{a^2}\right)+\chi(\psi+\omega-\phi+\chi)}{\psi+\omega-\phi+\chi}}}{a^2}\right)+(\phi-\chi)\left(\frac{-\frac{\left(\phi(\chi-\omega)\varepsilon+\chi(\chi-\omega)\varepsilon+\chi(\psi+\omega-\phi+\chi)c^2+\chi\varepsilon\right)}{(\psi+\omega-\phi+\chi)\frac{\phi(\phi-\chi)\left(\frac{1}{a^2}\right)+\chi(\phi-\chi)\left(\frac{1}{a^2}\right)+\chi(\psi+\omega-\phi+\chi)}{\psi+\omega-\phi+\chi}}}{a^2}\right)}{\psi+\omega-\phi+\chi}$$

$$\alpha=\frac{(\chi-\omega)\varepsilon+(\psi+\omega+\phi-\chi)\left(\phi(\chi-\omega)\varepsilon+\chi(\chi-\omega)\varepsilon+\chi(\psi+\omega-\phi+\chi)c^2+\chi\varepsilon\right)}{\left(\phi(\phi-\chi)\left(\frac{1}{a^2}\right)+\chi(\phi-\chi)\left(\frac{1}{a^2}\right)+\chi(\psi+\omega-\phi+\chi)\right)(\psi+\omega-\phi+\chi)} \tag{11}$$

With this, equation (3) becomes:

$$\lambda=\frac{(\chi-\omega)\varepsilon+(\psi+\omega+\phi-\chi)\left(\phi(\chi-\omega)\varepsilon+\chi(\chi-\omega)\varepsilon+\chi(\psi+\omega-\phi+\chi)c^2+\chi\varepsilon\right)}{\left(\phi(\phi-\chi)\left(\frac{1}{a^2}\right)+\chi(\phi-\chi)\left(\frac{1}{a^2}\right)+\chi(\psi+\omega-\phi+\chi)\right)(\psi+\omega-\phi+\chi)}+\frac{-\frac{\left(\phi(\chi-\omega)\varepsilon+\chi(\chi-\omega)\varepsilon+\chi(\psi+\omega-\phi+\chi)c^2+\chi\varepsilon\right)}{(\psi+\omega-\phi+\chi)\frac{\phi(\phi-\chi)\left(\frac{1}{a^2}\right)+\chi(\phi-\chi)\left(\frac{1}{a^2}\right)+\chi(\psi+\omega-\phi+\chi)}{\psi+\omega-\phi+\chi}}}{a^2} \tag{12}$$

Simplifying:

$$\lambda=\frac{(\chi-\omega)\varepsilon+(\psi+\omega+\phi-\chi)\left(\phi(\chi-\omega)\varepsilon+\chi(\chi-\omega)\varepsilon+\chi(\psi+\omega-\phi+\chi)c^2+\chi\varepsilon\right)}{\left(\phi(\phi-\chi)\left(\frac{1}{a^2}\right)+\chi(\phi-\chi)\left(\frac{1}{a^2}\right)+\chi(\psi+\omega-\phi+\chi)\right)(\psi+\omega-\phi+\chi)} \tag{13}$$

Proceeding to condition 2, and equation (2.64):

$$\begin{aligned}\alpha(b)+\tfrac{\beta}{b}&=\mu b+\tfrac{\nu}{b}\\ \mu&=\alpha+\tfrac{\beta}{b^2}-\tfrac{\nu}{b^2}\end{aligned} \tag{14}$$

Proceeding to condition 4, and equation (2.68):

$$\begin{aligned}&\phi\left(\alpha-\tfrac{\beta}{b^2}\right)+\chi\left(\alpha+\tfrac{\beta}{b^2}\right)+\chi\epsilon=\\&\Gamma\left(\mu-\tfrac{\nu}{b^2}\right)+\Delta\left(\mu+\tfrac{\nu}{b^2}\right)+\Delta\epsilon\end{aligned}\tag{15}$$

Substituting μ from equation (13) into equation (14):

$$\begin{aligned}&\phi\left(\alpha-\tfrac{\beta}{b^2}\right)+\chi\left(\alpha+\tfrac{\beta}{b^2}\right)+\chi\epsilon=\\&\Gamma\left(\alpha+\tfrac{\beta}{b^2}-\tfrac{\nu}{b^2}-\tfrac{\nu}{b^2}\right)+\Delta\left(\alpha+\tfrac{\beta}{b^2}-\tfrac{\nu}{b^2}+\tfrac{\nu}{b^2}\right)+\Delta\epsilon\end{aligned}\tag{16}$$

Solving for ν:

$$\nu=\frac{b^2}{2\Gamma}\left(\chi\varepsilon-(\phi+\chi-\Gamma-\Delta)\alpha-(\chi-\phi-\Gamma+\Delta)\left(\frac{\beta}{b^2}\right)\right)\tag{17}$$

Substituting α and β into equation (16):

$$\begin{aligned}&\nu=\tfrac{b^2}{2\Gamma}(\chi\varepsilon-(\phi+\chi-\Gamma-\Delta)\frac{(\chi-\omega)\varepsilon+(\psi+\omega+\phi-\chi)\left(\phi(\chi-\omega)\varepsilon+\chi(\chi-\omega)\varepsilon+\chi(\psi+\omega-\phi+\chi)c^2+\chi\varepsilon\right)}{\left(\phi(\phi-\chi)\left(\frac{1}{a^2}\right)+\chi(\phi-\chi)\left(\frac{1}{a^2}\right)+\chi(\psi+\omega-\phi+\chi)\right)(\psi+\omega-\phi+\chi)}-...\\&...-(\chi-\phi-\Gamma+\Delta)\left(\frac{-\frac{\left(\phi(\chi-\omega)\varepsilon+\chi(\chi-\omega)\varepsilon+\chi(\psi+\omega-\phi+\chi)c^2+\chi\varepsilon\right)}{(\psi+\omega-\phi+\chi)\frac{\phi(\phi-\chi)\left(\frac{1}{a^2}\right)+\chi(\phi-\chi)\left(\frac{1}{a^2}\right)+\chi(\psi+\omega-\phi+\chi)}{\psi+\omega-\phi+\chi}}}{b^2}\right))\end{aligned}\tag{18}$$

Simplifying:

$$\begin{aligned}&\nu=\tfrac{1}{2\Gamma}(b^2\chi\varepsilon-(\phi+\chi-\Gamma-\Delta)\frac{(\chi-\omega)\varepsilon+(\psi+\omega+\phi-\chi)\left(\phi(\chi-\omega)\varepsilon+\chi(\chi-\omega)\varepsilon+\chi(\psi+\omega-\phi+\chi)c^2+\chi\varepsilon\right)}{\frac{\phi(\phi-\chi)\left(\frac{1}{a^2}\right)+\chi(\phi-\chi)\left(\frac{1}{a^2}\right)+\chi(\psi+\omega-\phi+\chi)}{\psi+\omega-\phi+\chi}}-\Gamma-...\\&...-\frac{\left(\phi(\chi-\omega)\varepsilon+\chi(\chi-\omega)\varepsilon+\chi(\psi+\omega-\phi+\chi)c^2+\chi\varepsilon\right)}{(\psi+\omega-\phi+\chi)\frac{\phi(\phi-\chi)\left(\frac{1}{a^2}\right)+\chi(\phi-\chi)\left(\frac{1}{a^2}\right)+\chi(\psi+\omega-\phi+\chi)}{\psi+\omega-\phi+\chi}})\end{aligned}\tag{19}$$

Substituting ν from equation (18) into equation (13):

$$\begin{aligned}&\mu=\alpha+\tfrac{\beta}{b^2}-\tfrac{1}{2\Gamma b^2}(b^2\chi\varepsilon-(\phi+\chi-\Gamma-\Delta)\frac{(\chi-\omega)\varepsilon+(\psi+\omega+\phi-\chi)\left(\phi(\chi-\omega)\varepsilon+\chi(\chi-\omega)\varepsilon+\chi(\psi+\omega-\phi+\chi)c^2+\chi\varepsilon\right)}{\frac{\phi(\phi-\chi)\left(\frac{1}{a^2}\right)+\chi(\phi-\chi)\left(\frac{1}{a^2}\right)+\chi(\psi+\omega-\phi+\chi)}{\psi+\omega-\phi+\chi}}-\frac{\Gamma}{b^2}-...\\&...-\frac{\left(\phi(\chi-\omega)\varepsilon+\chi(\chi-\omega)\varepsilon+\chi(\psi+\omega-\phi+\chi)c^2+\chi\varepsilon\right)}{b^2(\psi+\omega-\phi+\chi)\frac{\phi(\phi-\chi)\left(\frac{1}{a^2}\right)+\chi(\phi-\chi)\left(\frac{1}{a^2}\right)+\chi(\psi+\omega-\phi+\chi)}{\psi+\omega-\phi+\chi}})\end{aligned}\tag{20}$$

Substituting α and β into equation (19) and simplifying:

$$\mu=-\frac{\frac{1}{2\Gamma}\left[b^2\chi-(\phi+\Gamma-\Delta)(\psi+\omega)\right]}{b^2}\tag{21}$$

Proceeding through equation (2.75):

$$\begin{aligned}&\textstyle\int_0^a (2\omega\lambda + \psi\epsilon_1) 2\pi r dr + \\ &\textstyle\int_a^c \left(\chi\left(\alpha - \frac{\beta}{r^2}\right) + \chi\left(\alpha + \frac{\beta}{r^2}\right) + \phi\epsilon_1\right) 2\pi r dr + \\ &\textstyle\int_b^c \left(\Delta\left(\mu - \frac{\nu}{r^2}\right) + \Delta\left(\mu + \frac{\nu}{r^2}\right) + \Gamma\epsilon_1\right) 2\pi r dr = P\end{aligned} \tag{22}$$

$$(2\omega\lambda + \psi\epsilon)\pi a^2 + \pi(2\alpha\chi + \epsilon\phi)(c^2 - a^2) + \pi\,(c-b)\,(c+b)\,(2\Delta\mu + \epsilon\Gamma) = P \tag{23}$$

Substituting α, λ, and μ into equation (22):

$$\begin{aligned}&(2\omega \tfrac{(\chi-\omega)\varepsilon+(\psi+\omega+\phi-\chi)\left(\phi(\chi-\omega)\varepsilon+\chi(\chi-\omega)\varepsilon+\chi(\psi+\omega-\phi+\chi)c^2+\chi\varepsilon\right)}{\left(\phi(\phi-\chi)\left(\frac{1}{a^2}\right)+\chi(\phi-\chi)\left(\frac{1}{a^2}\right)+\chi(\psi+\omega-\phi+\chi)\right)(\psi+\omega-\phi+\chi)} + \psi\epsilon)\pi a^2 + ... \\ &... + \pi(2\tfrac{(\chi-\omega)\varepsilon+(\psi+\omega+\phi-\chi)\left(\phi(\chi-\omega)\varepsilon+\chi(\chi-\omega)\varepsilon+\chi(\psi+\omega-\phi+\chi)c^2+\chi\varepsilon\right)}{\left(\phi(\phi-\chi)\left(\frac{1}{a^2}\right)+\chi(\phi-\chi)\left(\frac{1}{a^2}\right)+\chi(\psi+\omega-\phi+\chi)\right)(\psi+\omega-\phi+\chi)}\chi + \epsilon\phi)(c^2 - a^2) + ... \\ &... + \pi\,(c-b)\,(c+b)\left(2\Delta - \tfrac{\frac{1}{2\Gamma}(b^2\chi - (\phi+\Gamma-\Delta)(\psi+\omega))}{b^2} + \epsilon\Gamma\right) = P\end{aligned} \tag{24}$$

$$\epsilon = \frac{P \cdot \left(\phi(\phi-\chi)\left(\frac{1}{a^2}\right)+\chi(\phi-\chi)\left(\frac{1}{a^2}\right)+\chi(\psi+\omega-\phi+\chi)\right)(\psi+\omega-\phi+\chi)}{\left(2\omega(\chi-\omega)+\pi(\chi-\omega)+\left(2\omega(\psi+\omega+\phi-\chi)\phi+(\psi+\omega+\phi-\chi)(2\chi\phi+\chi(\psi+\omega-\phi+\chi)c^2)+\pi\left(2\chi\phi-\chi(\phi-\chi)\left(\frac{1}{a^2}\right)-\chi(\psi+\omega-\phi+\chi)\right)(c^2-a^2)\right)+\pi(c-b)(c+b)\left(2\Delta-\frac{\frac{1}{2\Gamma}(b^2\chi-(\phi+\Gamma-\Delta)(\psi+\omega))}{b^2}\right)\right)} \tag{25}$$

Appendix B COMSOL Setup Figures

Next Page.

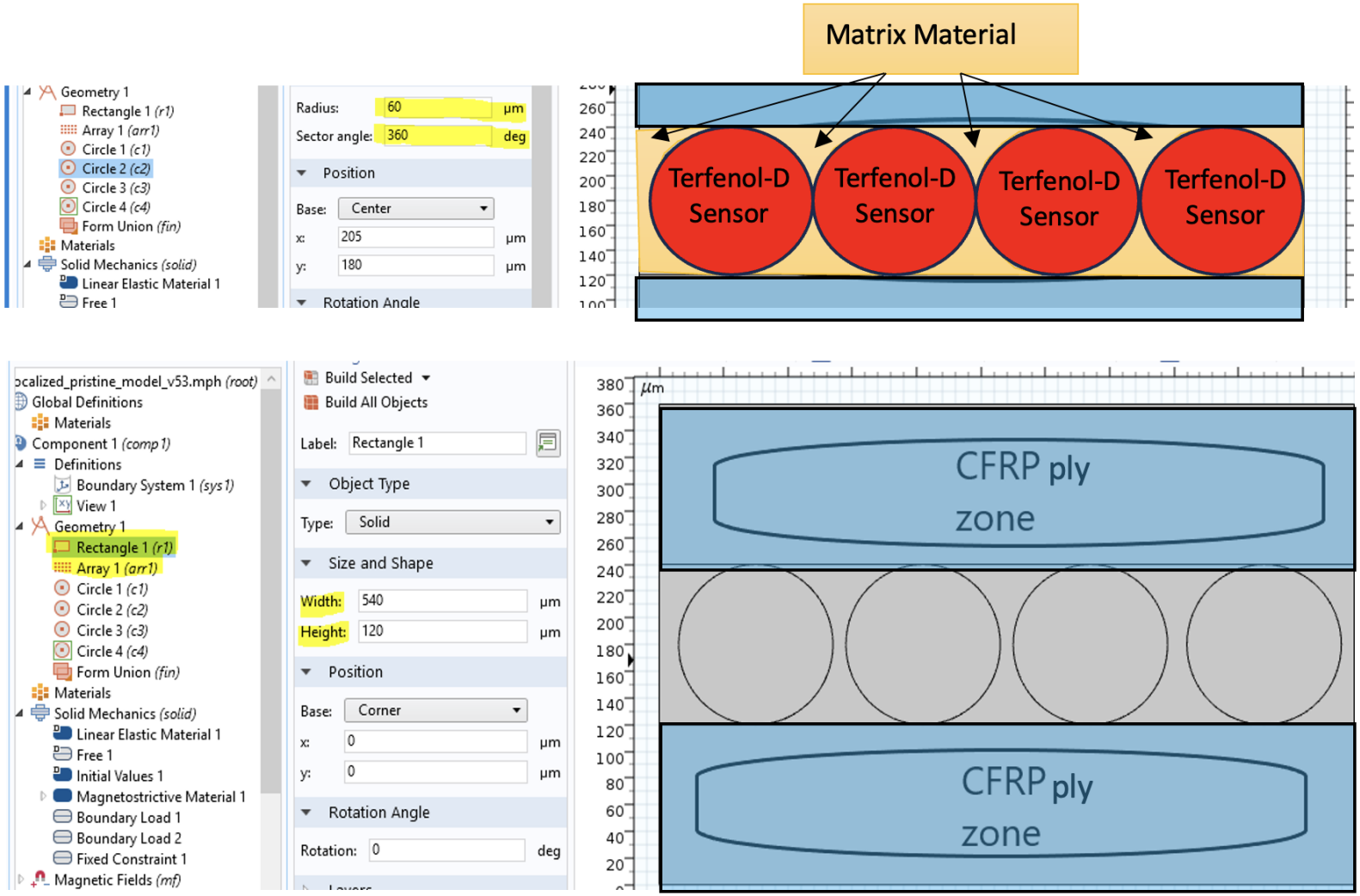

Figure 2: COMSOL geometry construction.

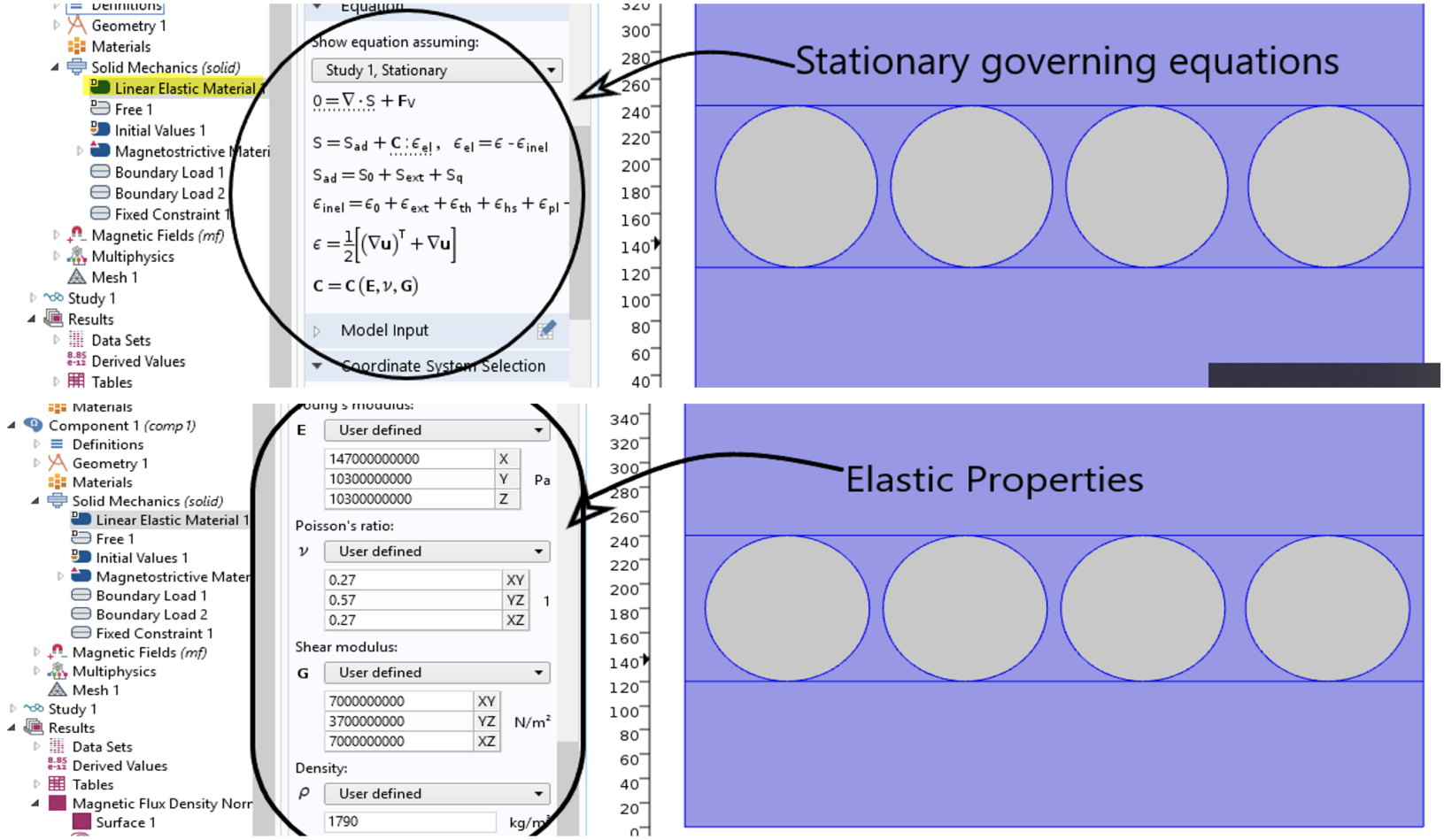

Figure 3: COMSOL solid mechanics.

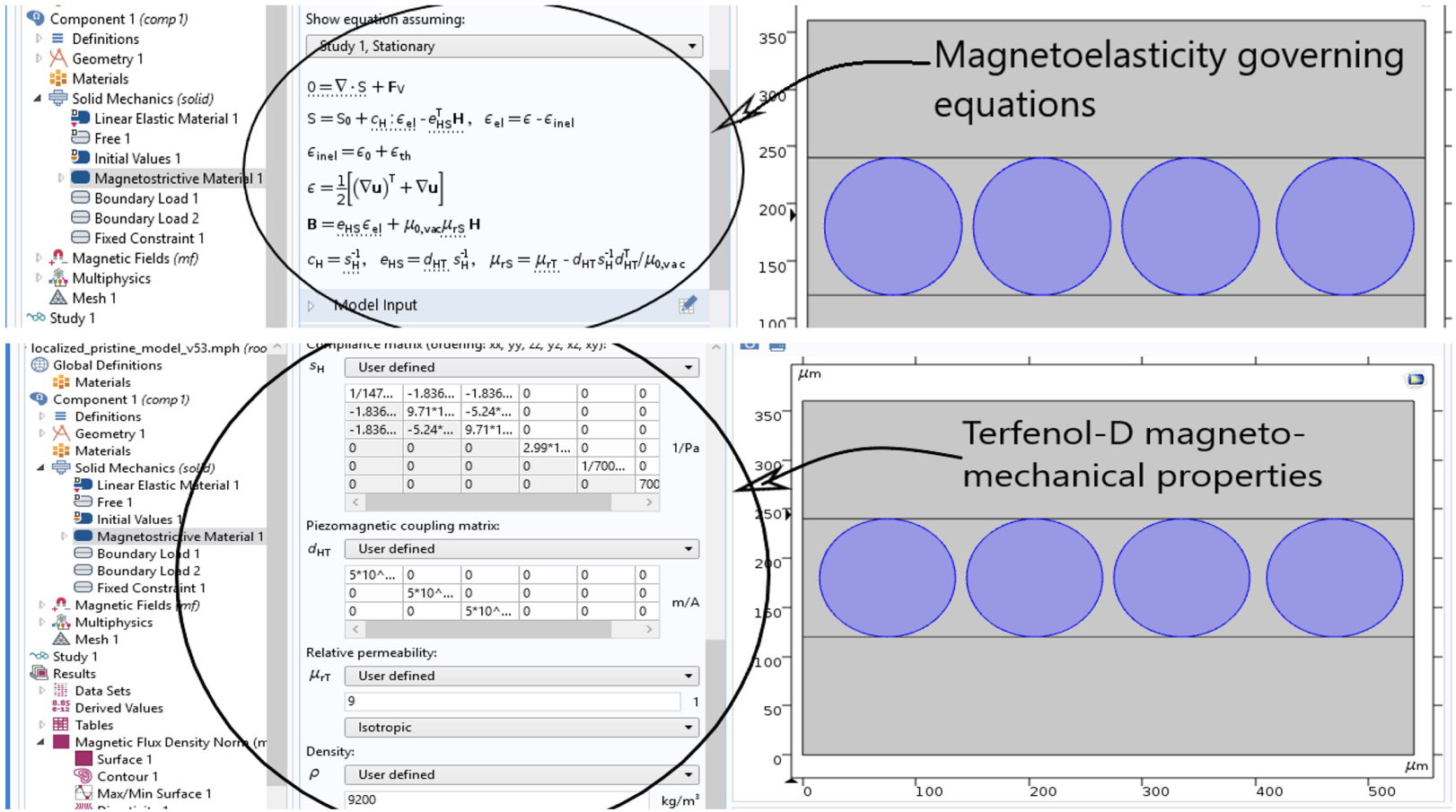

Figure 4: COMSOL magnetostrictive assignment.

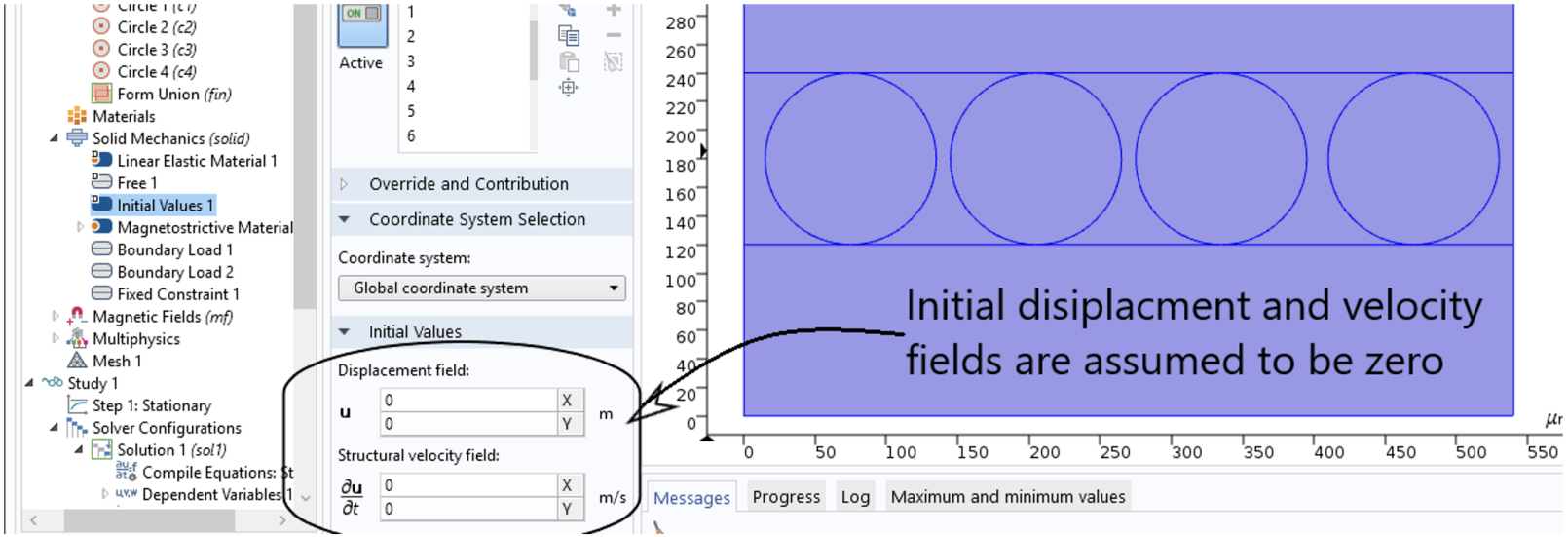

Figure 5: COMSOL displacement and velocity initialization.

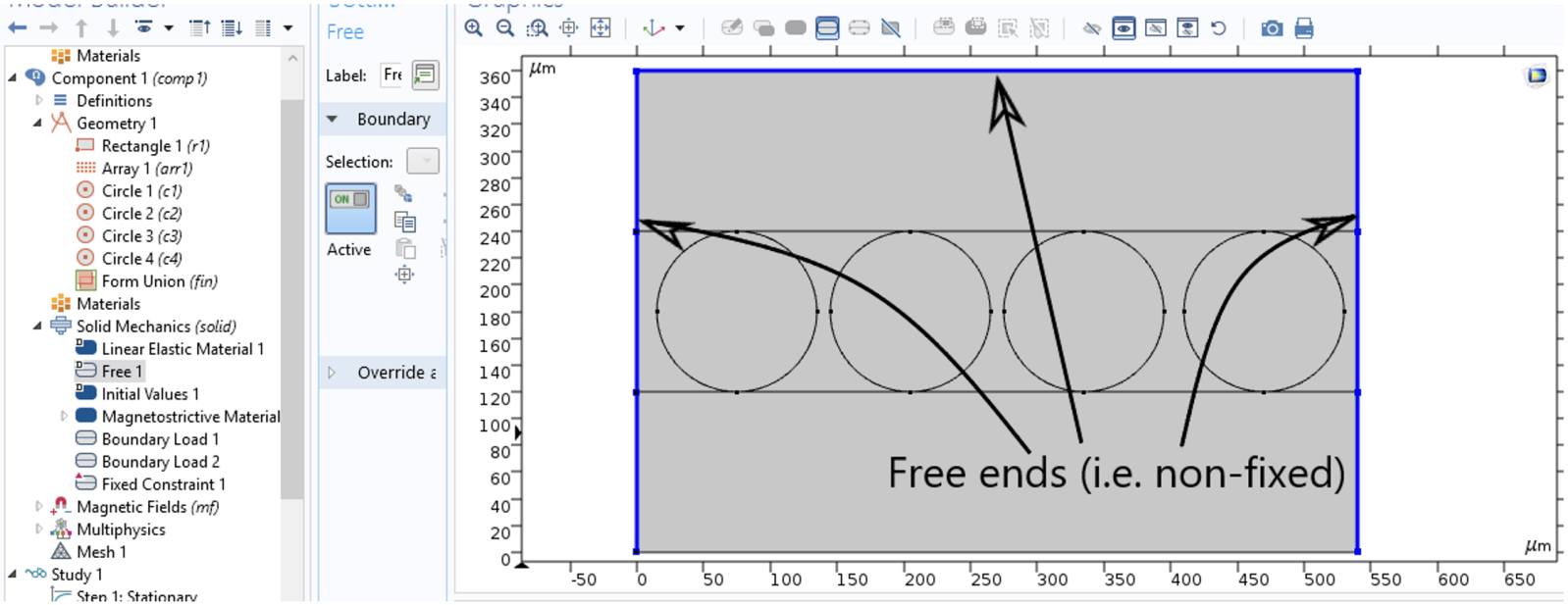

Figure 6: COMSOL boundary condition and free surface initialization.

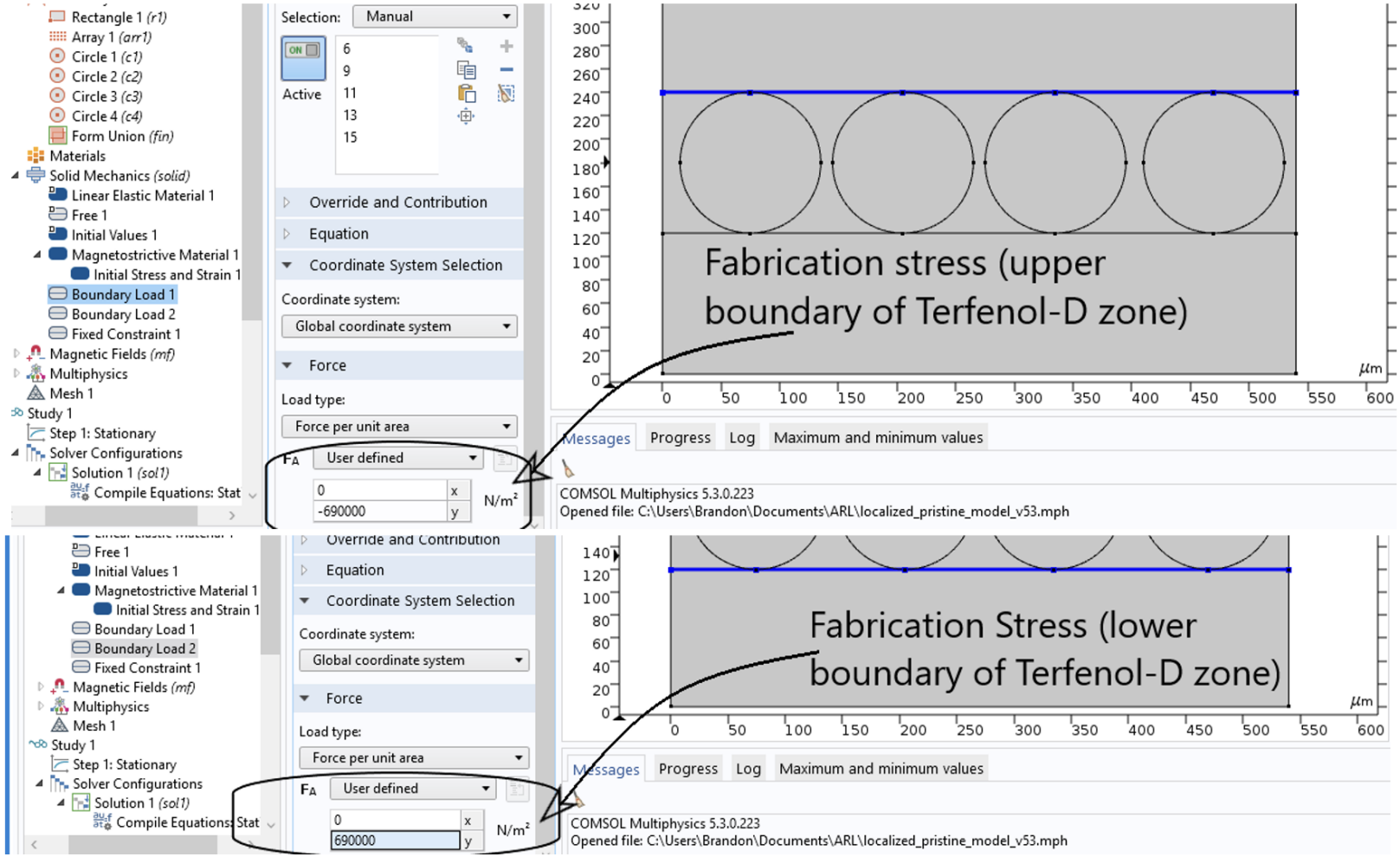

Figure 7: COMSOL fabrication stress initialization.

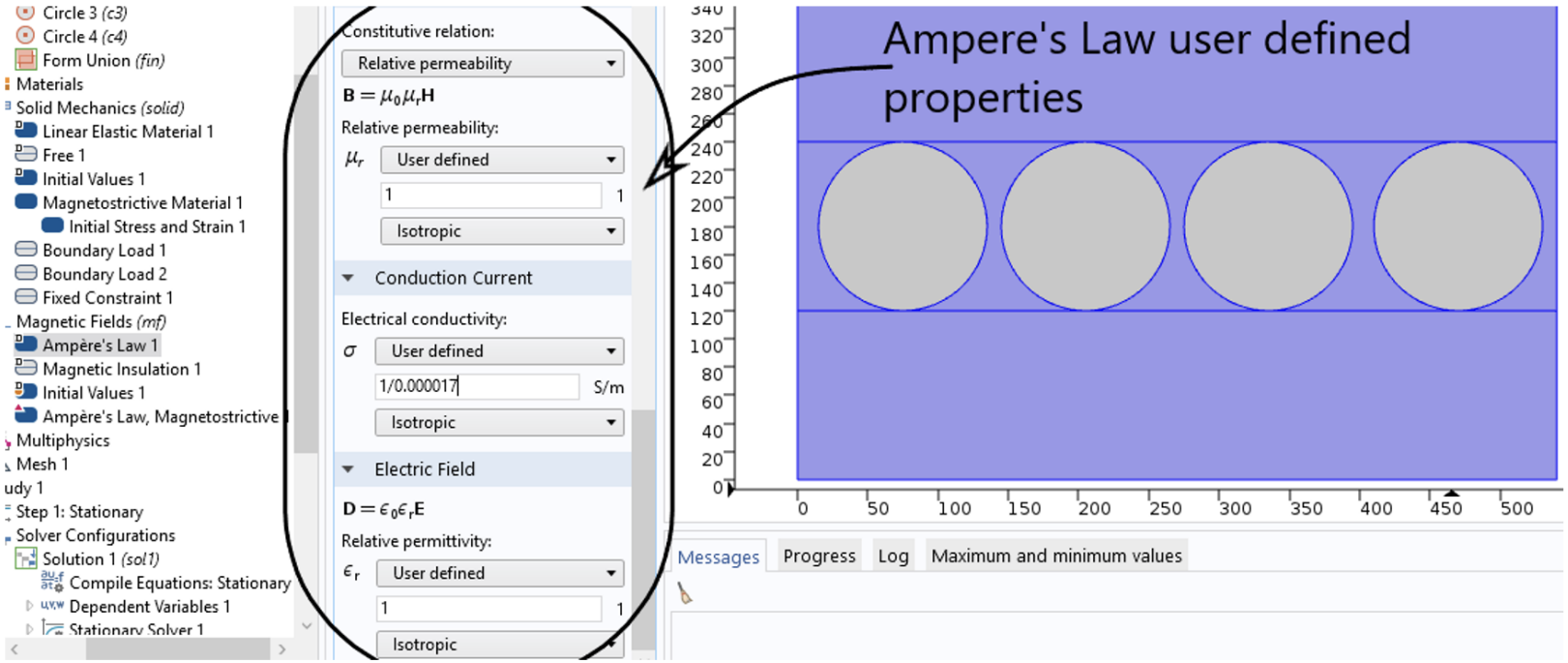

Figure 8: COMSOL Ampere's Law for CFRP initialization.

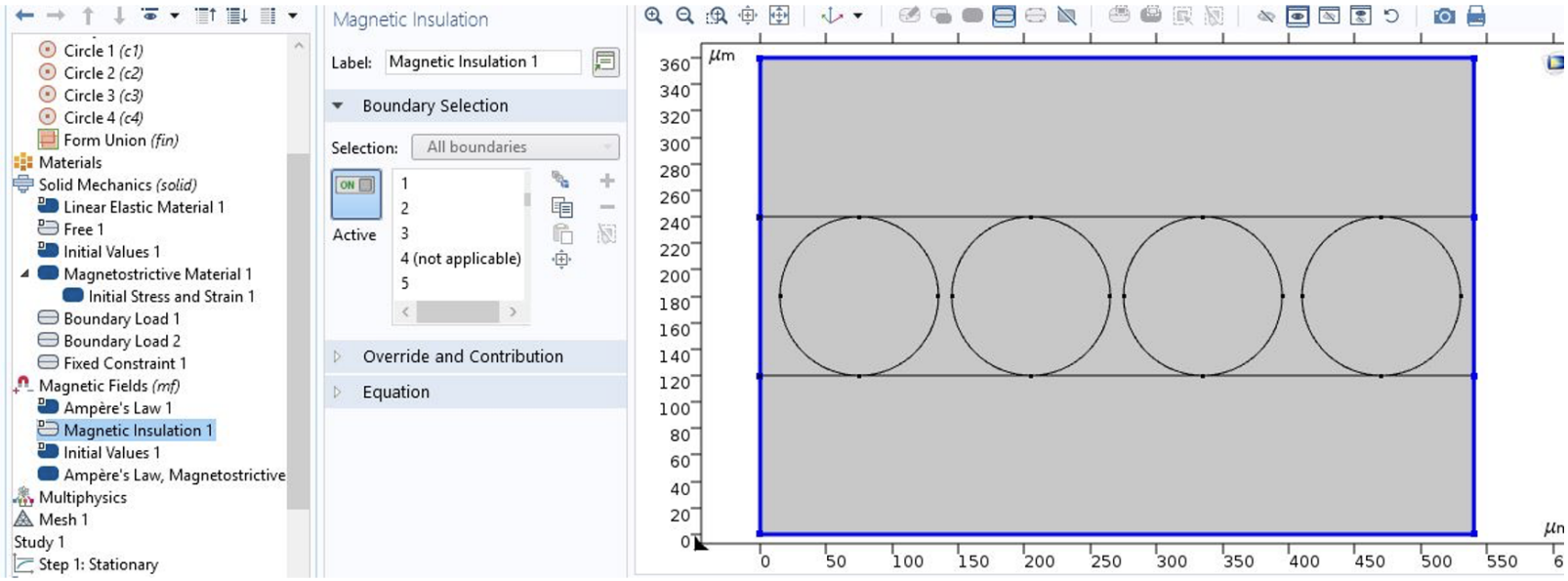

Figure 9: COMSOL magnetic insulation 1.

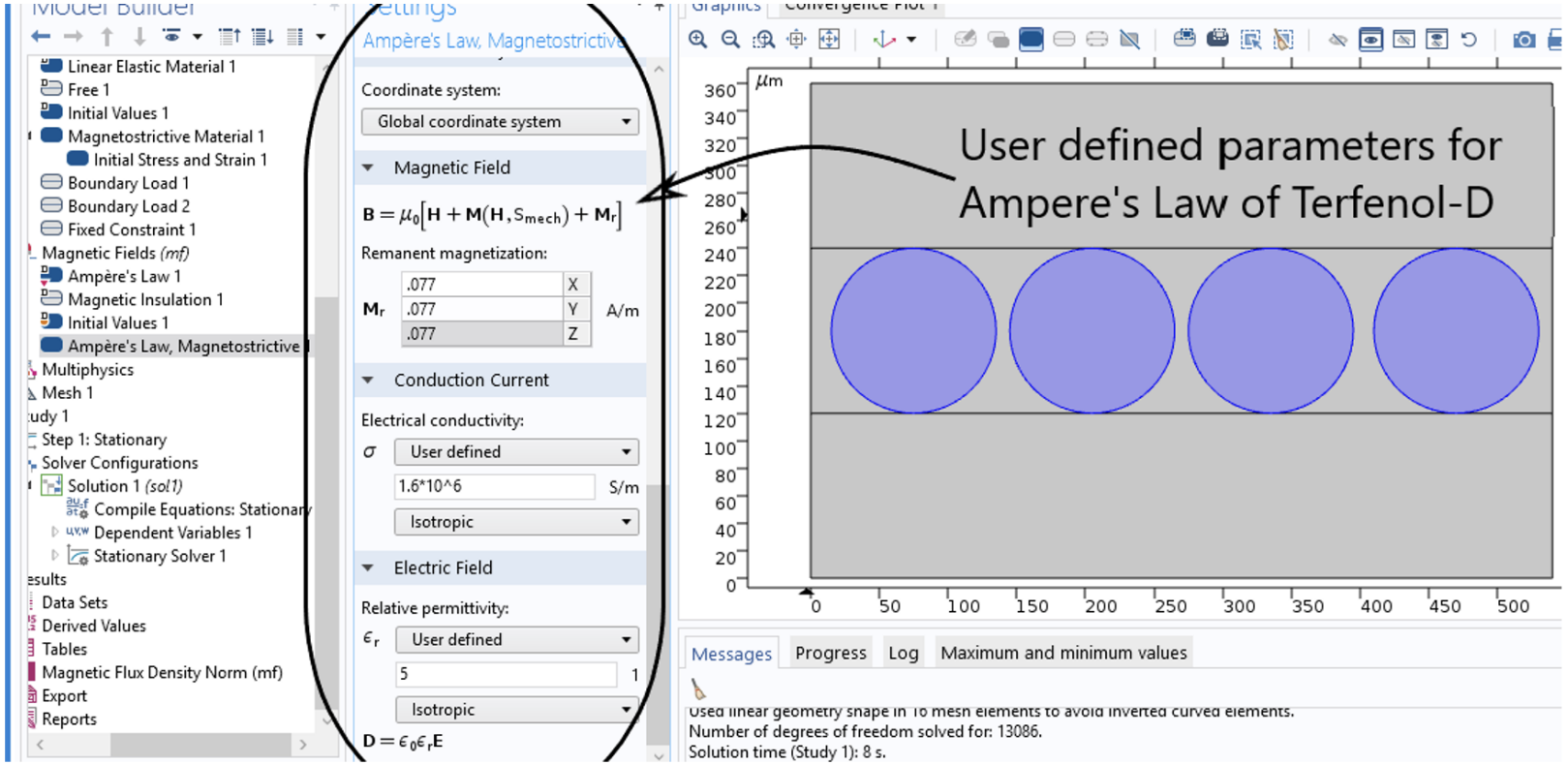

Figure 10: COMSOL Ampere's Law initialization for magnetostrictive sensors.

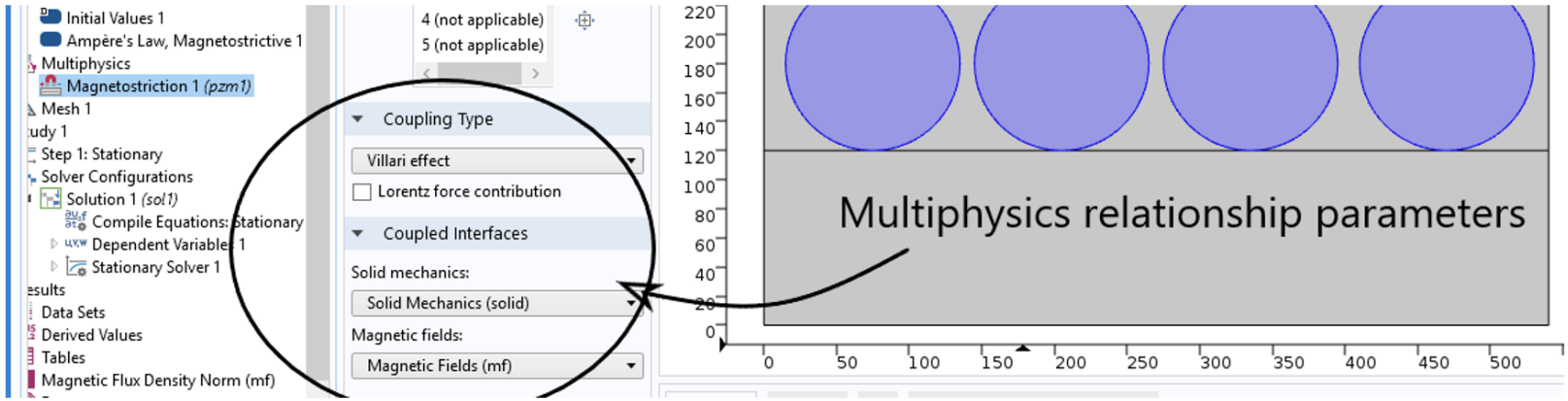

Figure 11: COMSOL magnetostriction definitions for sensors.

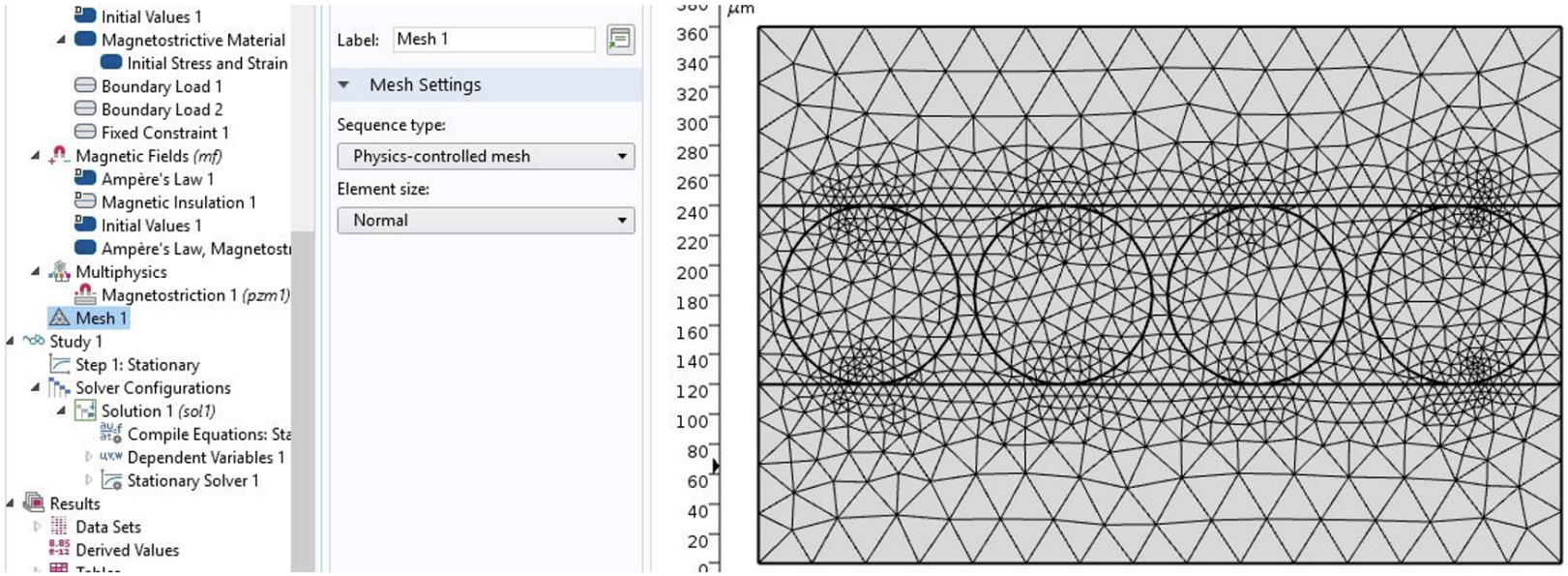

Figure 12: COMSOL physics driven discretization for MagCFRP.

Appendix C Relavent Tables and Figures

CFRP Base Material	IM7-HEXCEL 8555
Composite Fabrication Process	Vacuum Assisted Autoclave
Stacking Sequence	$[0/90/0]_s$
Number of Plies	6
Dimension of Panel	$(203.2 \times 203.2)\ mm$
Tabbing Material	G-10
Tabbing Adhesive	HYSOL 9309
MagCFRP Sensor Area	2580.6 mm^2
Specimen Width	25.4 mm
Specimen Thickness	1.26 mm

Table 1: MagCFRP test specifications

Terfenol-D Properties	**Value-Range**	**Comments**
Chemical Composition		$Tb_{0.3}Dy_{0.7}Fe_{1.92}$
Density	9200-9300 kg/m^2	
Young's modulus	50-90 GPa	Strength at constant saturation flux density
Tensile strength	28-40 MPa	
Compressive Strength	300-880 MPa	
Specific heat	0.33 kJ/(kg-K)	
Thermal conductivity	13.5 W/(m-K)	@ 25^oC
Curie temperature	380^oC	
Relative permeability μ^σ	9.0-12.0	Permeability at constant stress
Relative permeability μ^ϵ	3.0-5.0	Permeability at constant strain
Saturation Magnetization	1 T	Close proximity
Magneto-mechanical Coupling Coefficient k_{33}	0.6-0.85	Application specific
Magnetostrictive Coefficient d_{33}	2.0-20 nm/A	Application specific
Sensor Diameter	38-106 μ	
Poissons ration	0.3	

Table 2: Terfenol-D sensor properties

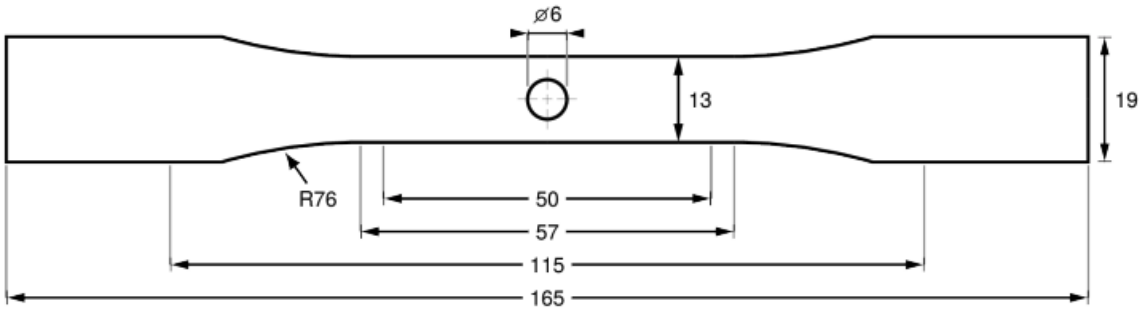

Figure 13: Onyx test coupon specifications Nelon et al. Measurements are in mm. Thickness = 3.2 mm

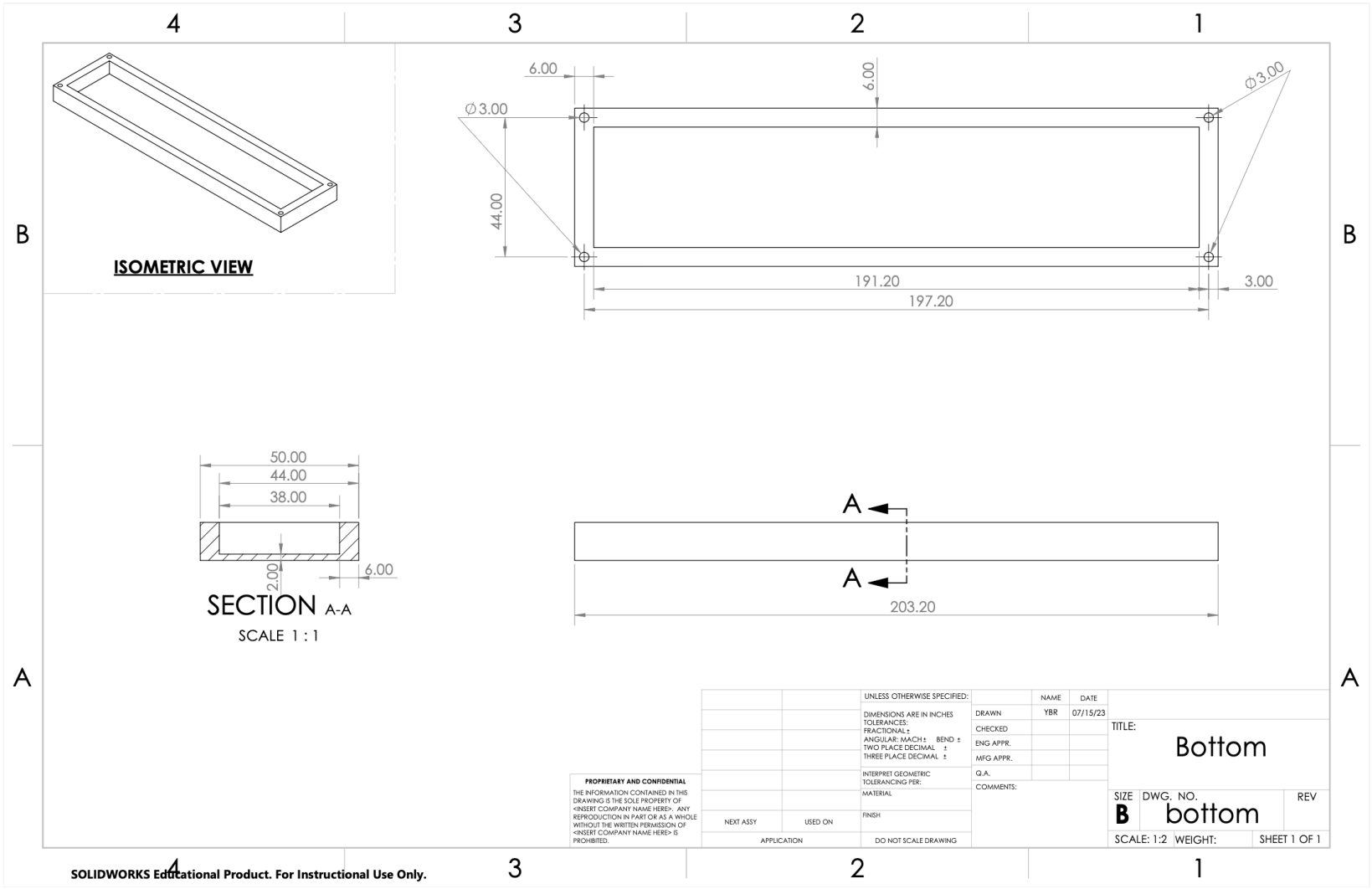

Figure 14: Silicon mold dye engineering drawing (bottom). Designed by Brandon Williams, modeled by Yogesh Rana.

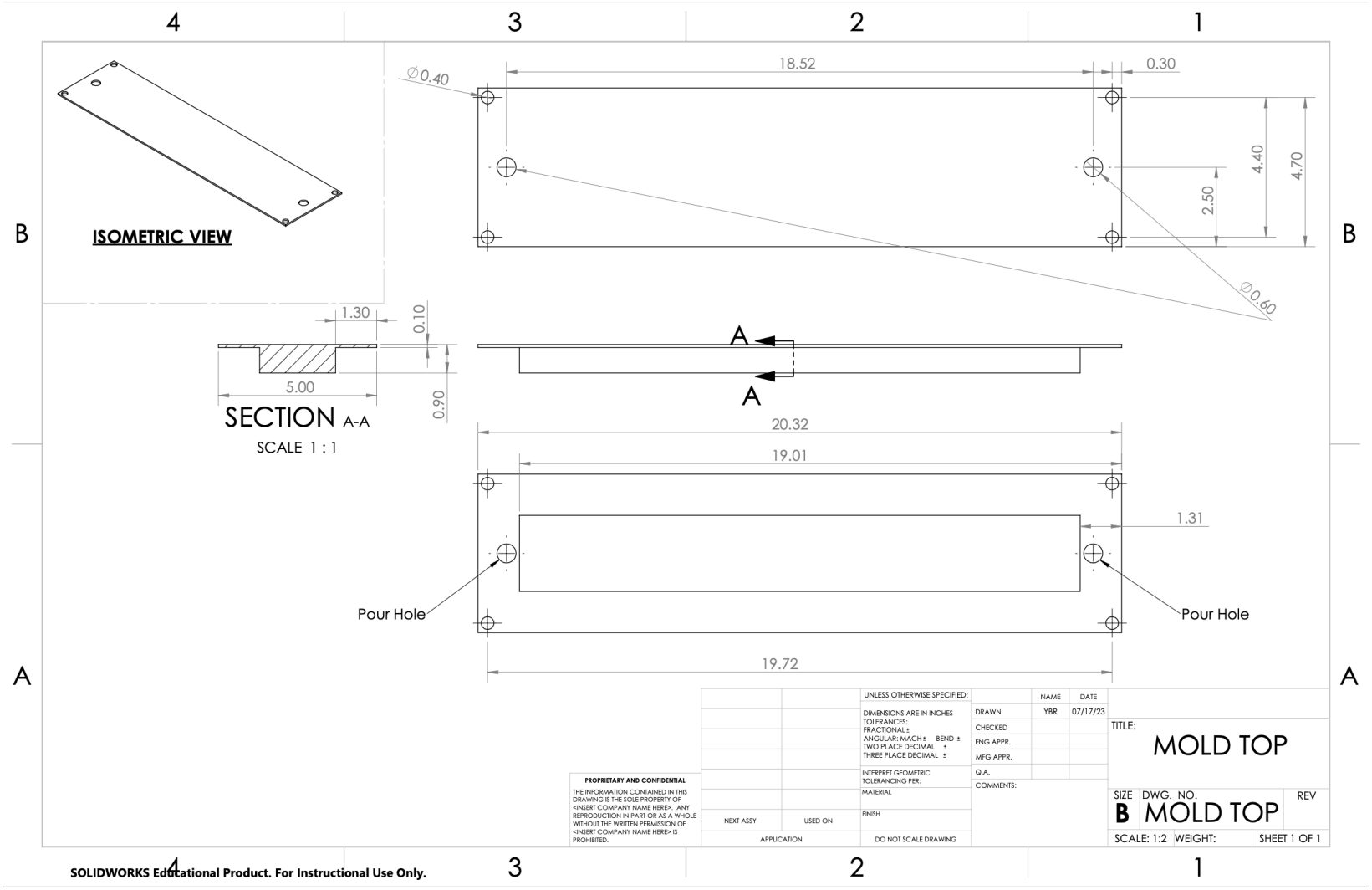

Figure 15: Silicon mold dye engineering drawing (top). Designed by Brandon Williams, modeled by Yogesh Rana.

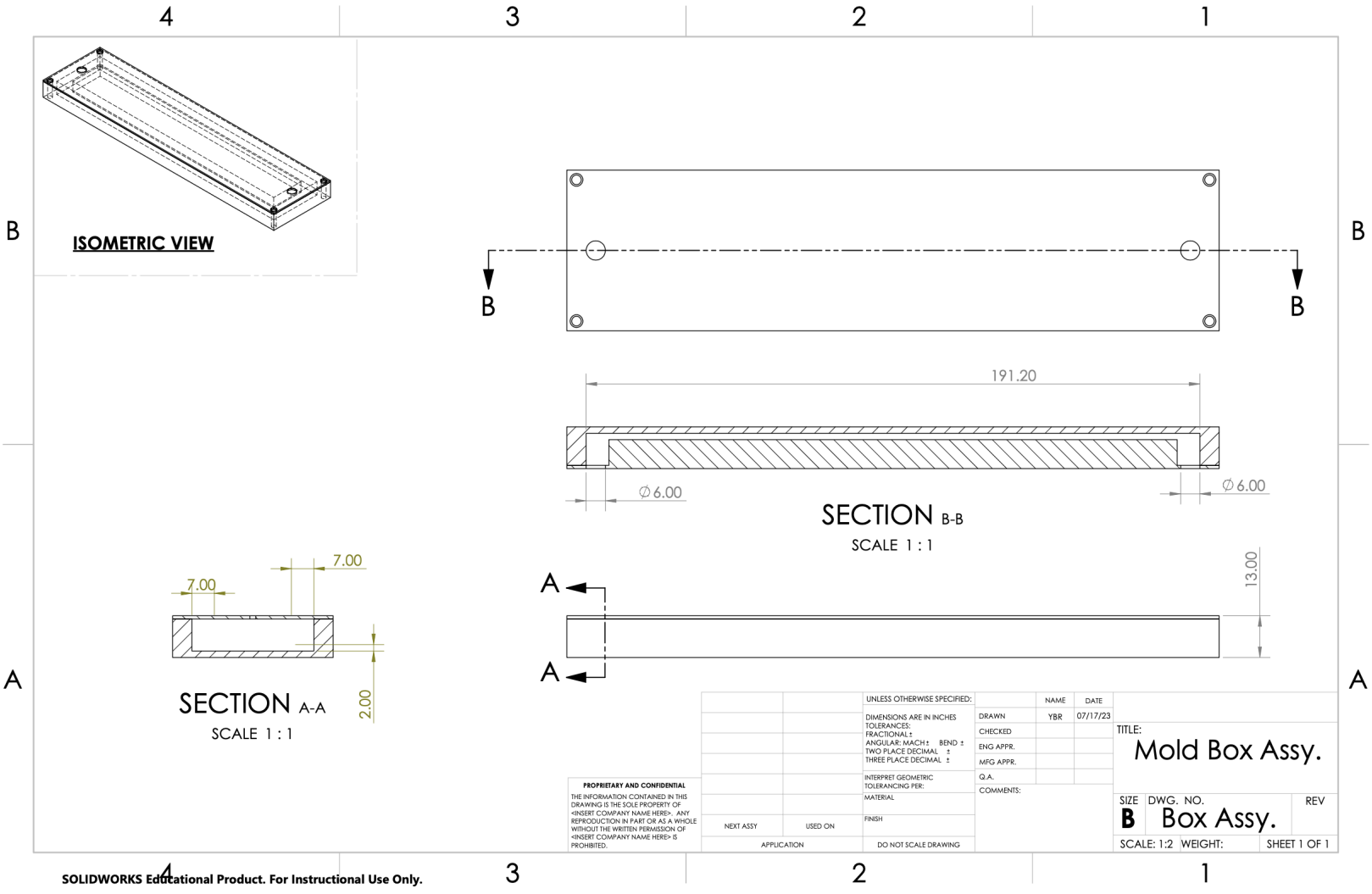

Figure 16: Silicon mold dye engineering drawing (assembly). Designed by Brandon Williams, modeled by Yogesh Rana.

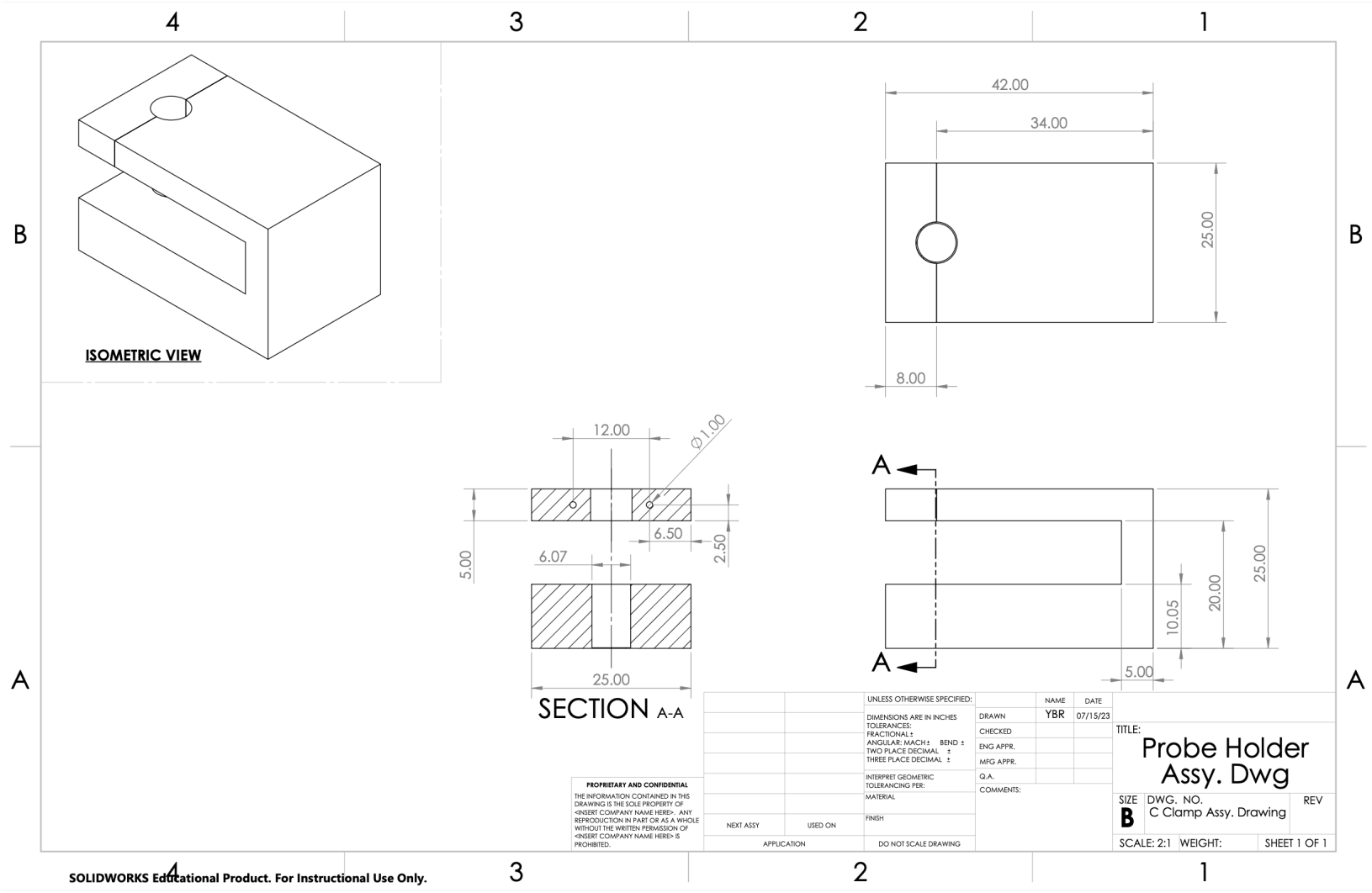

Figure 17: Indirect magnetization c-clamp engineering drawing (assembly). Designed by Brandon Williams, modeled by Yogesh Rana.

Bibliography

[1] J. Boshe. Acoustic emission examination of polymer-matrix composites. *Acoustic Emission Group*, pages 208–215, 2004.

[2] T.K. O 'Brien. Analysis of local delaminations and their influence on composite laminate behavior. *Delamination and Debonding of Materials*, pages 282–297, 1985.

[3] F. Chang. *Structural health monitoring 2013: A roadmap to intelligent structures*. Areesh Edu Trading, 2013.

[4] Vac Coat. Sputering process — sputtering deposition method. *https* : *//vaccoat.com/blog/sputtering/*, 2023.

[5] COMSOL. [32] comsol multiphysics reference manual. *www.comsol.com*.

[6] L. Dobrzanski. Properties of the magnetostrictive composite materials with the polyurethane matrix reinforced with terfenol-d particles. *Journal of Achievements in Materials and Manufacturing Engineering"*, 55(2):316–322, 2012.

[7] L A Makarova et al. Tunable layered composites based on magnetoactive elastomers and piezopolymer for sensors and energy harvesting devices. *Journal of Physics D: Applied Physics*, 54, 2021.

[8] V. Giurgiutiu. *Wave Propagation SHM with PWAS Transducers*. 2007.

[9] M. Haile, A. Hall, J. Yoo, M. Coatney, and O. Myers. Detection of damage precursors with embedded magnetostrictive particles. *Journal of Intelligent Material Systems and Structures*, 2015.

[10] A. Hamann and E. Dahlberg. High strain magnetostriction in a ferromagnet-polymer composite. *Applied Physics Letters*, 110(9):1–3, 2017. See `doi:10.1063/1.4977734`.

[11] Z. Hashin and S. Shtrikman. A variational approach to the theory of the effective magnetic permeability of multiphase materials. *Journal of Applied Physics*, 33(10), 1962. *https* : *//doi.org*/10.1063/1.1728579.

[12] D. Holder. Electrical impedance tomography: Methods, history and applications. *Carbon*, 2005.

[13] Corso Materiali intelligenti e Biomimetici. Magneto-rheological & magneto-strictive materials. *http* : *//www.centropiaggio.unipi.it/sites/default/files/course/material/magneto − reologicimagneto − strittivi.pdf*, 2018.

[14] A.K. Kaw. *Mechanics of Composite Materials, 2nd Edition*. Taylor & Francis Group, LLC, 2006.

[15] M. Kirschneck. Effects of magneto-mechanical coupling on structural modal parameters. *Topics in Modal Analysis II, Volume 8 Conference Proceedings of the Society for Experimental Mechanics Series*, pages 11–18, 2014.

[16] J. Krauthkramer and H. Krautkramer. *Ultrasonic Testing of Materials*. Springer-Verlag, 1990.

[17] E. Lacheisserie. *Magnetostriction: theory and applications of magnetoelasticity*. Boca Raton, Florida: CRC Press, 1993.

[18] Markets and Markets. Carbon fiber prepreg market by resin type (epoxy, phenolic, thermoplastic, bmi, polymide), manufacturing process (hot melt, solvent dip), end-use industry (aerospace & defense, automotive, sports & recreation, wind energy) - global forecast to 2027. $https://www.marketsandmarkets.com/Market-Reports/carbon-fiber-prepreg-market-25864916.html$, 2022.

[19] MarkForged. Mark two. $https://markforged.com/3d-printers/mark-two$, 2023.

[20] MaterialsScience2000. Magnetic particle inspection. https://www.youtube.com, 2014.

[21] J. Matrin, R.A. Anderson, D. Read, and G. Gulley. Magnetostriction of field-structured magnetoelastomers. *Physical Review E - Statistical, Nonlinear, and Soft Matter Physics*, 75(5), 2006. doi: 10.1103/PhysRevE.74.051507.

[22] S. Moore. Cfrp battery enclosures deliver multiple benefits in evs. https://www.plasticstoday.com/automotive-and-mobility/cfrp-battery-enclosures-deliver-multiple-benefits-evs, 2019.

[23] Mordor Intelligence. Automotive carbon fiber market size & share analysis - growth trends & forecasts (2023 - 2028). https://www.mordorintelligence.com/industry-reports/automotive-carbon-fiber-composites-market, 2022.

[24] B. Moskowitz. Hitchhiker's guide to magnetism. *Magnetic Anisotropy, Institute for Rock Magnetism*, 23(4):All, June 1991.

[25] O. Myeres and J. Alexander. Microstructure properties and strengthening mechanisms of the as4-3501-6 polymeric resin with embedded terfenol-d particles. *Development and Characterization of Multifunctional Materials; Modeling, Simulation and Control of Adaptive Systems; Structural Health Monitoring*, 1, 2014.

[26] NASA. Hypersonic composites resist extreme heat and stress. $https://spinoff.nasa.gov/Spinoff2007/ip_5.html$, 2007.

[27] A. Olabi. Design and application of magnetostrictive materials. 2005.

[28] W. Ong and W. Chiu. Non-cantact measurement techniques for structural health monitoring. *Procedia Engineering*, 75(doi: 10.1016/j.proeng.2013.11.009):45–50, 2014.

[29] Rebecca Shortland. Speed, strength, and safety: The importance of plastics in formula one. https://www.bpf.co.uk/article/plastics-in-formula-one-3292.aspx#: :text=Carbon2023.

[30] A.V. Ryzhkov, P.V. Melenev, C. Hom, and Y.L. Raikher. Coarse-grained molecular dynamics simulation of small ferrogel objects. *Journal of Magnetism and Magnetic Materials*, 383, 2015.

[31] D. Seifu. Torque magnetometer study of terfenol-d (tfd) in carbon fiber reinforce polymer. 2018.

[32] M. Shanmugham, H. Bailey, and W. Armstrong. Performance loss of terfenol-d particle epoxy composites under cyclic magneto-mechanical loading at the matrix glass transition start and finish temperatures. *Materials Science and Engineering*, pages 267–274, 2004. See . doi: 10.1016/j.msea.2003.11.038.

[33] Sika. Carbon fiber reinforced polymer (cfrp) plates. $https://www.sika.com$, 2023.

[34] Y.R. Sliozberg, J. Andzelm, C.B. Hatter, B. Anasori, and Y. Gogotsi. Interface binding and mechanical properties of mxene-epoxy nanocomposites. *Composites Science and Technology*, 192, 2020.

[35] Y.R. Sliozberg, J.L. Gair Jr., and A.J. Hsieh. Dissipative particle dynamics simulation of microphase separation in polyurethane urea nanocomposites. *Polymer*, 193, 2020.

[36] T.N. Tallman. Damage detection and conductivity evolution in carbon nanofiber epoxy via electrical impedance tomography. *Smart Materials and Structures*, 23(4), 2014.

[37] Electronics Tutorials. Hall effect sensor. $https://www.electronics-tutorials.ws/electromagnetism/hall-effect.html$, 2021.

[38] M.Y Wanhill, A.A Rashid, and N. Akram. Characterization of failure strain in fiber reinforced composites: Under on-axis and off-axis loading. *Crystals*, 11(https://doi.org/10.3390/cryst11020216), 2021.

[39] R.J.H Wanhill. Carbon fibre polymer matrix structural composites. *Research Gate*, ($DOI: 10.1007/978-981-10-2134-3_14$), 2017.

[40] Y. Zhu, C. Bakis, and J. Adair. Effects of carbon nanofiller functionalization and distribution on laminar fracture toughness of multi-scale reinforced polymer composites. *Carbon*, pages 1316–1331, 2012.

[41] S. Zurek, K. Chwastek, J. Jones, B. Koprivica, J. Leicht, and T. Taylor. Encyclopedia magnetica. $https://e-magnetica.pl/doku.php/start$.